First Principles and Genetic Algorithm Studies of Lanthanide Metal Oxides for Optimal Fuel Cell Electrolyte Design

Arif Ismail

Thesis submitted to the
Faculty of Graduate and Postdoctoral Studies
In partial fulfillment of the requirements
For the MSc degree in Chemistry

Department of Chemistry
Faculty of Science
University of Ottawa

Table of Contents

Abstract

As the demand for clean and renewable energy sources continues to grow, much attention has been given to solid oxide fuel cells (SOFCs) due to their efficiency and low operating temperature. However, the components of SOFCs must still be improved before commercialization can be reached. Of particular interest is the solid electrolyte, which conducts oxygen ions from the cathode to the anode. Samarium-doped ceria (SDC) is the electrolyte of choice in most SOFCs today, due mostly to its high ionic conductivity at low temperatures. However, the underlying principles that contribute to high ionic conductivity in doped ceria remain unknown, and so it is difficult to improve upon the design of SOFCs. This thesis focuses on identifying the atomistic interactions in SDC which contribute to its favourable performance in the fuel cell.

Unfortunately, information as basic as the structure of SDC has not yet been found due to the difficulty in experimentally characterizing and computationally modelling the system. For instance, to evaluate 10.3% SDC, which is close to the 11.1% concentration used in fuel cells, one must investigate 194 trillion configurations, due to the numerous ways of arranging the Sm ions and oxygen vacancies in the simulation cell. As an exhaustive search method is clearly unfeasible, we develop a genetic algorithm (GA) to search the vast potential energy surface for the low-energy configurations, which will be most prevalent in the real material.

With the GA, we investigate the structure of SDC for the first time at the DFT+U level of theory. Importantly, we find key differences in our results from prior calculations of this system which used less accurate methods, which demonstrate the importance of accurately modelling the system. Overall, our simulation results of the structure of SDC

agree with experimental measurements. We identify the structural significance of defects in the doped ceria lattice which contribute to oxygen ion conductivity. Thus, the structure of SDC found in this work provides a basis for developing better solid electrolytes, which is of significant scientific and technological interest.

Following the structure search, we perform an investigation of the electronic properties of SDC, to understand more about the material. Notably, we compare our calculated density of states plot to XPS measurements of pure and reduced SDC. This allows us to parameterize the Hubbard (U) term for Sm, which had not yet been done. Importantly, the DFT+U treatment of the Sm ions also allowed us to observe in our simulations the magnetization of SDC, which was found by experiment.

Finally, we also study the SDC surface, with an emphasis on its structural similarities to the bulk. Knowledge of the surface structure is important to be able to understand how fuel oxidation occurs in the fuel cell, as many reaction mechanisms occur on the surface of this porous material. The groundwork for such mechanistic studies is provided in this thesis.

Table of Figures

Table of Tables

List of Acronyms

DFT: ***D***ensity ***F***unctional ***T***heory

DFT+U: ***D***ensity ***F***unctional ***T***heory with Hubbard (***U***) correction

DOS: ***D***ensity ***O***f ***S***tates

GA: ***G***enetic ***A***lgorithm

GDC: ***G***adolinium-***D***oped ***C***eria

GGA: ***G***eneralized ***G***radient ***A***pproximation

IT-SOFC: ***I***ntermediate ***T***emperature ***S***olid ***O***xide ***F***uel ***C***ell

LDC: ***L***anthanide-***D***oped ***C***eria

LuDC: ***L***utetium-***D***oped ***C***eria

NN: ***N***earest ***N***eighbor

NNN: ***N***ext ***N***earest ***N***eighbor *(and so on for **NNNN**, **NNNNN**)*

PAW: ***P***rojector-***A***ugmented ***W***ave method

PBE: ***P***erdew, ***B***urke, ***E***rnzerhof density functional

PEMFC: ***P***olymer ***E***lectrolyte ***M***embrane ***F***uel ***C***ell

PES: ***P***otential ***E***nergy ***S***urface

SDC: ***S***amarium-***D***oped ***C***eria

SOFC: ***S***olid ***O***xide ***F***uel ***C***ell

XPS: ***X***-ray ***P***hotoelectron ***S***pectroscopy

YSZ: ***Y***ttrium-***S***tabilized ***Z***irconia

Simulation Packages

GULP: ***G***eneral ***U***tility ***L***attice ***P***rogram

SIESTA: ***S***panish ***I***nitiative for ***E***lectronic ***S***imulations with ***T***housands of ***A***toms

VASP: ***V***ienna ***A***b-Initio ***S***imulation ***P***ackage

Computer Clusters / Organizations:

CCRI: ***C***enter for ***C***atalysis ***R***esearch and ***I***nnovation

HPCVL: ***H***igh ***P***erformance ***C***omputing ***V***irtual ***L***aboratory

SHARCNET: ***S***hared ***H***ierarchical ***A***cademic ***R***esearch ***C***omputing ***Net***work

Acknowledgements

My time spent in the graduate program at the University of Ottawa was a memorable one, most of all because of the people I was surrounded by. The members of the Woo and Giorgi labs were very friendly and supportive throughout my time here, and always made coming in to work an enjoyable experience. Unfortunately, I can only highlight a few of the great times I had in the lab, to keep this section short. Specifically, I'd like to thank Peter Boyd, for breaking the sound barrier and finally reaching the big one hundred, on January 20th, 2011. I also thank Tom Daff, for his guidance with DFT calculations, and more importantly for making great pancakes. I also want to thank Michael Nohra, for his long-lasting friendship and for treating us to Denny's. It is difficult to summarize all of the good times I shared with Mike, Tom, and Pete; in essence, I just want to thank them for their friendship and ongoing support.

James Hooper, a former PhD student in the Woo group, helped me significantly at the start of my graduate studies. He wrote a large portion of the genetic algorithm code that I use in most of my thesis. As well, James was always available to answer my questions when I began this project. I learned a lot about Python programming and genetic algorithms from James, which proved useful throughout my Master’s degree.

My supervisors, Dr. Tom Woo and Dr. Javier Giorgi, were also very supportive and sources of great advice whenever I needed it. Being able to receive both of their input on this research project was critical to my success. As well, they showed great dedication to me as a student, always being available to answer questions, and provide useful feedback on presentations and manuscripts.

Lastly, I'd like to thank my family, who supported me the most. Even when I had difficult times at work, I could always feel comfortable at home, due to my mother's tireless efforts. My mom, brothers, and grandparents, all played an integral role in my daily life, and without them I could not have completed this work. By setting good examples, and helping me with anything and everything in life, they made it easy for me to succeed in my work.

CHAPTER 1 - INTRODUCTION

Section 1.1 - Fuel Cells

Fuel cells are widely regarded as a clean and efficient technology that will help alleviate the global energy crisis. In brief, they convert the chemical energy from a reaction into electrical output. Fuel cells have proven useful in industrial, residential, and transport applications in the past and present, and continue to be developed and improved upon to meet growing energy demands.

There exist many different kinds of fuel cells, each with its own advantages and disadvantages. They are commonly classified by the type of electrolyte. A brief discussion of the most common fuel cell types follows.

1.1.1 - Common Fuel Cell Types

By a conceptually simple design, the chemical energy from the reaction of hydrogen and oxygen is harnessed as electrical energy in a fuel cell. Half reactions occur at opposing electrodes which either require or generate electrons; as these electrons pass through a circuit, they are used to generate electrical power.

Two common types of fuel cells are polymer electrolyte membrane fuel cells (PEMFCs) and alkaline fuel cells. In the former, a solid porous electrolyte conducts hydrogen ions from the anode to the cathode, which react with oxygen to form water. In the latter, the electrolyte is an aqueous KOH solution that transports hydroxyl ions which react with hydrogen to form water. These fuel cells are implemented on large scales most likely because the product (water) is harmless to the environment. Yet, their components are not very cost effective.

An advantage of PEMFCs is their low operating temperature, which, at less than 100 °C, is in fact the lowest of all fuel cells. However, PEMFCs are exclusive to hydrogen fuel, for which a convenient storage method has not been implemented. Also, the production of the polymer membrane is costly and the cell is easily poisoned by carbon monoxide.[1] Yet, due to the fact that they emit no pollutants, they remain very attractive energy sources.

Alkaline fuel cells have proven useful in the past, providing on-board electricity, heat, and water to NASA astronauts on the Apollo space missions. However, there are several cost issues that limit its mass production. For instance, the fuel cell cannot contain any carbon dioxide, as this converts KOH into the carbonate form, which diminishes conductivity in the electrolyte and ruins cell performance. Therefore, pure oxygen must be fed into the cathode, or if the air contains carbon dioxide, some sort of cleansing mechanism must be put in place; while feasible for an agency like NASA, this is clearly not a practical option for others.

Currently, alkaline and PEMFC technologies are used to power buildings, automobiles, and buses, although they are not widespread. The leading company in this business, the United Technologies Corporation, makes fuel cell products which operate on pure hydrogen fuel. In a lot of cases, large quantities of hydrogen are required which cannot be met by storing pure hydrogen on site. Thus, the fuel plant contains a reforming centre where methane from natural gas is converted to hydrogen. This reforming process requires a lot of space and energy, and so is not ideal for transport applications. What is desired in these applications is a fuel cell which can operate on an abundant and inexpensive resource, like natural gas, at a low temperature with low emissions. Also, the

materials should be relatively cheap to make and durable over a long time period. In the next section, a fuel cell type which fits this description is described in detail.

1.1.2 - Solid Oxide Fuel Cells

In solid oxide fuel cells (SOFCs), a solid oxide is used as the electrolyte to transport oxygen ions from the cathode to the anode. These types of fuel cells require the highest operating temperature of all fuel cells, but also have marketable advantages over the other types. For instance, it is possible to use fuels other than hydrogen in an SOFC, such as methane, and achieve greater power density. Since their discovery, the high operating temperature of approximately 1000 °C has always been the biggest setback of the solid oxide fuel cell. Recently, scientists have succeeded in lowering the operating temperature to much more feasible values, such as 400 to 600 °C; these are known as intermediate temperature solid oxide fuel cells (IT-SOFCs) and they are of prime interest to commercialize.

In terms of the fuel gas, there are a wide range of chemicals that can be used in an SOFC. In theory, any chemical that can be oxidized over the anode is a viable fuel. The conventional hydrogen fuel cell uses solely pure hydrogen gas as the input, creating water as the only product. From an emissions point of view, this type of fuel is ideal because its output raises no threat to the environment. However, from a practical standpoint, a safe and economical way of storing the hydrogen in a working fuel cell has yet to be discovered. Hence, there exists a need for another type of environmentally-friendly fuel.

Hydrocarbons, and in particular natural gas, represent viable fuels for SOFCs due to their low cost and high abundance. With the right choice of catalyst, the anode first partially oxidizes methane, which is the main component of natural gas, to carbon

monoxide and hydrogen, a mixture known as syn gas. Subsequently, the hydrogen and carbon monoxide are further oxidized to produce water and carbon dioxide.[2] Essentially, methane provides a means of using hydrogen in a fuel cell without needing to store pure hydrogen, which is a significant advantage SOFCs have over other fuel cell types.

A disadvantage of using hydrocarbons is carbon formation on the anode surface, which causes the cell to stop working. This phenomenon, known as "coking", is a well known problem amongst fuel cell chemists. Identifying materials that are resistant to coke formation remains a subject of intense research. Another issue with hydrocarbon fuels is the emission of CO_2. Although not ideal for the environment, methane-fuelled SOFCs emit much less carbon dioxide than fossil fuel combustion engines, and so SOFCs are still an improvement over existing technologies.

The components of a solid oxide fuel cell are as follows. Oxygen, or air containing oxygen, is fed into the cathode where it is reduced to its anionic form. The oxygen anions pass from the porous cathode through the solid electrolyte to the anode of the fuel cell, where they oxidize the fuel (such as methane or hydrogen gas). The electronic circuit is attached to either end of the cell, which allows one to harness the chemical energy from the reactions as electrical output. A schematic is shown in Figure 1–1.

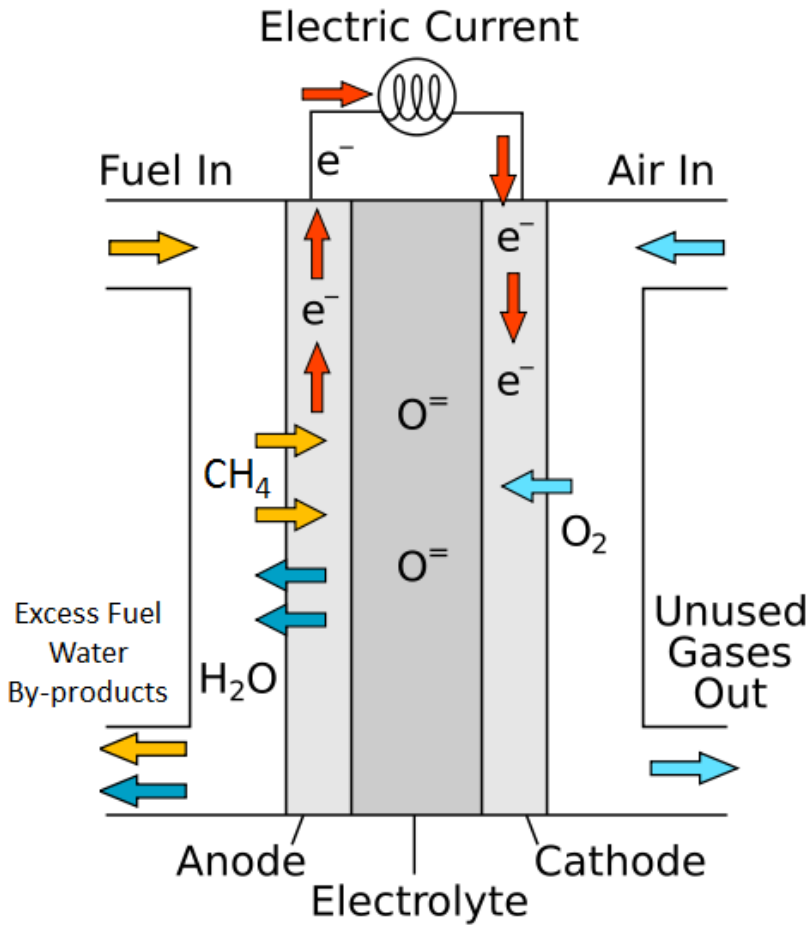

Figure 1–1. A solid oxide fuel cell.[3]

Section 1.2 - Doped Ceria

1.2.1 - Fuel Cell Electrolytes

The solid electrolyte must isolate the two gas atmospheres at the anode and cathode from one another, while transporting oxygen ions quickly across the cell. Thus, the ideal electrolyte has high oxygen ion conductivity, negligible electronic conductivity, and is chemically stable under both the highly oxidizing environment of the cathode and the highly reducing environment of the anode. For several years, yttrium-stabilized

zirconia (YSZ) has been the most studied and used electrolyte material in SOFCs, due to its high ionic conductivity and stability.[4] In particular, the structure of YSZ is known to be crucial to its function in the fuel cell. Zirconium oxide, ZrO_2, is doped with yttrium sesquioxide (Y_2O_3) in a concentration of about 8 mol % Y_2O_3 to make YSZ. As the trivalent Y species replaces the tetravalent Zr in the lattice, a charge imbalance is induced. To neutralize the overall charge, oxygen ions spontaneously exit the lattice, thereby creating vacant spots in the anion sub-lattice. It is believed that the increased mobility of oxygen anions in the YSZ lattice is due to the migration over these oxygen vacancies. Furthermore, the Y dopant stabilizes the cubic structure of zirconia from room temperature to the operating temperature range of the fuel cell.[4]

The major drawback of YSZ is that it is only significantly conductive at temperatures above 800 Celsius. Therefore it is not a suitable electrolyte for fuel cells operating at lower temperatures. For IT-SOFCs, a material that rapidly conducts oxygen anions at such temperatures is desired. Ceria-based materials are promising candidates for this application due to their high conductivity at 500 Celsius. Cerium oxide, or ceria (CeO_2), doped with a trivalent ion creates intrinsic oxygen vacancies, much like yttrium doping does to zirconia. While several trivalent dopants have been found to improve conductivity in ceria, the highest ionic conductivity is achieved with Sm^{3+} as the dopant.[5, 6] Recently, ceria containing two different trivalent species have been synthesized, which can increase oxygen ion conductivity beyond that of singly doped ceria compounds.[7] However, co-doped cerias are relatively new materials and are not nearly so ubiquitous in fuel cell laboratories. A lot of work remains to be done to find optimal combinations of dopants, and produce an electrolyte better than samarium-doped ceria (SDC) that can be

used in a fuel cell. Currently, samarium-doped ceria is one of the most commonly used electrolytes. This is due not only to its high ionic conductivity, but also because of its low electronic conductivity, which prevents electrons from leaking through the electrolyte and out of the power circuit. SDC is also known to have good stability in the reducing environment of the cell, which is an important feature for long-term use.

1.2.2 - Motivation

In order to commercialize solid oxide fuel cells, further optimization is required. For instance, a mechanistic understanding of fuel oxidation over commonly-used anodes will enable the prediction and development of better materials, which are resistant to problems such as coking. To find the mechanism, one must first know the structure of the anode and electrolyte surfaces on which the reaction occurs. Knowledge of the structure provides insight on the material's properties and at the same time enables more complex investigations such as fuel oxidation mechanisms. For this purpose, we study primarily samarium-doped ceria, one of the most commonly employed electrolytes. The fundamental factors that make SDC a superior ionic conductor to other doped ceria materials are currently unknown. This knowledge will be useful to improve solid oxide fuel cells, as it will lead to the design of better solid electrolytes. To identify these atomistic interactions which influence conductivity, the structure of the electrolyte material must be found.

Unfortunately, the literature on the structure of doped ceria is scarce, which is due in part to the difficulties in experimentally characterizing and computationally modelling this system. It is possible to obtain some structural information from x-ray absorption spectroscopy, however only ions up to a 3 Angstrom radius around a target ion can be

identified with sufficient accuracy.[8] In order to find the structure of doped ceria, one must evaluate all possible configurations of dopants and vacancies in the lattice in order to find the lowest-energy structures, which lie within kT (and hence are populated) at fuel cell temperatures. However, the number of configurations is enormous at the dopant concentrations which are used in fuel cells, and so a systematic evaluation of all these is not feasible (see Figure 1–2). In experiment, an 11.1 % dopant concentration of samarium oxide (or 20 mol % Sm) is used. To model a similar system, in a 2x2x2 simulation cell of ceria consisting 96 atoms, there are 163 trillion ways to place six dopants and three vacancies in the cell, which corresponds to 10.3 % of the dopant oxide, or 18.75 mol % of the dopant atom. Although some of these possibilities are equivalent by symmetry, the number of unique configurations is still too high to evaluate systematically. Current modelling studies of doped ceria use a lower concentration, where the possible structures are fewer in number. In fact, for the most part, the literature is limited to 3.2 % concentrations, where there are two dopants and one vacancy in the cell. Due to symmetry, only 33 unique configurations are present at this concentration and so they can be evaluated with reasonable computational accuracy.

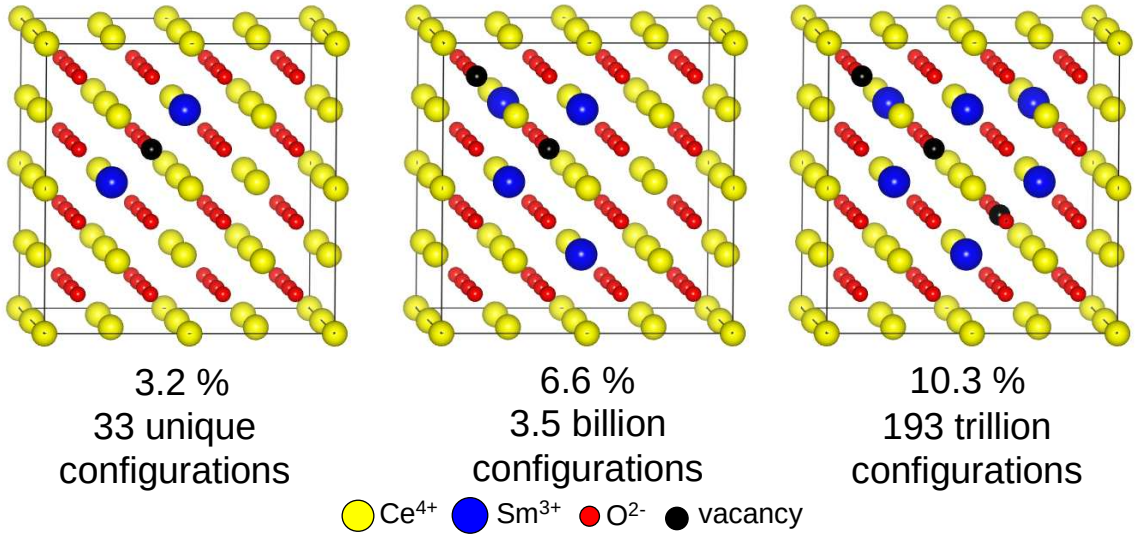

Figure 1–2. 2x2x2 simulation cells of doped ceria at various dopant concentrations, with the number of unique configurations (*left*) and the number of possible configurations (*middle and right*).

There also exist modelling studies which attempt to understand the oxygen ion migration pathway in doped ceria. Of particular interest is identifying the physical nature of SDC's high ionic conductivity. One can begin from the Arrhenius relationship, which relates ionic conductivity (σ) to the activation energy (E_a) for oxygen ion diffusion (1):

$$\sigma = \frac{\sigma_0}{T} \cdot \exp\left(\frac{-E_a}{k_B T}\right) \tag{1}$$

where σ_0 is a temperature-independent pre-exponential factor depending on ionic oscillation frequency and entropy of ion migration,[9] T is the temperature, and k_B is the Boltzmann constant. For pure ceria, the activation energy is often parsed into two components: the migration energy (E_m) and the vacancy formation energy (E_f). However in doped ceria, the dopants and vacancies form associates[10] with corresponding association energies (E_{ass}) which influence vacancy mobility. The energies of these associates determine the number of mobile vacancies in doped ceria much like the vacancy formation energy determines the concentration of vacancies in pure ceria; hence,

in doped ceria, the activation energy is understood as the sum of the migration energy and the association energy components. Yet, at high temperatures, most vacancies are dissociated and so E_{ass} can essentially be neglected. However, at low and intermediate temperatures (below 500 °C), the relative association energies of different configurations play a key role in diffusion pathways.[5, 11] Such temperatures are of the most interest because it is this low-to-intermediate range that is currently being targeted for future SOFCs to operate within.[12-14] It is thus desirable to know what structure factors minimize the dopant-vacancy association energy, which will in turn increase vacancy mobility and the performance of these materials as solid electrolytes.

In order to find these structural properties, one should investigate all possible configurations of SDC. Then the oxygen ion migration pathway can be determined by calculating the activation energy for various migrations amongst the low-energy configurations. However, at a high level of accuracy, such as that of periodic DFT calculations, the combinatorial problem is encountered again. There are simply too many possible migrations to make in the lattice when the dopant concentration is increased to experimentally-relevant values. Thus, there is a need for an efficient search method to find the low-energy configurations of SDC at an 11% dopant concentration, in order to model the real system. The structure will also provide an atomic-level understanding of the properties that yield high ionic conductivity in doped ceria, which will serve to build better electrolytes for future SOFCs.

1.2.3 - Current Computational Studies of the Doped Ceria Structure

To date, the only studies which have been done to model oxygen migration with electronic structure calculations such as DFT used the 3.2 % dopant concentration.[5, 6, 11,

[15] This limits the scope of their results because, at higher concentrations, the increased amount of dopants and vacancies are expected to play a pivotal role in the ionic conduction mechanism. There is one work which attempted to simulate oxygen ion conduction in SDC with molecular dynamics at the optimal 11% doping level.[16] However, these authors used classical potentials which were not fit to experiment, and placed the dopant ions in random lattice positions, which may not be accurate; overall, they did not gain any insight into the fundamental nature for increased conductivity in SDC.

Earlier works that attempted to model doped ceria suffered from inconsistencies in their calculations which resulted in a poor agreement with experiment. For example, Yoshida *et al.* neglected cationic sub-lattice relaxation in their calculation of migration barriers for Y-, La-, and Sm-doped ceria, and found a different order of activation energies than experiment.[17] The very first theoretical works used empirical potentials which made predictions on ionic conductivity based on dopant radii; however, not all configurations were investigated, and so an important low-energy structure may have been overlooked. Also, classical potentials are typically fit to the experimental lattice constant, which is an elastic parameter; the electronic component of dopant-vacancy association is not considered when developing classical potentials. Thus, it is imperative to use electronic structure calculations that capture accurately the differences in association energy between various configurations, such as density functional theory (DFT).

The first theoretical works that investigated the structure of doped ceria at a high level of theory were by Andersson *et al.*[5] and Muthukkumaran *et al.*,[6] which calculated

the activation energy for oxygen ion migration in lanthanide-doped ceria at 2.1 and 3.2% dopant concentrations. Using DFT calculations, the authors concluded that for Pm^{3+} and dopants to the right of Pm^{3+} in the lanthanide series, oxygen vacancies prefer to lie nearest neighbour (NN) to the dopant - meaning a dopant ion lies in the first coordination shell surrounding the oxygen vacancy. For larger dopants, to the left of Pm^{3+}, the vacancies prefer to lie in the second coordination shell, or next-nearest neighbour (NNN) to the dopant. (To aid in the visualization of dopant-vacancy distances, consider Figure 1–2. In the left picture, both dopant ions lie NN to the vacancy. In the middle picture, the additional two dopants added to make 6.6%, lie NNN to the same vacancy.) The authors also found that Sm-doped ceria had the lowest activation energy for vacancy migration compared to all other dopants, which is consistent with experimental data. However, not all possible configurations were sampled and so an important pathway may have been overlooked. A systematic search for 3.2% doped ceria is possible, as there are only 33 unique configurations to evaluate. In 2009, Wei *et al.* performed such a search for 3.2% lanthanide-doped ceria, with classical potentials.[11] The main conclusion from this work, which was later confirmed by DFT calculations,[15] was that the crossover from NNN to NN preference occurs at Gd^{3+}, and for Gd^{3+} itself there is no preference. Several, near-degenerate, low-energy structures were found for Gd-doped ceria which suggest that the vacancies do not prefer a specific configuration. This finding could suggest a reason for the high ionic conductivity of Gd-doped ceria, which is almost as high as that of SDC.[18]

So far, it has been assumed that first principles DFT calculations provide accurate descriptions of the electronic structure in doped ceria. This is not entirely true. In current DFT functionals, the well known self interaction error exists for strongly correlated d and

f electrons.[19] As a result, in rare-earth metals the f electrons are over delocalized, which makes what should be insulators behave as metals. A Hubbard correction to the DFT method known as DFT+U has recently emerged as a tool for correctly describing strongly correlated electrons. An empirical potential (known as the U parameter) is added to the rare-earth metals such that the f electrons are localized and the self-interaction error is corrected. Several studies of ceria have found that the DFT+U method correctly predicts experimental properties that conventional DFT does not, such as density of states, lattice constant, bulk modulus, and metallic character.[20-24] In this respect, the most accurate electronic structure method available to model doped ceria is DFT+U.

Recent works by Dholobhai *et al.*[25, 26] have demonstrated that DFT+U calculations yield different results than plain DFT for Gd- and Pr-doped ceria. Dholobhai calculated the migration barriers for all possible migrations of an oxygen ion in 3.2 % doped ceria, and found that in gadolinium-doped ceria the dopant ion prefers to lie nearest neighbor to the vacancy, a finding which contradicts the classical and DFT studies by Wei[11] and Nakayama.[15]

Section 1.3 - Thesis Goals and Outline

This thesis attempts to discover the fundamental properties of samarium-doped ceria that make it a good ionic conductor and solid oxide fuel cell electrolyte. The first step is to identify the atomistic interactions in doped ceria which minimize dopant-vacancy association energy, and hence increase conductivity. For this purpose, we will investigate the structure of SDC and other lanthanide-doped ceria materials at various dopant concentrations. In order to simulate concentrations higher than 3.2%, where there

are too many possible configurations to evaluate systematically, an intelligent search method will be designed. The search technique will be created to sample the entire structure space of lanthanide-doped ceria and find the configurations that will be prevalent at IT-SOFC operating temperatures.

As SDC at the 11.1% dopant concentration has not been accurately modelled before, we hope that the structural information provided in this thesis serves as a basis for future modelling studies of SDC. In addition, it adds to the understanding of atomistic interactions in doped ceria which optimize conductivity, which is needed to build better fuel cells.

In addition to the structural properties of SDC, this thesis will focus on providing new information on SDC's electronic properties. To this end, we will present new experimental data and use it to build an accurate DFT+U model for SDC. The computational investigation of SDC's electronic properties will provide further insight on the electronic structure data obtained by experiment.

Lastly, because the surfaces of fuel cell electrolytes play a critical role in fuel oxidation, it is important to study the SDC surface. The goals of this section will be to identify the structure of low-index surfaces of SDC as well as the differences between bulk and surface composition. These results will form the basis for studies of oxygen ion diffusion and fuel oxidation mechanisms over the SDC surface. Hence, this thesis will be useful to fuel cell and materials scientists who hope to optimize solid oxide fuel cells.

The rest of the thesis is organized as follows. Chapter 2 contains the computational details, including a description of our intelligent search method used to find low-energy structures. The structure search results for LDC are found in Chapter 3,

where we emphasize the importance of using accurate calculations. In Chapter 4, we show the electronic properties of SDC, found by both calculation and experiment. Next, to build on our bulk structure search, we perform a surface structure search in Chapter 5. Finally, the conclusions and future work are outlined in Chapter 6.

Section 1.4 - References

1 S. Srinivasan, *Fuel Cells : From Fundamentals to Applications*, Springer US, 2006.

2 S. C. Singhal and K. Kendall, *High Temperature Solid Oxide Fuel Cells*, Elsevier, 2003.

3 U. author, Solid oxide fuel cell, ed. Solid_oxide_fuel_cell.svg, 2007, p. Figure.

4 P. Holtappels, U. Vogt and T. Graule, *Advanced Engineering Materials*, 2005, **7**, 292-302.

5 D. A. Andersson, S. I. Simak, N. V. Skorodumova, I. A. Abrikosov and B. Johansson, *Proc. Natl. Acad. Sci. U.S.A.*, 2006, **103**, 3518-3521.

6 K. Muthukkumaran, R. Bokalawela, T. Mathews and S. Selladurai, *J. Mater. Sci.*, 2007, **42**, 7461.

7 F. Y. Wang, B. Z. Wan and S. F. Cheng, *J. Solid State Electrochem.*, 2005, **9**, 168-173.

8 H. Yoshida, H. Deguchi, K. Miura, M. Horiuchi and T. Inagaki, *Solid State Ionics*, 2001, **140**, 191-199.

9 W. Wieczorek, *Mater. Sci. Eng., B*, 1992, **15**, 108-114.

10 M. Mogensen, N. M. Sammes and G. A. Tompsett, *Solid State Ionics*, 2000, **129**, 63-94.

11 X. Wei, W. Pan, L. Cheng and B. Li, *Solid State Ionics*, 2009, **180**, 13.

12 D. H. Dong, D. Li, X. Y. Zhang, Z. L. Chai, K. Wang, C. Z. Li, D. Y. Zhao and H. T. Wang, *J. Mater. Chem.*, 2010, **20**, 1122-1126.

13 B. Lin, J. Chen, Y. Ling, X. Zhang, Y. Jiang, L. Zhao, X. Liu and G. Meng, *J. Power Sources*, 2010, **195**, 1624-1629.

14 X. G. Zhang, M. Robertson, S. Yick, C. Deces-Petit, E. Styles, W. Qu, Y. S. Xie, R. Hui, J. Roller, O. Kesler, R. Maric and D. Ghosh, *J. Power Sources*, 2006, **160**, 1211-1216.

15 M. Nakayama and M. Martin, *PCCP*, 2009, **11**, 3241.

16 S. F. Lee and C. W. Hong, *CMC-Comput. Mat. Contin.*, 2009, **12**, 223-235.

17 H. Yoshida, T. Inagaki, K. Miura, M. Inaba and Z. Ogumi, *Solid State Ionics*, 2003, **160**, 109-116.

18 K. Eguchi, T. Setoguchi, T. Inoue and H. Arai, *Solid State Ionics*, 1992, **52**, 165-172.

19 N. J. Mosey and E. A. Carter, *Phys. Rev. B*, 2007, **76**, 155123.

20 D. A. Andersson, S. I. Simak, B. Johansson, I. A. Abrikosov and N. V. Skorodumova, *Phys. Rev. B*, 2007, **75**, 035109.

21 J. L. F. Da Silva, M. V. Ganduglia-Pirovano, J. Sauer, V. Bayer and G. Kresse, *Phys. Rev. B*, 2007, **75**, 045121.
22 M. Nolan, V. S. Verdugo and H. Metiu, *Surf. Sci.*, 2008, **602**, 2734.
23 Z. Yang, Luo, G., Lu, Z., Woo, T. K., Hermansson, K., *J. Phys.: Condens. Matter*, 2008, **20**, 035210.
24 Z. Yang, G. Luo, Z. Lu and K. Hermansson, *J. Chem. Phys.*, 2007, **127**, 074704.
25 P. P. Dholabhai, J. B. Adams, P. Crozier and R. Sharma, *J. Chem. Phys.*, 2010, **132**, 094104.
26 P. P. Dholabhai, J. B. Adams, P. Crozier and R. Sharma, *PCCP*, 2010, **12**, 7904.

CHAPTER 2 - METHODS

Section 2.1 - Search method

An efficient and practical search method is needed to find the structure of doped ceria at experimentally-relevant dopant concentrations, simply because there exist too many possible configurations to evaluate systematically. The goal is to find the low-energy configurations of a doped metal oxide, like samarium-doped ceria, and the differences in energy between them. An evolutionary-inspired search method known as the genetic algorithm (GA) has proven effective in crystal structure prediction previously.[1] For example, Oganov *et al.*[2] and Hooper *et al.*[3] used genetic algorithms to find structures of polymeric nitrogen at various pressures. For this application, we modified the genetic algorithm of Hooper *et al.*[3] to find low-energy structures of doped metal oxides. A detailed description of my personal contributions to the code are provided at the end of this section.

There are multiple options when creating a genetic algorithm, which are described by Woodley and Catlow.[1] In this section, we discuss only our implementation of the GA search method. The entire process is automated by a Python code and can be run on the CCRI (or "Wooki"), HPCVL, and SHARCnet computer clusters.

As the algorithm is inspired by evolutionary principles, many of the terms used to describe the GA and its elements stem from evolutionary biology. In a structure search, there are several different configurations, which differ in their positions of dopants and oxygen vacancies. To distinguish one configuration from the next, the GA code keeps track of each structure's coordinates. The identity of each structure is encoded in its

genetic information, or its "genes". Thus, a *gene* is defined as the list of fractional x, y, and z coordinates of the atoms which make up a particular structure. In addition, the coordinates of the oxygen vacancies are included in the gene list. A separate list called *atomtypes* keeps track of the different atomic species in each structure, and is written in the same order as the gene list. For instance, the first four x, y, and z positions correspond to the first four atomic species in the atomtypes list. This is important to keep track of, because the positions of the dopant atoms and vacancies are crucial to the uniqueness of each gene. In the atomtypes list, the vacancies are represented by dummy atoms, which do not correspond to real elements. All of the genes, or structures, make up what is known as the *population*. The program begins by randomly creating unique structures to fill up a population of pre-determined size. These structures are created based on criteria input by the user. For instance, the structure of doped ceria is known to be a face-centered cubic lattice of cerium cations with an interpenetrating simple cubic lattice of oxygen anions. The user specifies a specific concentration of dopant which tells the program to substitute the corresponding number of dopant ions for cerium ions from the pure ceria lattice, and remove the corresponding number of oxygen ions to form vacancies. During initial structure creation, the program tests each newly created structure against all existing members of the population, to make sure that each new gene is unique. For this test, a code was created to check the distances of dopant atoms to dopant atoms, dopant atoms to vacancies, and vacancies to vacancies in each structure. These three distances provide an unambiguous determination of uniqueness between any two doped ceria configurations.

Once the population is made, each gene is assigned a *fitness*, which will determine its fate in the next generation of structures. In the GA, the fitness is the property of the algorithm that the user wishes to optimize. Our algorithm applies Darwinian selection for choosing new structures. Hence, the more fit a structure is, then the more likely it is to pass on its genetic information to future populations. (The method in which its structural information is "passed on" is discussed later.) In this case, the algorithm is designed to look for low-energy configurations, so it makes sense then that the fitness of a structure is defined as the total energy following geometry optimization. To see how this energy is calculated, refer to Section 2.2. Originally, the total energy from a single point energy evaluation - that is, without optimizing the geometry - was used as the fitness. However, it was quickly noted that the ranking of structures by single point energies and by energies after optimization is not the same; in fact, significantly different configurations were found to be favored with the two definitions of fitness. It is of course more reliable to use the energy of a structure in a local minimum as the fitness, so all GA results presented in this thesis are using the energy of the optimized geometry as the fitness. The programs used to optimize the geometry are discussed in Section 2.2. In terms of the code, the genes are ranked by energy, and weighted by a Boltzmann distribution to determine their probability of selection for reproduction. This weighting is designed to represent the evolutionary principle of natural selection or "survival of the fittest".

Wherever possible, it is the goal of the genetic algorithm to create more fit populations. In our case, it corresponds to the new population being created from the favorable structural qualities of the previous population. For this purpose, the genes from

the current population which are selected for reproduction undergo one of the many mating and mutation operations that have been designed for metal oxides. In general, the goal of these operations is to produce more fit genes efficiently, however they also serve to maintain genetic variability in the population. Genetic variability, which corresponds to differences among structures in the population, is important for any algorithm to proceed effectively. By introducing this variability, more of the configurational space is explored, and so the more likely and quickly it is that the algorithm finds the global minimum of the potential energy surface. The mating and mutation operations, as well as the other schemes used to create the new population, are explained below. James Hooper, a former Ph.D. student of Dr. Tom Woo, wrote the code for these operations.[4]

The mating operation corresponds to taking elements of two parent genes to create two new, "child" genes. The new genes are spliced forms of the parents, taking segments from one parent and complementary segments from the other parent's gene. In the context of the new structure, it corresponds to taking the metal atoms from one parent and the oxygen atoms and vacancies from the other parent. The second child will have the complementary segments that the first child did not receive. A schematic is shown in Figure 2–1.

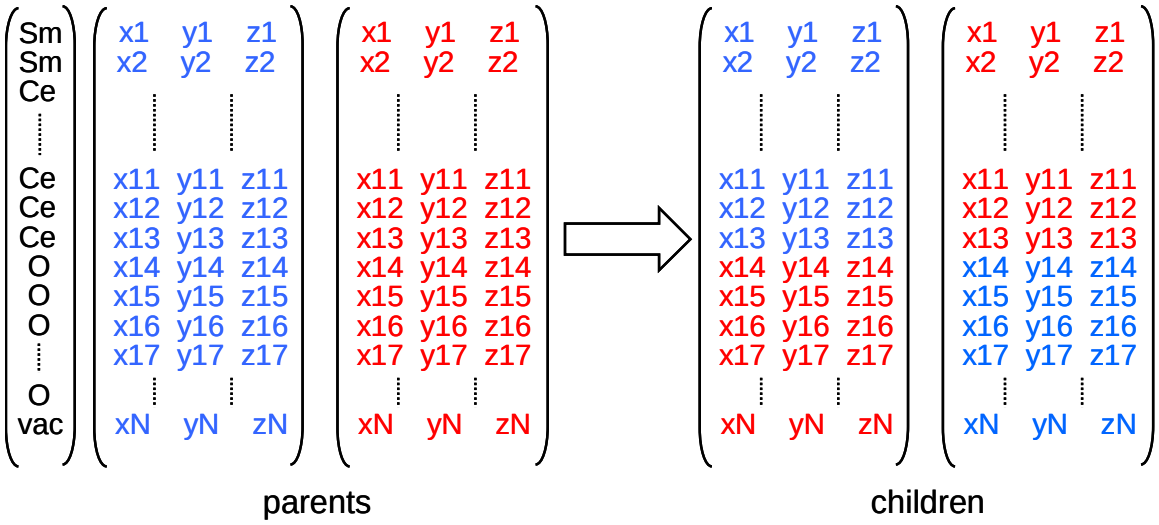

Figure 2–1. Genetic algorithm mating routine. The left-most column is the atomtypes list (where "vac" signifies a vacancy) followed by the genes of both parents and the children. The splicing occurs so that the new genes receive cations from one parent and anions from the other parent.

Mutation operations alter a structural quality of a single gene to make a new member of the next generation. The operations include: a) modifying a subset of the dopant atoms; b) modifying a subset of the vacancies; c) performing a) and b) together; and d) a geometry perturbation. In the first operation, a random subset of the dopant atoms is selected (which ranges from 1 to the total number of dopant atoms in the cell) to be replaced with cerium ions at random positions in the lattice. The second operation works in a similar fashion, instead using the vacancies and the oxygen ions in the lattice. The third operation is just the sum of the first two, so it changes both the positions of dopants and vacancies. The geometry perturbation alters the coordinates of one or more of the atoms in the parent structure. The maximum amount by which the atoms can be moved is specified by the user, to avoid creating nonsensical geometries. This last operation is designed to explore more of the potential energy surface which is not available through any other operation performed on the positions in the ideal lattice geometry.

To generate the new population, in addition to the new structures created from mating and mutations, a small number of structures are promoted unchanged from the current population to the next generation. This method is known as *elitism* and is key to any genetic algorithm. It ensures that the best genes from one population are at least as fit as the best genes from the next population, in case the mating and mutation routines do not discover a better gene. The number of elite structures must be kept small enough so as to not decrease genetic variability to an unhealthy low value. At the same time, the number of elite structures must be large enough to preserve the good members of the population in the genepool. It is set to be between 10 and 15 % of the population by default, however for large populations the user typically lowers this value in the input file. For example, for a population of 500 structures, it was found that promoting the best 20 at each generation is a healthy number for the GA. This number leads to the most efficient retrieval of the best structures and therefore represents the balance described above.

Finally, at each generation, the program generates new random structures to add to the new population. The random genes make up five percent of the new population. This is another way that the algorithm ensures genetic variability. Another advantage of putting random genes into the population is that it allows for the possibility of exploring new parts of the potential energy surface, if one of these structures is selected for reproduction. This is especially crucial at late stages in the GA, when the elite members of the population stop changing at every generation. At this point, the genes selected for reproduction very often share several of the same structural qualities, so the mating

operation is redundant. If one of the randomly generated structures is selected, then it introduces new structural qualities in the children, which would otherwise be unexplored.

Every new population that is created represents one generation or one cycle of the GA. This process is repeated until the elite genes remain the same for a sufficient number of generations. Once the best structures stop changing, then the GA is converged. The user must determine through tests of various population sizes, what is a sufficient number of generations to assure convergence. A flowchart summarizing the algorithm is shown in Figure 2–2.

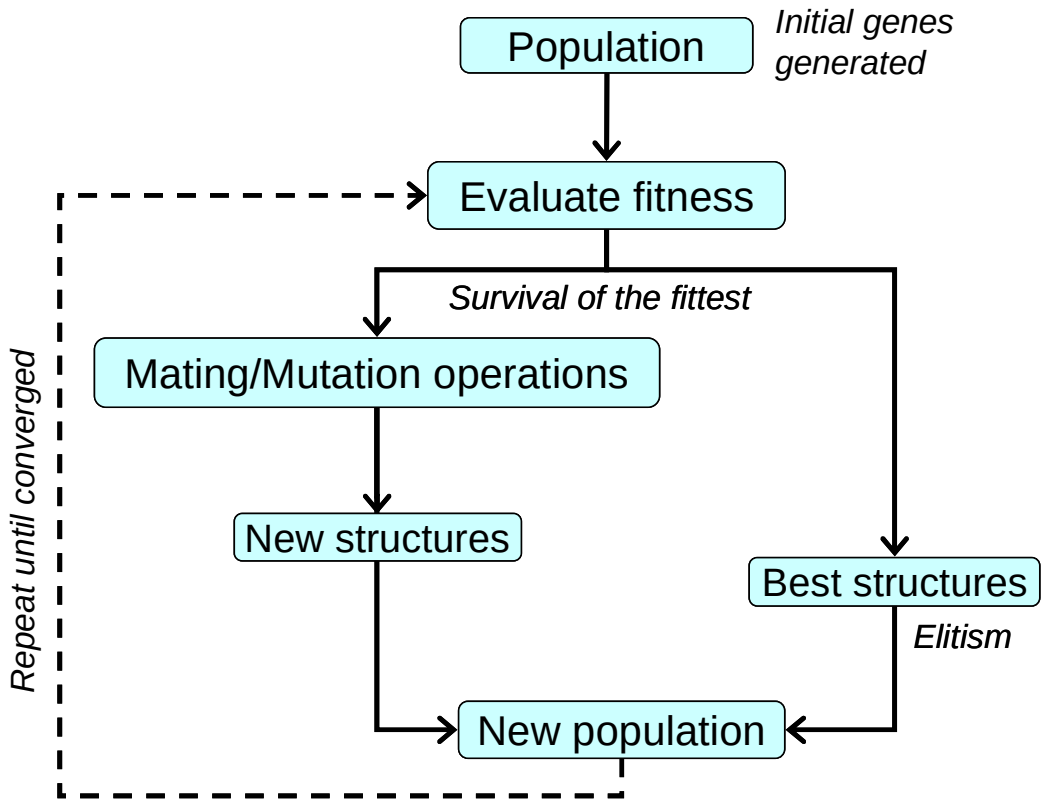

Figure 2–2. Genetic algorithm flowchart. In addition to the operations listed, 5 % of each new population contains randomly generated genes.

Sometimes after the mating and mutation routines create the child structures and elite structures are placed in the new genepool, there exist structures which have the same

fitness (i.e. degenerate structures). Initially, the program was set up to remove any degenerate structures, because it was believed that any two structures with the same energy must be structurally identical. This is actually true at concentrations of 3.2 and 6.6% SDC. In fact, an adjustable parameter called the 'resolution' allows the user to specify a small energy value, such as 0.001 eV, that the program uses to determine whether two structures are degenerate; if two structures' energies are within the specified resolution, then one was removed from the genepool.

However, at 10.3% and higher concentrations, energies of distinct configurations from the classical evaluation are so similar that the program cannot distinguish between them, even if the resolution is set to small values. Thus, an additional screening parameter was used: the Sm-vacancy distances. At these concentrations, in order to find all of the lowest-energy structures, which were nearly degenerate, the program was set up to evaluate the Sm-vacancy distances between two structures which had the same energy. If they were different, then both structures remained in the genepool. If they were the same, then one was removed. Several GA trials of bulk 10.3% SDC were run with this modified code (see Section 3.4 for details).

Later, it was noted that Sm-vacancy distances are not the single unique determinant of SDC configurations. For instance, it is possible to have two configurations, which are structurally different (in terms of Sm-Sm distances or vacancy-vacancy distances) yet have the same Sm-vacancy distances. Therefore, the GA was modified to account for this. Furthermore, we also noticed that the program often miscalculated the positions of the vacancies after the geometry optimization. A code was developed by James Hooper to correct the positions of the vacancies in the lattice. In the

latest version of the GA, if the energies of two structures fall within the specified resolution, the vacancies are first 'aligned' to their correct positions in both structures. Then, both configurations are tested on the basis of: Sm-Sm distances, Sm-vacancy distances, and vacancy-vacancy distances. If there exists one distance pair that is not identical, then the structures are different and both are kept in the genepool; otherwise, if every distance is the same (within a specified tolerance), then the structures are considered the same and so one is removed. The bulk 10.3% SDC GA trials were run again with the modified screening criteria, which properly accounts for defects in the lattice and differences between structures (see Section 3.4 for details).

As a final note, the bulk of the GA code was written by James Hooper. The major parts which I contributed include: extracting the atomic positions and lattice vectors from a GULP or VASP output file, writing new positions and lattice vectors to create a GULP or VASP input file, calculating and comparing the distances between defects in structures, and modifying the GA code to run on SHARCnet and HPCVL clusters. Importantly, the code is set up to run by itself on SHARCnet, as it can on Wooki. However, for large GAs requiring several CPUs, the algorithm can be run from Wooki, yet submit jobs for geometry optimizations to both Wooki and HPCVL computers. This is crucial for GAs with DFT(+U) optimizations, which require 16 CPUs per geometry optimization, but only 1 CPU for the main code. Also, I designed a special version of the code to search for high-energy structures, which involved a modification to the fitness. In Chapter 3, it will be made clear which version of the code is being used and for what reason. Finally, for the analysis of the GA results, I wrote codes which analyzed the distributions of defects within the best structures over several generations, which was

used to determine convergence in bulk and surface GA trials run on highly concentrated SDC.

2.1.1 - Interpreting GA Results

Above a 3.2 % dopant concentration, the number of possible configurations is so high that it is not feasible for a single GA trial of reasonable size to investigate all structures. In fact, at 6.6 % SDC, there exist 3.5 billion possible arrangements of dopants and vacancies in a 2x2x2 simulation cell, while at 10.3 % SDC, this number is 193 trillion. In comparison, the GA trials for these systems range from population sizes of 50 to 500, run for at most 600 generations. Thus, the best structures which emerge from a single GA trial of 6.6% or 10.3% SDC may not be the true lowest-energy structures in the entire material. It is more reliable to run multiple trials with the same parameters (i.e. same population size, run for the same number of generations) but with different random genes in the initial population and compare the best structures. If multiple independent trials find the same low-energy configurations, then it is more likely that these are indeed the lowest-energy configurations and less likely that a better structure has been overlooked.

The number of low-energy configurations from the GA that are chosen to be analyzed merits discussion. From their energy differences, we can assess the relative distribution of low-energy configurations at various temperatures. Using the IT-SOFC temperatures as a guide, we should be concerned with the structures that will be populated at temperatures between 400 and 600 Celsius. The Boltzmann distribution of configurations present at these temperatures will give a realistic description of the material. Thus, it is imperative to analyze the configurations which lie within kT at these

temperatures. After the relevant configurations are found, we attempt to look for qualitative similarities amongst the relevant structures to deduce what atomistic interactions will be dominant in the fuel cell.

2.1.2 - Tandem Genetic Algorithm

In order to accurately determine the energy differences amongst low-energy configurations, it is imperative to use a high level of theory in the energy evaluations. Such an accurate electronic structure method is provided by density functional theory which better describes the electronic structure compared to classical simulations. To further improve upon this description for lanthanides, it is generally accepted to add a Hubbard correction (or U term) to the DFT formalism. However, due to the computational expense of DFT and DFT+U calculations, it is not feasible to employ such high-level calculations in the GA, with so many structures to evaluate. To solve this problem, a dual level or 'tandem' approach to the algorithm was made. In the first stage, the large structure space is sufficiently searched using the low level, classical calculation to define the fitness of each structure. Multiple classical GA trials are run until reproducible results are obtained, and the best structures are well known. Subsequently, these elite structures become part of the population of a new GA trial which uses the high level DFT(+U) calculation as the fitness. The initial stage of the tandem GA is designed to screen out high-energy configurations, so that the final stage can proceed with only good candidates. Because the DFT(+U) GA begins from an already fit genepool, it does not need to be run for as many generations as the classical GAs to reach convergence. In this way, the DFT(+U) GA will find the lowest-energy structures and rank them accurately, without needing a large population size.

A number of tests and results were done to validate the tandem GA search method, which are presented in Section 3.1.

Section 2.2 - Computational Details

Two main software packages were used for the optimization of geometries in this work. The classical simulations were done with the General Utility Lattice Program (GULP)[5] and the first principles DFT simulations were done with the Vienna ab initio Simulation Package (VASP)[6, 7]. The latter code was also used for determination of activation energies in oxygen diffusion pathways, as well as electronic properties like the density of states. However, most of the calculations for this thesis involve simple geometry optimizations to local minima on a potential energy surface. The details are described in Section 2.2.1.

2.2.1 - Energy Evaluations

The classical calculations involve short range pair-wise Buckingham potentials and an Ewald summation[8] of long range interactions. The potential is shown in equation (1). The shell model[9] was used to account for the polarizability of the O^{2-} ions. This model involves a massless shell potential of negative charge attached to a massive core of slightly positive charge, to simulate a mobile electron cloud around a relatively stationary nucleus. The oxygen shell had a charge of -2.08 e and was tied to the atomic core by a 27.29 eV/Å^2 spring constant. The Buckingham parameters, shown in Table 2–1, were taken from Balducci *et al.*[10] and Senyshyn *et al.*[11] The functions were evaluated between 0.5 and 10 Å for Ce-O and O-O pairs and between 0.5 and 6 Å for Sm-O pairs. The

elevation of the lower cutoff from 0.0 to 0.5 Å was employed to help eliminate unphysical structures from our genetic algorithm; it should in no way affect the energies of relevant configurations.

$$S_{ij} = Ae^{\left(-r_{ij}/\rho\right)} - \frac{C}{r_{ij}^6} \quad (1)$$

Table 2–1. Buckingham parameters for interatomic potentials[10, 11]

Species	*A (eV)*	*ρ (Å)*	*C (eV·Å^6)*
O^{2-} - O^{2-}	22764.3	0.149	27.89
Ce^{4+} - O^{2-}	1986.8	0.3511	20.40
Sm^{3+} - O^{2-}	4040.9	0.3034	0.0

In addition to the above parameters, we also used the force field parameters of Wei *et al.*[12] who performed a systematic evaluation of 3.2 % lanthanide-doped ceria. The two sets of potentials were compared to more accurate calculations, at various concentrations of dopant (see Section 3.1 for details). The potentials taken from Wei *et al.* contain a shell potential on both Ce^{4+} and O^{2-} ions, which are attached to their respective cores by 177.74 and 6.3 eV/Å^2 spring constants, respectively. The Ce^{4+} shell has a charge of -0.2 e and the O^{2-} shell has a charge of -2.04 e. Also, the Buckingham functions (shown in Table 2–2) were evaluated between 0.0 and 20.0 Angstroms. In addition to Sm-doped ceria, Gd- and Lu-doped ceria were studied with these potentials.

Table 2–2. Buckingham parameters for interatomic potentials from Wei *et al.*[13-15]

Species	*A (eV)*	*ρ (Å)*	*C (eV·Å^6)*
O^{2-} - O^{2-}	9547.96	0.2192	32.00
Ce^{4+} - O^{2-}	1809.68	0.3547	20.40
Sm^{3+} - O^{2-}	1944.44	0.3414	21.49
Gd^{3+} - O^{2-}	1885.75	0.3399	20.34
Lu^{3+} - O^{2-}	1618.80	0.3385	19.27

All DFT and DFT+U calculations were performed with the Vienna ab initio simulation package (VASP).[6, 7] The exchange-correlation effects were described with the Perdew Burke Erzenhof (PBE) functional[16] within the generalized gradient approximation (GGA). The PBE functional has been used in the past for DFT calculations of similar systems,[17] and has been shown to be better for simulating solids than other GGA and semi-empirical functionals.[16, 18, 19] In the DFT+U method, a Hubbard (U-term) correction is added to the conventional Kohn-Sham Hamiltonian to more correctly account for the localization of strongly correlated electrons, and to mitigate the self-interaction error present in conventional DFT. A U-value of 5 eV was placed on all cerium ions, which is consistent with previous studies of doped ceria.[20-24] No such correction is needed on samarium because the f electrons were placed in the core, and hence are already localized. Pseudopotentials were generated with the projector augmented wave (PAW) method.[25] The cerium $5s^2$, $5p^6$, $6s^2$, $5d^1$, and $4f^1$ states, as well as the samarium $5s^2$, $5p^6$, $6s^2$, and $5d^1$ states, and the oxygen $2s^2$ and $2p^4$ states were treated as valence electrons, whereas the others were frozen in the core. Currently all electronic structure calculations of lanthanide-doped ceria employ the same methodology as in the

majority of this work, where the f electrons of the dopant are placed in the core of the pseudopotential.[20, 21]

Structures were relaxed until the forces on each ion were below 0.02 eV/Å and the total energy was converged within 0.01 meV. The energies from an optimization run cannot be trusted due to the fact that after cell relaxation, the PAW basis vectors are no longer orthogonal. Thus, a static run (where the ions are not moved) is always done, starting from the optimized structure, to get the energy. A 520 eV plane-wave cutoff energy was used throughout. Studies of similar compounds using VASP have employed a plane-wave cutoff of 400 eV that were found to be converged to approximately 0.01 meV.[20, 21, 26] Other standard features include a variable cell, spin polarization, and Gaussian smearing of 0.20 eV. Although the magnetization was not fixed in these calculations, it was found that all electrons were paired following relaxation.

For the DFT+U calculations of Chapter 3 and Chapter 5, the VASP calculations were done as described above. For the electronic structure analysis in Chapter 4, it was necessary to treat the 4f electrons of samarium as valence and parameterize the value of U for Sm, in order to match our calculations with experiment. These calculations are described in Section 2.2.3.

2.2.1.1 - Exploration of Faster DFT Calculations

Because VASP calculations used significant CPU time and resources, various techniques were tried to improve the calculation time. First, instead of using the plane wave approach implemented in VASP, a smaller basis set which employs atomic-centered functions implemented in the Spanish Initiative for Electronic Simulations with Thousands of Atoms (SIESTA)[27] program was used. However, for this system,

pseudopotentials are difficult to develop and test. The pseudopotentials used were taken from an online database available for SIESTA users. It was found that the DFT-calculated energies of all configurations of 3.2 % SDC did not correlate with the energetics from the classical optimizations. Also, the improvement in CPU time was not significant compared to VASP. Thus, the SIESTA program was not be used in our search algorithm.

Other methods to improve the VASP calculation included a smaller k-point grid. Using the 3x3x3 Monkhorst-Pack k-point grid, a single DFT optimization takes days to run on 16 parallel processors on Wooki. Yet, with just the Gamma point, the same optimization completes in approximately 8 hours on the same number of processors. It was found that the energy evaluations with the Gamma k-point overall reproduces the same trend in energies with a 3x3x3 k-point grid for doped ceria configurations, so it sufficed to use just the Gamma point in the GA energy calculations. For accurate energy differences and electronic properties such as density of states calculated outside of the genetic algorithm, the larger k-point grid was used. It was also found that calculations with the 3x3x3 k-point grid produced a very different density of states plot than the same calculation with just the Gamma point. For the size of the system being studied, a 3x3x3 k-point grid should be sufficient.

2.2.2 - Activation Energy Calculations

To calculate the activation energy of oxygen ion migration in the SDC lattice, first principles DFT+U calculations were used as implemented in the VASP code. The computational details are the same as the DFT+U calculations in the genetic algorithm, where a Hubbard correction of 5 eV is applied to Ce, but not to Sm, whose f electrons are

placed in the core. To calculate activation energies for oxygen vacancy migration, we adopt the same procedure as that of Andersson *et al.*[26] and Dholabhai *et al.*[20, 21] The activation energy is given by the difference between the total energy of the system before migration and the saddle point energy determined from first principles DFT+U calculations. The saddle point positions were chosen as the midpoint along the line joining the initial and final sites for the migrating ion. The migrating ion was allowed to relax in both directions perpendicular to the migration path to ensure the optimal saddle point positions are found. To ensure that the actual highest energy point is indeed the midpoint structure, additional calculations were performed where the ion was shifted slightly from the midpoint. These calculations showed that the midpoint is truly the highest-energy position.

2.2.3 - Density of States Calculations

For the density of states, static calculations were performed on previously-optimized structures of SDC and pure ceria, using a number of formalisms implemented in VASP. Also, a reduced 6.6% SDC lattice was made, which contained two trivalent Ce ions, to attempt to reproduce experimental data on reduced SDC. Part of the study here was to test the difference between calculated DOS plots using various methods. The methods include: conventional DFT, DFT+U with U_{Ce} but no U_{Sm}, DFT+U with U_{Ce} and varying U_{Sm} values, and hybrid DFT calculations. The first two types have been explained above. Various values of U_{Sm} (2, 4, 5, 6, 8, 10, 12, 14, and 16 eV) were tried to attempt to reproduce experimental data. In these calculations, the 16 electron pseudopotential of Sm was used, which includes the 4f electrons as valence. The value of U_{Ce} stayed constant at 5 eV, because it has already been parameterized for ceria.

To optimize structures with DFT+U where U_{Sm} is included, it was necessary to employ a 400 eV plane-wave cutoff energy. With larger cutoffs the electronic structure did not converge. Studies of similar compounds using VASP have employed the same 400 eV cutoff which was found to be converged to approximately 0.01 meV.[20, 21, 26] Furthermore, for the static calculations, it was necessary to begin from the optimized wavefunctions and charge densities from the VASP optimization. Without this, VASP begins from a random guess at the wavefunction, which it is unable to converge. With the exception of these differences, all other aspects of the DFT+U calculation were the same as described in Section 2.2.1.

As an alternative to the Hubbard correction, hybrid DFT calculations that use exchange-correlation functionals which employ a percentage of Hartree-Fock exchange are a possible solution to the self-interaction error present in conventional DFT. We tried these calculations for ceria and for SDC, although they were found to be very computationally demanding, requiring as many as 256 parallel CPUs. As this is a relatively new method, the implementation of it in the VASP program has not been fully optimized. Several computational errors were encountered, which were documented by other VASP users as well,[28] and convergence was never achieved for the SDC system, only for pure ceria. Thus, no results from these hybrid DFT calculations are presented in this thesis.

Section 2.3 - References

1 S. M. Woodley and R. Catlow, *Nat Mater*, 2008, **7**, 937-946.
2 A. R. Oganov and C. W. Glass, *J. Chem. Phys.*, 2006, **124**, 244704.
3 J. Hooper, A. Hu, F. Zhang and T. K. Woo, *Phys. Rev. B*, 2009, **80**, 104117.

4 J. Hooper, Ph.D. Thesis, University of Ottawa, 2010.
5 J. D. Gale, *J. Chem. Soc. Faraday Trans.*, 1997, **93**, 629.
6 G. Kresse, Furthmuller, J., *Comput. Mater. Sci.*, 1996, **6**, 15.
7 G. Kresse and J. Hafner, *Phys. Rev. B*, 1993, **47**, 558.
8 P. P. Ewald, *Ann. Phys.*, 1921, **64**, 253-287.
9 J. D. Gale, *Phil. Mag. B*, 1996, **73**, 3.
10 G. Balducci, J. Kaspar, P. Fornasiero, M. Graziani and M. S. Islam, *J. Phys. Chem. B*, 1998, **102**, 557.
11 A. Senyshyn, A. R. Oganov, L. Vasylechko, H. Ehrenberg, U. Bismayer, M. Berkowski and A. Matkovskii, *J. Phys.: Condens. Matter*, 2004, **16**, 253.
12 X. Wei, W. Pan, L. Cheng and B. Li, *Solid State Ionics*, 2009, **180**, 13.
13 R. W. Grimes, Busker, G., McCoy, M. A., Chroneos, A., Kilner, J. A., *Ber. Bunsen-Ges. Phys. Chem.*, 1997, **101**, 1204.
14 L. Minervini, Grimes, R. W., Sickafus, K. E., *J. Am. Ceram. Soc.*, 2000, **83**, 1873.
15 S. Vyas, R. W. Grimes, D. H. Gay and A. L. Rohl, *J. Chem. Soc. Faraday Trans.*, 1998, **94**, 427.
16 J. P. Perdew, K. Burke and M. Erzenhof, *Phys. Rev. Lett.*, 1996, **77**, 3865.
17 M. Nakayama and M. Martin, *PCCP*, 2009, **11**, 3241.
18 S. Kurth, J. P. Perdew and P. Blaha, *Int. J. Quantum Chem.*, 1999, **75**, 889-909.
19 I. H. Lee and R. M. Martin, *Phys. Rev. B*, 1997, **56**, 7197-7205.
20 P. P. Dholabhai, J. B. Adams, P. Crozier and R. Sharma, *J. Chem. Phys.*, 2010, **132**, 094104.
21 P. P. Dholabhai, J. B. Adams, P. Crozier and R. Sharma, *PCCP*, 2010, **12**, 7904.
22 M. Nolan, V. S. Verdugo and H. Metiu, *Surf. Sci.*, 2008, **602**, 2734.
23 Z. Yang, G. Luo, Z. Lu and K. Hermansson, *J. Chem. Phys.*, 2007, **127**, 074704.
24 Z. Yang, Luo, G., Lu, Z., Woo, T. K., Hermansson, K., *J. Phys.: Condens. Matter*, 2008, **20**, 035210.
25 P. E. Blochl, *Phys. Rev. B*, 1994, **50**, 17953.
26 D. A. Andersson, S. I. Simak, N. V. Skorodumova, I. A. Abrikosov and B. Johansson, *Proc. Natl. Acad. Sci. U.S.A.*, 2006, **103**, 3518-3521.
27 J. M. Soler, E. Artacho, J. D. Gale, A. Garcia, J. Junquera, P. Ordejon and D. Sanchez-Portal, *J. Phys.: Condens. Matter*, 2002, **14**, 2745-2779.
28 D. Vogtenhuber, Ionic relaxation problem (VASP 5.2.11), VASP support site, 2011.

CHAPTER 3 - INVESTIGATING LOW-ENERGY CONFIGURATIONS OF SAMARIUM-DOPED CERIA

This chapter focuses on identifying low-energy bulk structures of doped ceria at various dopant concentrations. Systematic and GA search results will be presented, and the usefulness and credibility of the GA will be justified. The structural qualities amongst low-energy configurations of SDC are identified and are used to rationalize its high ionic conductivity. Wherever possible, theoretical results are compared to experiment.

A lot of the work in this chapter has been published in peer-reviewed scientific journals. The results of Sections 3.1, 3.2, and 3.3 are published in: *Physical Review B*, **2010**, *81*, 224104 (1-11) and *Physical Chemistry Chemical Physics*, **2011**, *13*, 6116-6124. We are currently preparing a manuscript for the results of Sections 3.4 to 3.6. For a complete list of thesis-related publications, refer to Section 6.3.

Section 3.1 - Systematic Search of 3.2% LDC

In this section, we perform a systematic search of all possible configurations of 3.2% Lanthanide-doped ceria, using classical and DFT levels of theory. The classical potentials are compared to more accurate electronic structure calculations in order to justify the tandem GA method, used at higher concentrations. The implications of using accurate calculations are discussed in detail, with regards to 3.2% samarium-doped ceria structures. In addition to Sm, we substituted Gd and Lu dopants in ceria, to assess the differences in defect association amongst ions in the lanthanide series. Previously, Andersson *et al.*,[1] Muthukkumaran *et al.*,[2] and Nakayama and Martin[3] studied migration barriers in the same materials using DFT; while their results are accurate, not all possible

configurations of the material were sampled, so it may be possible that a relevant migration path was overlooked. In contrast, Wei *et al.*[4] performed a systematic search for all lanthanide ion dopants in ceria, although with classical potentials. Thus, a systematic search at a high level of theory is lacking in the literature and is needed in order to accurately assess defect association in doped ceria. It is known from experiment that samarium and gadolinium dopants greatly improve the ionic conductivity of ceria, whilst smaller rare-earth metal dopants like lutetium do not.[5] We investigate the low-energy structures of these materials to determine what structural properties influence conductivity.

Figure 3–1 displays the undoped, 2x2x2 simulation cell of ceria, which consists of 64 oxygen and 32 cerium atoms. The dopant concentration of 3.2% of the doped oxide is easily simulated in a 2x2x2 cell of ceria because only one oxygen vacancy and two dopant atoms need to be placed in the cell. Due to symmetry, all of the oxygen positions are identical, so the position of the vacancy is irrelevant; this leaves only two dopant atoms to be placed, which, after symmetry is considered, correspond to just 33 unique configurations. Clearly, it is feasible to simulate all of these configurations at the classical and DFT(+U) levels of theory.

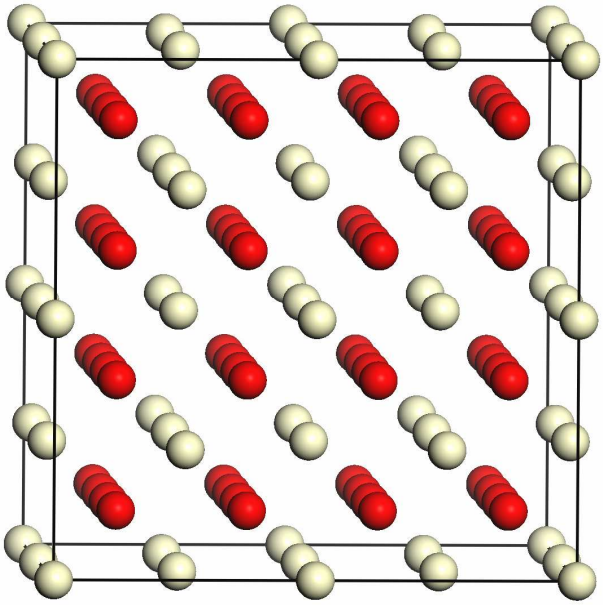

Figure 3–1. A 2x2x2 simulation cell of ceria. The white balls represent Ce^{4+} ions and the red balls represent O^{2-} ions.

The classical potentials for cerium and oxygen ions from Balducci *et al.*[6] in combination with the potentials for samarium ions of Senyshyn *et al.*[7] make up the primary classical force field used in this work. An exhaustive evaluation of all possible configurations of 3.2% SDC was done with these potentials. We compare our results to those of Wei *et al.*[4], who used a different force field and a slightly different optimization. Instead of the constant pressure geometry optimization used in this work, Wei *et al.* uses the Mott-Littleton method,[8] which divides the cell into two regions, and calculates the defect interaction energy between them at constant volume. Overall, both methods attempt to find the same information, which is the defect association energies of all configurations. Differences in the potentials may play a crucial role in the results.

In the structural analysis of doped metal oxides, configurations are often distinguished by the unique distances between their defects, which in this case are dopant atoms and oxygen vacancies. The first coordination shell around the vacancy is known as

the nearest neighbour (NN) shell, the second one is the next nearest neighbour (NNN) shell, and so on. For example, a configuration where both dopant ions lie in the first coordination shell around the vacancy is called "NN-NN". In 3.2% LDC, the 33 unique configurations can be distinguished by the two dopant-vacancy distances, as well as the distance between the two dopant atoms.

Wei *et al.*[4] predicts that in SDC, Sm prefers the NNN site next to the vacancy, as the two lowest-energy structures have the NNN-NNN configuration, with the dopant atoms separated by at least 6.7 Angstroms. In contrast, the hybrid NN-NNN configuration with a 6.7 Å distance between dopant atoms is preferred by our chosen force field, with the NN-NN configuration being second best. Wei *et al.* ranks the NN-NNN and NN-NN configurations as third and sixth best, respectively, where the relative association energy of the NN-NN structure is greater than 0.1 eV above the lowest-energy structure. This is a significant difference in energetics, which could be due to the fact that the Buckingham parameters are different, and/or the optimization schemes are different in our study versus Wei's.

To assess how the difference in optimization affects the results, a systematic search was performed using the potentials of Wei *et al.*, with the same optimization in GULP that was used for the other set of potentials. We find that our search results correlate fairly well with the results in ref. 4, meaning that the difference in optimization scheme does not significantly affect the results. Rather, it is only the difference in Buckingham parameters that causes the discrepancies described above. The constant pressure optimization ranks the structures the same way the constant volume Mott-Littleton optimization does, as we find the same energy differences between

configurations as Wei *et al*. The only exception was that, in our systematic search with Wei's potentials, three different configurations (with different energies) were found for the NNN-NNN structure where the dopant ions lie 3.8 Å apart. The structures differed due to the in-plane oxygen relaxations around the vacancy, which were not identical depending on where the Sm atoms were situated in the cell. In ref. 4, Wei *et al.* seems to treat these three structures as separate configurations, even though they have the same Sm-Sm and Sm-vacancy distances when one takes into account periodic boundary conditions. We found one such NNN-NNN configuration to be just 0.016 eV higher than the lowest-energy structure, ranking it third best amongst all configurations, although with the Mott-Littleton method it was much higher in energy. The fact that the constant pressure geometry optimization ranks all but one structure the same as the constant volume Mott-Littleton optimization, shows that the optimization scheme does not play a big role in determining the difference between our results and those of Wei *et al.* Evidently, the differences in Buckingham parameters account for the discrepancies.

In order to determine which set of potentials is more accurate, we compare them to higher level electronic structure calculations (see section 3.1.1). This will also serve to validate the use of one set of parameters in our tandem GA, which is needed for dopant concentrations above 3.2%.

As mentioned previously, a systematic search at a high level of theory is needed in order to identify the structural trends amongst low-energy structures in doped ceria with a greater degree of accuracy. We chose to study samarium-doped ceria because it has the highest ionic conductivity of all singly doped ceria materials,[1, 2] and is therefore the most interesting to fuel cell scientists. Density functional calculations on all unique

configurations of SDC were performed with and without the Hubbard (U) correction added to cerium ions. The DFT+U method has emerged as the method of choice for simulating doped ceria, due to its accurate treatment of the electronic structure surrounding lanthanide ions. Yet, the DFT method is much less computationally expensive, and in the interest of time it was tried first. Both sets of results are presented below, and the implications of using the more accurate calculation are discussed.

The structural information and energetics of the best nine configurations from the DFT+U systematic search are shown in Table 3–1. For comparison, DFT energies are also provided; comparison to the classical potentials is done later in section 3.1.1.

Table 3–1. Relative energies and structural information of the best 3.2% SDC structures

Structure	ΔE_{DFT+U} [a,b] *(eV/cell)*	ΔE_{DFT} [a,c] *(eV/cell)*	*Sm-Sm distance*[d] *(Å)*	*Sm-vacancy distance*[e] *(Å)*
S1	0.000	0.007	3.8	NN-NN
S2	0.032	0.000	6.6	NN-NNN
S3	0.068	0.083	5.4	NN-NNN
S4	0.081	0.042	3.8	NN-NNN
S5	0.095	0.112	7.6	NN-NNNN
S6	0.098	0.125	6.6	NN-NNNN
S7	0.106	0.028	7.6	NNN-NNN
S8	0.109	0.023	6.6	NNN-NNN
S9	0.132	0.107	3.8	NNN-NNN

[a] Energies reported are relative to the lowest energy structure of the given potential. [b] Relative total electronic energies from DFT+U calculations. [c] Relative total electronic energies from DFT calculations. [d] Sm-Sm distance reported is taken from the ideal lattice before geometry relaxation. [e] NN distance is approximately 2.4 Å, NNN ~ 4.5 Å, and NNNN ~ 5.9 Å.

Recent works by Wei *et al.*[4] and Nakayama *et al.*[3] predicted that a crossover from NNN to NN dopant site preference across the lanthanide series occurs at Gd^{3+}, and for

Gd-doped ceria itself there is no preference, using classical and DFT calculations. However, a recent DFT+U study of Gd-doped ceria by Dholabhai *et al.*[9] found that the NN site is actually preferred by the dopant by 0.14 eV/cell. Since Sm is close to Gd in the Lanthanide series, the NN site might also be preferred at the DFT+U level. Indeed, Table 3–1 shows that structure **S1**, which has exclusive NN occupation, is optimal for 3.2% SDC at the DFT+U level, while at the DFT level, structure **S2**, which is a hybrid NN-NNN structure, is the most stable. The NN preference at the DFT+U level is further illustrated by the fact that the lowest 6 structures (**S1**-**S6**) sport at least one NN interaction. In contrast, at the DFT level structures **S7** and **S8**, which contain exclusive NNN interactions, are the third and fourth most stable structures, respectively. It is also worth noting that structures **S7** and **S8** are high energy structures at the DFT+U level, lying over 0.1 eV/cell above the lowest energy structure (**S1**).

Accurate treatment of the electronic structure is crucial, as dopant-vacancy interaction is known to have a non-negligible electronic component.[4, 10] The proper description of localized f electrons around Ce^{4+} nuclei in the DFT+U formalism most likely accounts for the difference between DFT+U and DFT results listed above.

However, overall the two methods correlate fairly well. In fact, among all 3.2% configurations, there is a linear relation between DFT and DFT+U energy (see Figure 3–2). This shows that plain DFT reproduces the same general trend in the dopant-vacancy association energies as the more accurate DFT+U calculations. While this result indicates promise for lower level calculations, it is important to remember that the correlation is not perfect, and that there are discrepancies which are manifested in the structural properties of the best configurations (explained above).

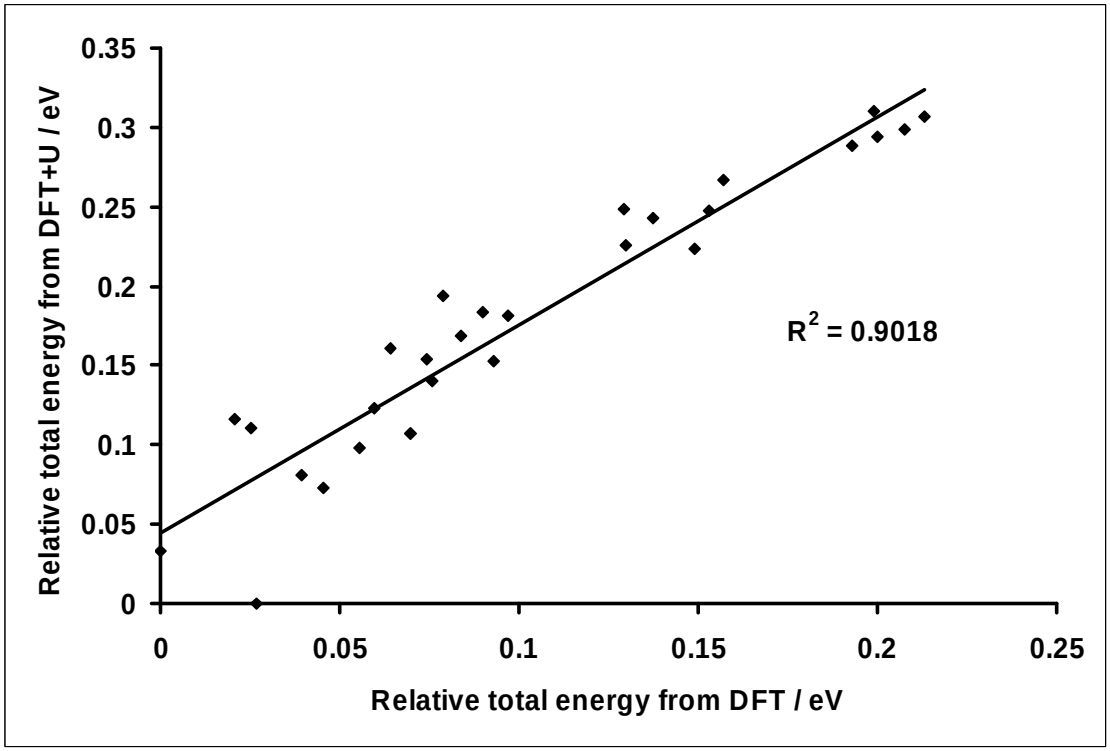

Figure 3–2. Correlation between the DFT and DFT+U relative energies of the unique 3.2% SDC structures. The energies of all structures are relative to the lowest-energy structure from each method, which is assigned a value of 0.

The NN preference of Sm at the DFT+U level is in agreement with the DFT calculations of Andersson *et al.*;[1] although, at the DFT level, we found the best structure to be a NN-NNN configuration, which Andersson did not consider. In contrast, Wei *et al.* performed an exhaustive search and predicted a NNN preference for the Sm ion.[4] Due to the higher accuracy of the DFT+U method over classical potentials, it is safe to trust the DFT+U results presented here over other calculations. In Section 3.1.1, which compares classical potentials to electronic structure calculations, the pitfalls of Wei *et al.*'s Buckingham parameters are illustrated. In a DFT study, Nakayama and Martin found that the NN Sm-vacancy interaction is not favourable,[3] which contradicts our findings. However, in their work, the authors do not consider the second dopant ion in the simulation cell, which has drastic influence on the overall association energy. For

instance, we found that NN-NN configuration is quite different in energy than the NN-NNNN configuration (where only one ion is at a different distance with respect to the vacancy), and furthermore, that the different Sm-Sm distances also affect the association energy. Thus, it is difficult to compare our results with those of Nakayama and Martin because they were interested in identifying the association of a vacancy with a single dopant ion, whereas we identified the association of a vacancy with two dopant ions, as in the real 3.2% SDC material.

Relying on the most accurate simulations, it is clear that Sm favours the NN site around the vacancy in 3.2% SDC. A more thorough comparison of the classical potentials with DFT and DFT+U systematic searches is presented in the following section, as well as the results for Gd- and Lu-doped ceria; these results will also serve to validate the tandem GA method. Section 3.1.2 contains the first tests of the genetic algorithm done at the 3.2% concentration.

3.1.1 - Tandem GA Validation

A systematic search of all 3.2% SDC configurations was completed at the DFT and DFT+U (U_{Ce} = 5 eV) levels of theory, in order to benchmark the classical potentials used previously. In Figure 3–3 and Figure 3–4 (below), the Balducci[6] and Senyshyn[7] force field is compared to higher level calculations. Here we are concerned with validating the tandem GA by showing the correlation between a set of classical potentials and a higher level calculation.

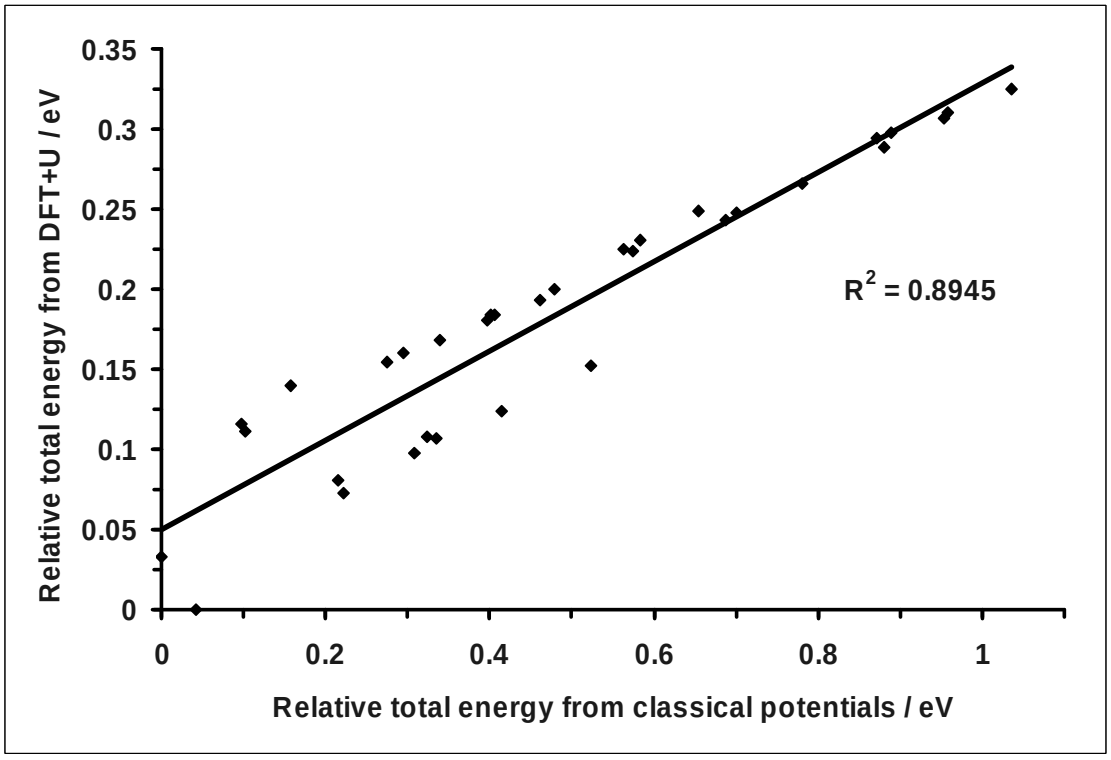

Figure 3–3. Correlation between the classical[6, 7] and DFT+U relative energies of the unique 3.2% SDC structures. The energies of all structures are relative to the lowest-energy structure from each method, which is assigned a value of 0.

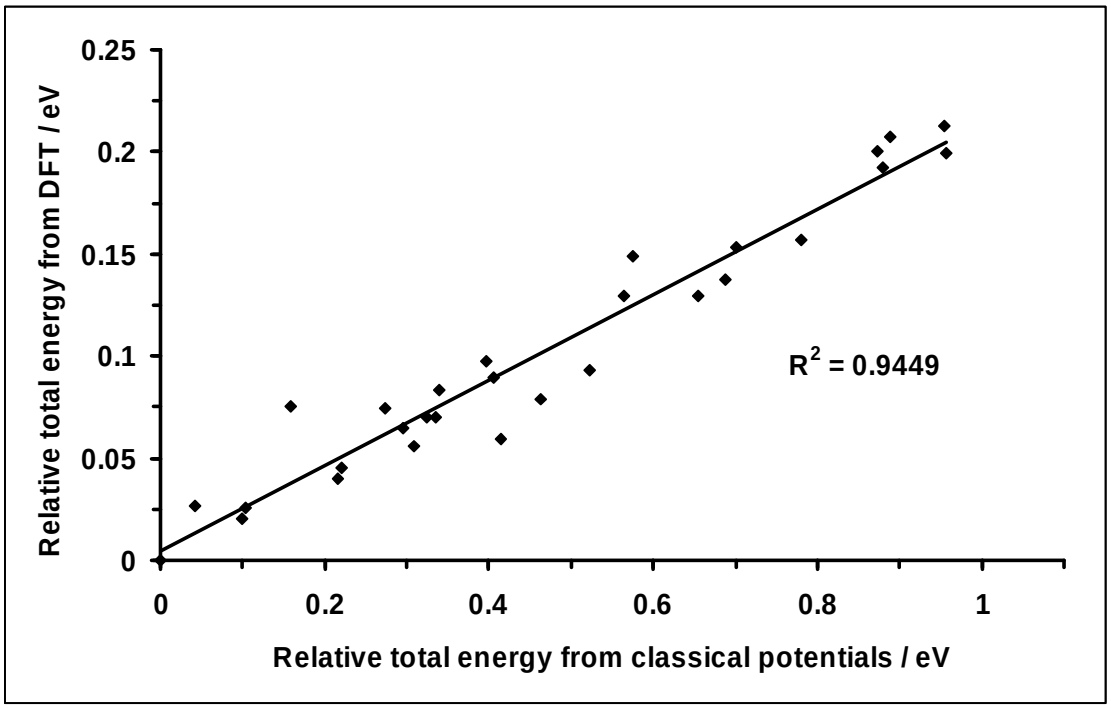

Figure 3–4. Correlation between the classical[6, 7] and DFT relative energies of the unique 3.2% SDC structures. The energies of all structures are relative to the lowest-energy structure from each method, which is assigned a value of 0.

Clearly, the structures that are low-energy with the classical potentials of Balducci *et al.*[6] and Senyshyn *et al.*[7], are also low-energy with the higher levels of theory. The same holds true for the high-energy structures, which means that the classical potentials can be used in the first step of the tandem GA to eliminate high-energy configurations from the genepool.

It is interesting to observe that this force field seems to correlate a bit better with DFT than with DFT+U, as the R-squared values suggest. In fact, the force field agrees quite well with DFT especially at low-energies, where most configurations have predominantly NNN interactions. In DFT+U, NNN configurations are not favoured, as discussed above, and thus these structures lie above the line in Figure 3–3. The configurations with a Sm NN to the vacancy lie below the line in Figure 3–3, indicating the DFT+U-preferred interaction, which is not perfectly represented in the classical

scheme. Overall however, the finding that this force field correlates slightly better with DFT than with DFT+U is not significant from a computational standpoint; it does not affect the validity of the tandem GA at all.

A closer analysis of Figure 3–3 and Figure 3–4 reveals that there are a few structures which are predicted to be low-energy by the classical scheme, yet are high-energy as ranked by the DFT(+U) calculation. These points represent false positives, which are not ideal, yet are fairly easy to deal with in the tandem GA. In the first generation of the DFT(+U) GA, any high-energy structures that were read in from the first step are removed from the genepool due to their newly assigned low fitness. More importantly, there exist no false negatives with this approach. In other words, there are no configurations that the classical force field predict to be high-energy, yet are actually low-energy in a DFT(+U) calculation. For the purpose of our tandem GA, where several configurations are initially removed from consideration in the first stage, it is critical that none of these structures prove to be low-energy in a DFT(+U) calculation.

Since the correlation between the chosen classical force field and DFT(+U) is not perfect, it is important that near the end of the GA - that is, once the screening of numerous structures is complete - a higher level calculation accurately assess the energy differences between the best candidates. A structure search solely at the classical level of theory is not entirely reliable due to the existence of false positives, as illustrated above.

Using the systematic search results, the classical force field of Wei *et al.*[4] was also tested against DFT and DFT+U calculations. These results are shown in Figure 3–5 and Figure 3–6.

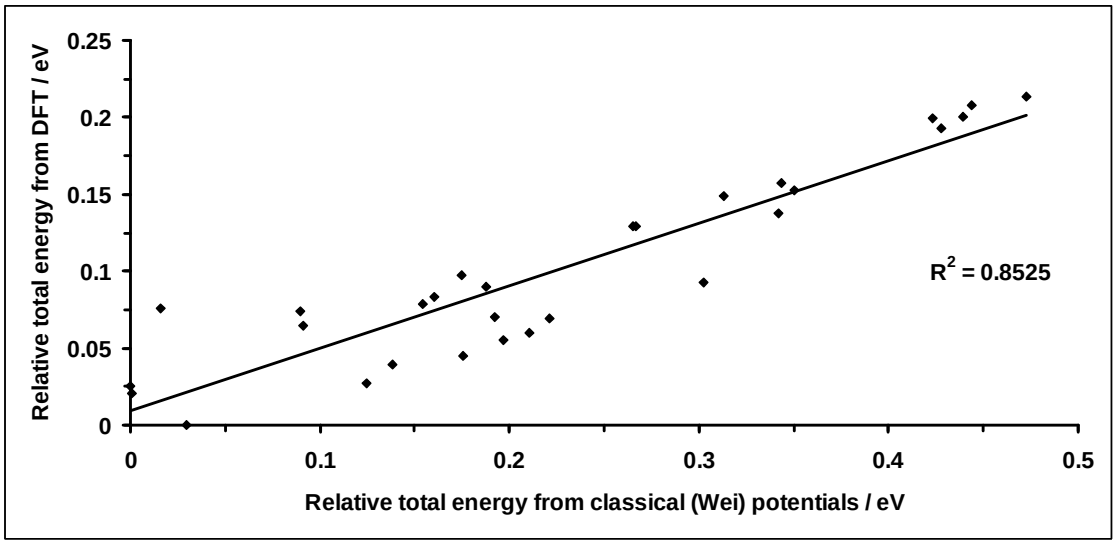

Figure 3–5. Correlation between the classical[4] and DFT relative energies of the unique 3.2% SDC structures. The energies of all structures are relative to the lowest-energy structure from each method, which is assigned a value of 0.

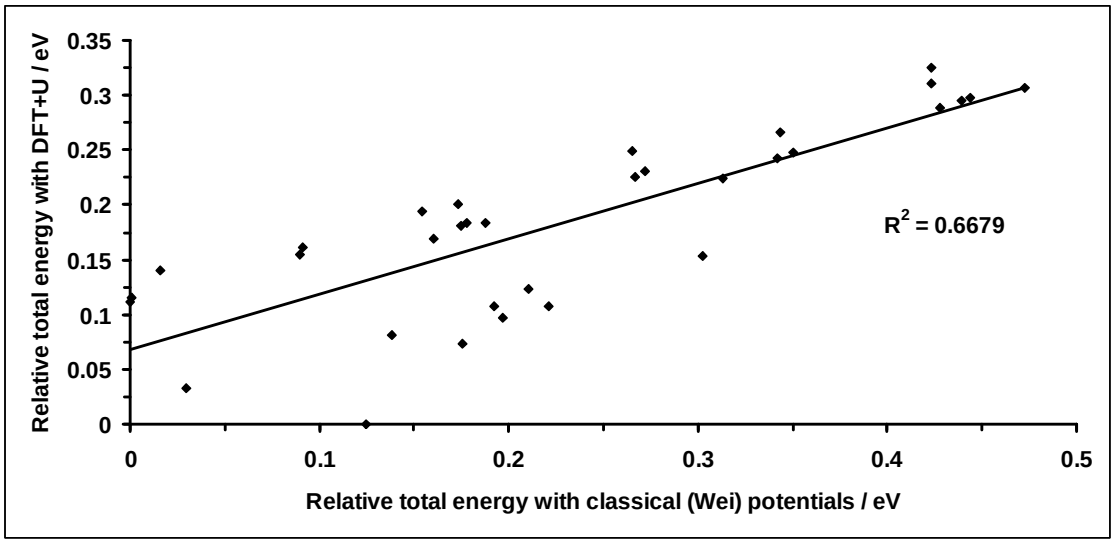

Figure 3–6. Correlation between the classical[4] and DFT+U relative energies of the unique 3.2% SDC structures. The energies of all structures are relative to the lowest-energy structure from each method, which is assigned a value of 0.

The R-squared values of 0.85 and 0.67 are much lower compared to those obtained with the other force field, indicating that the parameters of Wei *et al.* do not correlate

nearly as well as the Balducci/Senyshyn parameters with high level calculations. Especially troublesome is the configuration in Figure 3–6, which was assigned a high-energy of 0.30 eV in the classical scheme yet is actually 0.15 eV above the lowest-energy structure in DFT+U. This and other points well below the line of best fit illustrate that, if Wei's potentials were used in the first stage of the tandem GA, the screening of unfavourable configurations would not be very accurate, that is, low energy configuration would be prematurely rejected.

In summary, the accurate calculations provided a means of testing whether or not a lower level calculation performs well. Overall, the results indicate that the potentials of Balducci *et al.*[6] and Senyshyn *et al.*[7] should be used for the first stage of the tandem GA.

The correlation between various calculation methods was shown for 3.2% SDC only because it is the only concentration at which such a comparison is feasible to calculate. At higher concentrations, there are too many structures to evaluate systematically at a high level of theory. However, because the system is generally the same, we expect that the correlation will hold at higher concentrations. Although the correlation cannot be evaluated exhaustively, we perform test calculations to justify this assumption in later sections.

3.1.2 - Initial GA Tests

Here we present the first tests of the genetic algorithm on 3.2% lanthanide-doped ceria materials. These tests are designed to assess the GA's ability to find low-energy configurations for a variety of potential energy surfaces. Using the potentials from Wei *et al.*,[4] we compare the GA results to the systematic search results by Wei *et al.* for Sm-, Gd-, and Lu-doped ceria. Also, for SDC, we perform a GA using the parameters from

Balducci *et al.*[6] and Senyshyn *et al.*[7] and compare to our systematic search results from those potentials. Finally, we performed DFT optimizations on the best ten favoured structures from the classical GAs and compare to the systematic search with DFT energetics.

Recall that at concentrations higher than 3.2%, it is unfeasible to evaluate all possible configurations, thus a GA result at these concentrations cannot be compared to a systematic search result. For these GAs, we will need some other form of validation. This will be presented in future sections.

Using the classical potentials of Balducci[6] and Senyshyn,[7] seven trials of the GA were run for 20 generations, each with, on average, 20 structures in the population. Recall that each trial of the GA is independent, as the initial population of each trial is randomly generated from the start. Every single trial recovered the lowest-energy structure within the first five generations. Also, the top six structures recovered from the GAs are the same top six structures from the systematic search on 3.2% SDC. The fact that the systematic search results parallel the GA results imply that the evolutionary protocols in the GA are sufficient for exhaustively exploring the potential energy surface of 3.2% SDC materials. Structural qualities of the top six structures from the GA, named **C1**-**C6** according to their relative classical energies, are shown in Table 3–2.

Table 3–2. Relative energies and structural information of 3.2% SDC structures recovered from GA search

Structure	$E_{classical}$ [a,b] *(eV/cell)*	E_{DFT} [a,c] *(eV/cell)*	*Sm-Sm distance[d] (Å)*	*Sm-vacancy distance[e] (Å)*
C1	0.000	0.000	6.7	NN-NNN
C2	0.042	0.007	3.8	NN-NN
C3	0.098	0.023	6.7	NNN-NNN
C4	0.103	0.028	7.6	NNN-NNN
C5	0.158	0.107	3.8	NNN-NNN
C6	0.216	0.042	3.8	NN-NNN

[a] Energies reported are relative to the lowest energy structure of the given potential. [b] Relative total electronic energies from the classical potential of Balducci *et al.*[6] and Senyshyn *et al.*[7] [c] Relative total electronic energies from DFT calculations. [d] Sm-Sm distance reported is taken from the ideal lattice before geometry relaxation. [e] NN distance is approximately 2.4 Å, NNN ~ 4.5 Å, and NNNN ~ 5.9 Å.

The best six structures from these trials were then optimized with DFT. In the following order, structures **C1**, **C2**, **C3**, **C4**, and **C6** emerged as the best five structures ranked by DFT energetics. Encouragingly, the systematic search at the DFT level found these configurations to be the top five as well. This result was expected, due to the positive correlation between the classical potentials and the DFT optimization, presented earlier. This result indicates that the GA trials performed at the classical level were sufficient to screen out high energy structures from the gene pool.

Using Wei *et al.*[4]'s potentials for the same material, we performed additional GA trials on 3.2% SDC. Again, the GA results paralleled the systematic search results, which are summarized in Table 3–3. The last column in Table 3–3 refers to the structural notation used in ref. 4, so the reader can easily compare the results with those of Wei *et al.*

Table 3–3. Relative energies and structural information of 3.2% SDC structures recovered from GA search using parameters from ref. 4

Structure	$E_{classical}$ [a,b] *(eV/cell)*	*Sm-Sm distance*[c] *(Å)*	*Sm-vacancy distance*[d] *(Å)*	*Structure symbol*[e]
C4	0.000	7.6	NNN-NNN	4_2_2
C3	0.001	6.7	NNN-NNN	3_2_2
C5*	0.016	3.8	NNN-NNN	1_2_2
C1	0.030	6.7	NN-NNN	3_1_2
C5*	0.090	3.8	NNN-NNN	1_2_2
C5*	0.091	3.8	NNN-NNN	1_2_2
C2	0.125	4.1	NN-NN	1_1_1
C6	0.138	3.8	NN-NNN	1_1_2

[a] Energies reported are relative to the lowest energy structure of the given potential. [b] Relative total electronic energies from the classical potential of Wei *et al.*[4] [c] Sm-Sm distance reported is taken from the ideal lattice before geometry relaxation. [d] NN distance is approximately 2.4 Å, NNN ~ 4.5 Å, and NNNN ~ 5.9 Å. [e] Refers to the naming convention in ref. 4. *See text for details.

The explanation for multiple energies for seemingly identical **C5** configurations (denoted by * in Table 3–3) was provided earlier in Section 3.1. Recall that in our systematic search run with Wei *et al.*'s potentials, we obtained these three different energies for **C5**, whereas in ref. 4, Wei *et al.* treats them as different structures, and finds a different energy for one of the configurations. This does not represent a fault in the GA, because the GA mimicked the results from our systematic search (using the same potentials) perfectly. Rather, it is due to the difference in optimizations between that used in this work and that in ref. 4.

Overall, our GA results match qualitatively from those of the systematic search, correctly recovering and ranking each of the structures in the correct energetic sequence. To further demonstrate the effectiveness of the algorithm with other materials, we performed GA trials using potentials for which a systematic search has already been completed.[4] Past calculations have predicted that a crossover of NNN to NN preference

occurs in the lanthanide series around Gd,[3, 4] so we chose to study 3.2% GDC and LuDC to complement the 3.2% SDC results discussed above. For these materials, we make use of Wei *et al.*'s Buckingham parameters.

We ran two GA trials on each material, with 15 structures in the population. They ran for, on average, 15 generations, where the fittest structure remained unchanged in the last five generations. The lowest-energy structures from our GA trials of GDC are shown in Table 3–4, and similarly for LuDC in Table 3–5. The last column in these Tables refers to the naming convention used by Wei *et al.*,[4] to ease comparison with ref. 4. In addition, we ran a systematic search of GDC and LuDC using the same parameters as in the GA.

Table 3–4. Relative energies and structural information of 3.2% GDC structures recovered from GA search using parameters from ref. 4

Structure	$E_{classical}$ [a,b] *(eV/cell)*	*Gd-Gd distance*[c] *(Å)*	*Gd-vacancy distance*[d] *(Å)*	*Structure symbol*[e]
G1	0.000	6.7	NN-NNN	3_1_2
G2	0.020	4.1	NN-NN	1_1_1
G3	0.029	6.7	NNN-NNN	3_2_2
G4	0.029	7.6	NNN-NNN	4_2_2
G5	0.048	3.8	NNN-NNN	1_2_2
G6	0.097	3.8	NN-NNN	1_1_2

[a] Energies reported are relative to the lowest energy structure of the given potential. [b] Relative total electronic energies from the classical potential of Wei *et al.*[4] [c] Gd-Gd distance reported is taken from the ideal lattice before geometry relaxation. [d] NN distance is approximately 2.4 Å, NNN ~ 4.5 Å, and NNNN ~ 5.9 Å. [e] Refers to the naming convention in ref. 4.

Table 3–5. Relative energies and structural information of 3.2% LuDC structures recovered from GA search using parameters from ref. 4

Structure	$E_{classical}$ [a,b] *(eV/cell)*	*Lu-Lu distance*[c] *(Å)*	*Lu-vacancy distance*[d] *(Å)*	*Structure symbol*[e]
L1	0.000	4.1	NN-NN	1_1_1
L2	0.229	5.3	NN-NNN	2_1_2
L3	0.234	6.6	NN-NNN	3_1_2
L4	0.241	9.1	NN-NNNNN	5_1_4
L5	0.242	6.6	NN-NNNN	3_1_3
L6	0.267	7.6	NN-NNNN	4_1_3
L7	0.270	6.4	NN-NNNNN	3_1_4
L8	0.309	3.8	NN-NNN	1_1_2

[a] Energies reported are relative to the lowest energy structure of the given potential. [b] Relative total electronic energies from the classical potential of Wei *et al.*[4] [c] Lu-Lu distance reported is taken from the ideal lattice before geometry relaxation. [d] NN distance is approximately 2.4 Å, NNN ~ 4.5 Å, NNNN ~ 5.9 Å, and NNNNN ~ 7.0 Å. [e] Refers to the naming convention in ref. 4.

Overall, the potentials of Wei *et al.*[4] find that the NN-NN structure is favoured strongly (by 0.229 eV/cell) in LuDC, not favoured (nearly degenerate with other structures) in GDC, and disfavoured (by 0.125 eV/cell) in SDC. All of the structures shown in Table 3–4 and Table 3–5 were recovered in the same energetic order from the systematic searches. Therefore, it is clear that the GA can properly sample the structure space at this concentration. Yet, admittedly, this test is not a rigorous one. Since there are only 33 unique configurations in 3.2% LDC, it should be fairly easy for a GA or any search method to find all of these by simple trial and error, even with a small population size. To the credit of our GA, the mating and mutation routines, which were designed to use favorable structural information from the previous generation to create more fit structures, were the primary source of the low-energy configurations found in the GAs.

Section 3.2 - GA Search of 6.6% SDC

Studying the structure of doped ceria materials at concentrations above 3.2% is difficult due to the enormous number of possible configurations, created by the increased number of defects. A systematic evaluation of the PES of 6.6% SDC is unfeasible, at the DFT(+U) and classical levels of theory, so we have employed a specialized tandem genetic algorithm to find the lowest-energy structures. The details of our approach are described in Section 2.

Our genetic algorithm has proven to be effective at navigating the potential energy surface of 3.2% doped ceria materials, with a number of different potentials, correctly reproducing results of a systematic search. The algorithm's success suggests that it can be used to replace systematic searches at higher concentrations as well. Due to the enormity of the PES at 6.6% and higher concentrations, the GA trials run on these materials must have much larger population sizes and require many more generations to reach convergence than the GA trials at 3.2%. In this regard, a GA on 6.6% SDC with a DFT or DFT+U energy as the fitness is simply not feasible. Thus, we must first narrow the scope of the accurate DFT(+U) structure search, by using classical GA searches to eliminate the high-energy configurations. This is the main premise behind the tandem GA. We begin with classical simulations using potentials from Balducci *et al.*[6] and Senyshyn *et al.*[7], which were shown in the previous section to correlate well with DFT and DFT+U calculations.

Five GA trials, which used the energy derived from the classical potential as the fitness metric, were run on 80 to 120 structures each for 40 generations. The same best structure was recovered in every trial, which suggests that it is truly the lowest-energy

structure. Two larger trials, which were run for 100 generations with 200 structures in each population, did not produce any lower energy structures. Because the larger GA trials found no new configurations, we believe the sampling of the configuration space at the classical level was sufficient.

For the second step in the tandem search, we did two separate searches: one with DFT-based fitness and the other with DFT+U-based fitness. At first, the DFT energetics were used to benchmark the tandem method. Later, we were interested in accurately assessing the structural qualities of low-energy SDC structures, and so a DFT+U-based GA was necessary. The results of both searches are presented below and the implications of using the more accurate method are discussed.

Prior to the DFT and DFT+U GAs, certain classical/classical tandem GAs were done by James Hooper in order to prove the robustness of the algorithm. For example, one tandem GA was performed using a poor screening potential in the first step of the tandem GA and demonstrating the ability of the second step of the GA to still find the low-energy structures. Another test determined the right population size to use in the second step of the tandem GA. Because the second step is much more computationally demanding, the second GA should recover the lowest-energy structures using the smallest population possible. It was determined that a total population of 50 structures, starting from the best 16 structures from the first step, can converge within 25 generations. All of these tests were done by James Hooper and are described in ref. 11.

The top 16 structures from the classical GA trials, along with 34 randomly generated structures were used as the initial population of a GA which used the energy from DFT+U calculations as the fitness metric. This DFT+U GA trial, which had a

population size of 50 structures, was run for 20 generations requiring over a thousand geometry optimization runs. Over the final ten generations, the top five members of the population remained the same. This was deemed sufficiently converged based on benchmark calculations of our tandem GA in a previous study.[11] The DFT GA trial started from the same 16 structures found by classical GAs, and 34 randomly generated ones. This GA was run for 25 generations, and found no structures to displace the three lowest-energy structures carried over from the classical portion.

The lowest-energy configurations recovered from the DFT+U GA, which we have labeled **U1** to **U5**, are shown in Table 3–6. The reported energies are relative to the lowest-energy structure obtained from the respective method - i.e. the best structure is assigned an energy of zero. Qualitative information such as the distance between vacancies and distance between Sm atoms and vacancies is also provided. As there are two vacancies in the simulation cell, we report the distances of all four Sm atoms to each vacancy in two columns: Sm-vac1 and Sm-vac2. Interestingly, two of the lowest five structures, **U2** and **U4**, were not read in to the initial population of the DFT+U GA, yet were found through mating and mutation operations. If these configurations proved to be grossly high in energy in the classical optimization, then they would represent false negatives and greatly compromise the validity of the screening using this method. However, we find that in the classical GA, structures **U2** and **U4** are not that far off from **U3** and **U5** in terms of energy (at the classical level). Indeed, had we read in slightly more than the top 16 structures from our classical GAs, structures **U2** and **U4** would have been members of the population from the beginning of the DFT+U GA. For reference, the lowest energy structure resulting from the classical GAs, structure **X1**, is also

included in Table 3–6. Structure **X1**, although the best structure with the classical potential, is somewhat high in energy at the DFT+U (and DFT) level. It is also useful to compare the lowest energy structures of 6.6% SDC obtained from the DFT+U GA with those determined at the DFT level. The lowest-energy configurations recovered from the DFT GA, which we have labeled **D1** to **D5**, are given in Table 3–7.

Table 3–6. Relative energies and structural information of the best five 6.6% SDC structures recovered from DFT+U GA

Structure[a]	ΔE_{DFT+U} *(eV/cell)*[b,c]	ΔE_{DFT} *(eV/cell)*[b,d]	$\Delta E_{classical}$ *(eV/cell)*[b,e]	*Vac-vac distance*[f] *(Å)*	*Sm-vac1 distance*[g]	*Sm-vac2 distance*[g]
U1/D1[h]	0.000	0.000	0.048	6.0	3 NNN, 1 NN	3 NNN, 1 NN
U2*	0.000	0.297	0.369	6.0	1 NNNN, 1 NNN, 2 NN	1 NNNN, 1 NNN, 2 NN
U3	0.027	0.089	0.330	6.0	1 NNNN, 1 NNN, 2 NN	3 NNN, 1 NN
U4*	0.039	0.118	0.386	6.0	2 NNN, 2 NN	1 NNNN, 2 NNN, 1 NN
U5	0.043	0.286	0.337	6.0	3 NNN, 1 NN	2 NNN, 2 NN
X1[i]	0.128	0.198	0.000	6.7	4 NNN	4 NNN

[a] Structures with asterisks were newly found with the DFT+U GA and were not a member of the initial population. [b] Energy relative to the lowest-energy structure, which is assigned a value of zero. [c] Relative total electronic energies from DFT+U calculations. [d] Relative total electronic energies from DFT calculations. [e] Relative total energies from the classical potential of Balducci[6] and Senyshyn.[7] [f] The vacancy-vacancy distance reported is taken from the ideal lattice before geometry relaxation. [g] The column shows the number of Sm with that particular distance followed by a letter code for the distance value (NN is on average 2.4 Å, NNN is 4.5 Å, and NNNN is 5.9 Å). [h] Structure **U1** is identical to structure **D1** located from the DFT GA reported in Table 3–7. [i] The lowest energy structure, **X1**, resulting from the classical GA is provided for reference.

Table 3–7. Relative energies and structural information of select 6.6% SDC structures from DFT GA

Structure	ΔE_{DFT} *(eV/cell)* [a,b]	ΔE_{DFT+U} *(eV/cell)* [a,c]	*Vac-vac distance (Å)* [d]	*Sm-vac1 distance* [e]	*Sm-vac2 distance* [e]
D1/U1 [f]	0.000	0.000	6.0	3 NNN, 1 NN	3 NNN, 1 NN
D2	0.020	0.110	6.0	4 NNN	4 NNN
D3	0.020	0.082	6.0	4 NNN	3 NNN, 1 NN
D4	0.030	0.082	6.0	4 NNN	3 NNN, 1 NN
D5	0.041	0.069	6.0	4 NNN	2 NNN, 2 NN

[a] Energy relative to the lowest-energy structure, which is assigned a value of zero. [b] Relative total electronic energies from DFT calculations. [c] Relative total electronic energies from DFT+U calculations. [d] The vacancy-vacancy distance is taken from the ideal ceria lattice before geometry optimization. [e] The column shows the number of Sm with that particular distance followed by a letter code for the distance value (NN is on average 2.4 Å, and NNN is 4.5 Å). [f] Structure **D1** is identical to structure **U1** located from the DFT+U GA reported in Table 3–6.

The small differences in energy between favoured configurations in Table 3–6 suggest that several of these may co-exist in low-to-intermediate temperature solid oxide fuel cells (IT-SOFC). Therefore, in order to gain structural insight on the material, we attempt to rationalize structural trends from a number of low-energy configurations recovered from the GA. The first, most striking feature is that structures with a 6 Å vacancy separation are strongly favored. This is a ubiquitous characteristic of all structures recovered from both DFT and DFT+U GAs. Structures with longer or shorter vacancy-vacancy distances tend to have higher energies at the DFT and DFT+U levels of theory. For example, structure **X1**, which has a vacancy-vacancy distance of 6.7 Å is notably higher in energy (0.128 eV in DFT and 0.198 eV in DFT+U). Therefore, such configurations would not contribute significantly to the overall makeup of the material at IT-SOFC operating temperatures if one were to assume a Boltzmann distribution of configurations.

Interestingly, beyond the identical vacancy separation, there is little overlap between the five lowest energy structures obtained at the DFT+U and DFT level. Only structure **U1** was recovered from both GAs, and amongst the other structures - namely **U2** to **U5** and **D2** to **D5** - there exist significant differences. The most striking is that the next-nearest-neighbor (NNN) preference of the Sm atom relative to the vacancy is observed with DFT but not with DFT+U. Structures **D2** to **D5** all contain at least one vacancy with exclusive NNN Sm occupation. These structures are disfavoured in DFT+U (relative energies $\geq$ 0.07 eV compared to U1) because of their NNN dominance, yet are favoured in conventional DFT calculations for this same characteristic.

In contrast, DFT+U-favoured structures contain a variety of Sm-vacancy interactions, with no specific site being dominant. A commonality amongst structures **U1** to **U5** is the presence of at least one samarium atom nearest neighbor to each vacancy. This is not seen in the majority of DFT-favoured structures, **D2** to **D5**. It is precisely for this lack of Sm NN interactions at both vacancies that these structures are penalized in DFT+U. A more precise analysis further justifies this conjecture. Consider structures **D2** to **D5** at the DFT+U level. These structures possess the same optimal vacancy-vacancy distance and somewhat similar Sm-Sm distances. **D2** is highest in energy out of this set because no NN sites are occupied by a Sm atom; **D3** and **D4** are slightly lower in energy than **D2**, due to the presence of one NN interaction; and **D5** is even lower in energy at 0.07 eV/cell due to the presence of an additional NN interaction. Considering the structural differences amongst **U2** to **U5** and **D2** to **D5**, we can conclude that DFT+U does not favor the NNN Sm-vacancy interaction nearly as strongly as does conventional DFT, and that the DFT+U method favors a balance of Sm-vacancy interactions.

We now focus our analysis on the two lowest-energy structures, **U1** and **U2**, which are most likely to be present in low temperature 6.6% SDC. As their relative energies suggest, structures **U1** and **U2** are very similar configurations (see Figure 3–7). The Sm positions in both structures are identical; only the vacancies have moved one lattice unit (or 2.7 Å) in the x direction. In a real fuel cell, even at low temperatures, one does not expect a single configuration to exist on its own, as oxygen anions must hop over vacancies to move through the lattice and hence contribute to the overall conductance. Because anions move orders of magnitude faster than cations in the fluorite structure,[12] it is reasonable to assume that the vacancies will quickly change positions to create a range of configurations existing in a dynamic state, while the metal atoms remain in their ideal lattice sites. Indeed, studies modelling ionic conductance in doped ceria and zirconia electrolytes have found this to be true.[13-15] Therefore, we suggest that both structures **U1** and **U2** be considered in future modelling studies of 6.6% SDC.

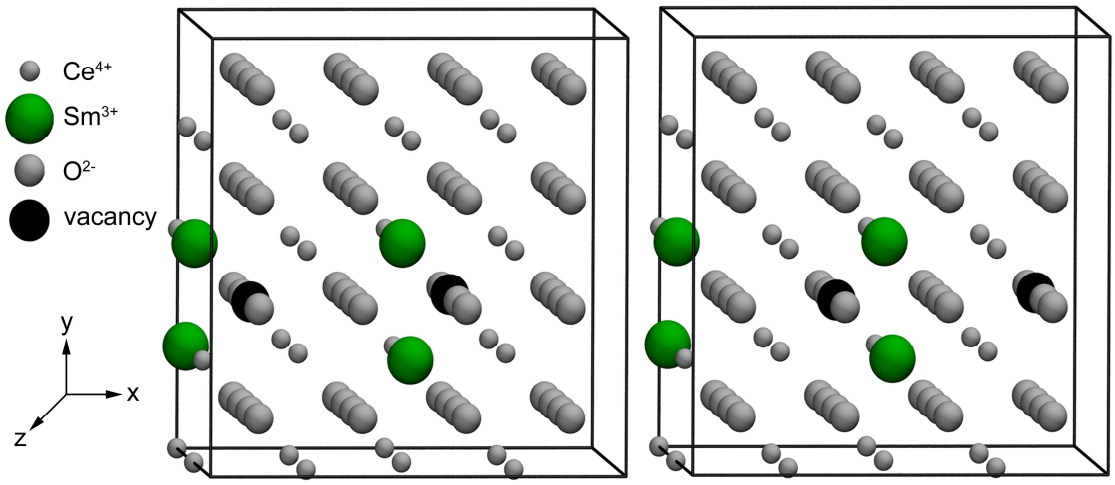

Figure 3–7. Atomic positions of the lowest energy structures, U1 (*left*) and U2 (*right*) obtained from the DFT+U GA structure search. For clarity, the unrelaxed positions are shown.

The fact that **U1** and **U2** are degenerate has another interesting implication. Consider the radically different Sm-vacancy interactions induced by the shift of both

vacancies by a single lattice position: from a structure with 6 NNN and 2 NN interactions, a structure with 2 NNNN, 2 NNN, and 4 NN interactions is created. The fact that both configurations have the same energy shows that 6.6% SDC favours "hybrid" structures which contain a variety of Sm-vacancy distances. This is important because the same rationale has been used to explain the high ionic conductivity of Gd-doped ceria (GDC) at 3.2%; namely, because the NN and NNN sites are degenerate for Gd^{3+}, it is favorable for a number of configurations to hop from one to another, and hence the material has high ionic conductivity.[4, 11] (As a side note, this so-called "degeneracy" is based on energy evaluations from classical potentials and subsequent DFT+U calculations[9] have shed doubt on this claim. However, the rationale for high ionic conductivity remains sound.) The opposite is true for Lu-doped ceria at 3.2% where the NN site is strongly favoured: here, the vacancies are trapped in a deep potential energy well and thus argued to be less mobile.[3, 4, 11] For 6.6% SDC, the hybrid configurations are degenerate, meaning the vacancies are not trapped in a particular site - much like in 3.2% GDC - which gives the material very high ionic conductivity. This relationship is explored further in Section 3.3.

It is worthwhile to note that the thermal energy available at 673 and 773 Kelvin, which are typical SOFC operating temperatures, is 0.058 eV and 0.066 eV, respectively. Therefore, it is not just **U1** and **U2** that will co-exist at these temperatures; the relative energies of structures **U1** to **U5** fall within this range, and should be substantially populated at these temperatures. In fact, our GA recovered five additional structures (**U6** to **U10** - shown in Table 3–8) that lie within kT at 773 K, three of which lie within kT at 673 K. These structures would also be expected to be prevalent in low temperature fuel

cells. Although our GA was not fully converged beyond the fifth-best structure, we find a 6 Å vacancy separation in the top ten structures from the GA, which reinforces the notion that this particular distance is favored. Also, as in the top five, the top ten configurations do not exclusively favor a particular Sm-vacancy interaction. Other GAs done by James Hooper on vast structure spaces in a 3x3x3 simulation cell demonstrate that the GA does not need to be fully converged to the best structures in order to rationalize meaningful trends from the data.[11]

Table 3–8. Relative energies and structural information of select 6.6% SDC structures recovered from DFT+U GA

Structure[a]	ΔE_{DFT+U} *(eV/cell)*[b,c]	*Vac-vac distance*[d] *(Å)*	*Sm-vac1 distance*[e]	*Sm-vac2 distance*[e]
U6*	0.046	6.0	1 NNNN, 3 NN	1 NNNN, 2 NNN, 1 NN
U7*	0.056	6.0	1 NNNN, 3 NN	2 NNNN, 1 NNN, 1 NN
U8*	0.058	6.0	1 NNNN, 2 NNN, 1 NN	1 NNNN, 1 NNN, 2 NN
U9*	0.062	6.0	3 NNN, 1 NN	1 NNNN, 1 NNN, 2 NN
U10	0.066	6.0	3 NNN, 1 NN	3 NNN, 1 NN

[a] Structures with asterisks were newly found with the DFT+U GA and were not a member of initial population. [b] Energy relative to the lowest-energy structure, which is assigned a value of zero. [c] Relative total electronic energies from DFT+U calculations. [d] The vacancy-vacancy distance reported is taken from the ideal lattice before geometry relaxation. [e] The column shows the number of Sm with that particular distance followed by a letter code for the distance value (NN is on average 2.4 Å, NNN is 4.5 Å, and NNNN is 5.9 Å).

Thus, in order to simulate a representative structure of 6.6% SDC, future studies should investigate configurations which contain the interactions that are favoured at the DFT+U level of theory. These structural qualities are as follows: a 6 Å distance between oxygen vacancies; at least one Sm ion nearest neighbor to each vacancy; and a mix of Sm-vacancy distances (i.e. no single coordination site around the vacancy (NN, NNN, or NNNN) is favoured).

In summary, the tandem GA has been used to find the low-energy configurations of SDC at the 6.6% concentration, which are important to understand the mechanism of fuel oxidation and bulk oxygen ion diffusion, as well as the change in properties with increasing dopant. A preliminary investigation of oxygen ion diffusion in 3.2 and 6.6% SDC is carried out in the next section. Following this, we will continue to use our GA to investigate higher concentrations, which are more representative of the optimal SDC fuel cell electrolyte.

Section 3.3 - oxygen Ion Diffusion in Bulk SDC

In this section, we investigate the activation energy barriers for oxygen ion diffusion in 3.2 and 6.6% SDC, making use of the low-energy structures found by the GA. Since it is only relevant to explore the oxygen ion migrations which are likely to occur in low-temperature fuel cells, then it makes sense that we evaluate those migrations between low-energy configurations. Prior works have investigated oxygen ion migrations in other 3.2% lanthanide-doped ceria materials, where it is feasible to evaluate all possible oxygen jumps, at the DFT+U level of theory.[9, 16] Andersson *et al.*[1] as well as Nakayama and Martin[3] performed a DFT study on selected diffusion pathways in 3.2% SDC. We build on this work by evaluating selected oxygen ion jumps in 3.2% SDC, for the first time at the DFT+U level of theory, and compare our results to lower level calculations. These results are presented in Section 3.3.1.

At 6.6%, just as with the structure search, evaluating all possible oxygen ion jumps is not possible due to the enormous number of possibilities. Now that the low-energy 6.6% SDC structures are known, it is possible to perform a diffusion study on this

material, and investigate relevant oxygen migration paths in the lattice amongst the most prevalent configurations. Thus, we consider structures **U1** and **U2** in our evaluation of diffusion in 6.6% SDC. These results are presented in Section 3.3.2.

Note that the work presented here is not a complete picture of the diffusion in 3.2 and 6.6% SDC; in the interest of time, we selected specific migrations to evaluate, and consider our work a starting point for future research on oxygen ion diffusion.

3.3.1 - Migration Barriers in 3.2% SDC

Because the anions in the fluorite structure move orders of magnitude faster than the cations,[12] it makes sense to consider oxygen ion migrations between structures which possess the same Sm positions. Previous studies modelling ionic conductance have also relied on this phenomenon.[13-15]

Two such configurations are **S2** and **S9**, which represent an oxygen ion migration between NN and NNN sites. We chose these configurations because the dopant ions are 6.6 Å apart, which is a large enough distance that they do not interact. This also makes our calculations analogous to the Pr- and Gd-doped ceria migration barrier calculations of Dholabhai *et al.*,[9, 16] who separated the dopant ions by approximately the same distance. We find that the activation energy for the NN to NNN transition was higher than that for the reverse transition, due to the fact that the NN site is favoured in 3.2% SDC. The migration barrier for the NN→NNN transition was 0.48 eV, and for the reverse it was 0.40 eV, which is on par with barriers for 3.2% GDC[9] (0.50 eV for the forward and 0.36 eV for the reverse). In contrast, work by Dholabhai *et al.* showed that in Pr-doped ceria (PDC) the NN→NNN transition is favoured over the NNN→NN by 0.02 eV.[16] Also in

contrast to GDC and SDC, it was found with DFT+U calculations that the Pr^{3+} dopant prefers to occupy the NNN position relative to the vacancy.[16]

The differences in migration barriers and dopant-vacancy preferences in PDC versus GDC and SDC is often understood by the size of the dopant ion. Pr^{3+} is substantially larger than Gd^{3+} and Sm^{3+} and so it tends to repel vacancy formation at the nearest neighbor site.[1, 16] Several theoretical[1, 3, 4, 11] and experimental[17] works have confirmed that smaller dopants such as Y^{3+} and Lu^{3+} strongly favour the NN site, and in fact trap the oxygen vacancy in a deep potential energy well in their low-energy configurations, although this is yet to be confirmed with DFT+U calculations. As SDC and GDC fall in the middle of the lanthanide series, they represent a balance between these competing effects: the dopant is large enough so as not to trap vacancies in NN sites yet small enough to have easily surmountable migration barriers. Consequently, SDC and GDC have the highest ionic conductivity amongst all singly-doped ceria materials.

With conventional DFT, Nakayama *et al.* found a linear correlation between dopant ionic radius and activation energy for oxygen vacancy diffusion.[3] Our DFT+U calculations are in line with this trend as SDC and GDC have near-identical dopant ionic radii and exhibit similar migration barriers. However, it is possible that the DFT+U method may give significantly different activation barriers than DFT. To test this, we further consider the migration barrier for the NNN→NN transition considered by Andersson *et al.* for 3.2% SDC configurations in which the dopant ions lie 3.8 Å apart.[1] This corresponds to a transition from structure **S4** to **S1** and was found to have a barrier of 0.39 eV at the DFT level with structure **S1** being 0.08 eV more stable than **S4**. Although the energy difference between structures **S4** and **S1** is the same at the DFT+U

level, the activation barrier is found to be 0.56 eV (**S4** to **S1**), which is 0.16 eV higher than the analogous migrations where the dopant ions lie 6.6 Å apart. The discrepancy between DFT and DFT+U calculated migration barriers, suggests that the two methods may predict different migration pathways.

Unfortunately, it is not possible to compare the energies for single jumps to the experimentally-determined activation energy, because the rate-limiting migrations have not been found. Since the experimental value is an average of several long range oxygen ion migrations, the likelihood of all possible single jumps must first be determined in order to calculate the activation energies of plausible long range diffusion pathways, which can be compared to experiment. However, a systematic investigation of all possible migrations is beyond the scope of this work. Encouragingly, Andersson *et al.* reported the same additive effect on the barriers upon bringing the dopant ions closer to one another in the lattice for several doped ceria materials.[1] Once again, DFT+U reproduces a trend from a lower level calculation, yet the actual values are distinct.

3.3.2 - Migration Barriers in 6.6% SDC

We investigate activation energy barriers for different vacancy migration pathways in 6.6% SDC in order to gain insight on the mechanism of oxygen diffusion in this material. While several studies of migration barriers have been calculated for 3.2% SDC, the literature severely lacks the same investigations for higher concentrations. As mentioned previously, the higher concentrations are of greater relevance to fuel cell researchers because the peak of SDC's ionic conductivity is around 11%. To investigate relevant diffusion pathways, one must study the structures that are representative of the true material. To this end, we use the lowest-energy structures from our GA search to

investigate diffusion in 6.6% SDC, as they are the most prevalent in nature. In particular, structures **U1** and **U2** are ideal for this study, because their cation positions are identical (see Figure 3–7), which is crucial in order to study a realistic pathway involving only anionic migrations. In this section, we consider two possible pathways of diffusion between structures **U1** and **U2**: the concerted and step-wise mechanisms (see Figure 3–8).

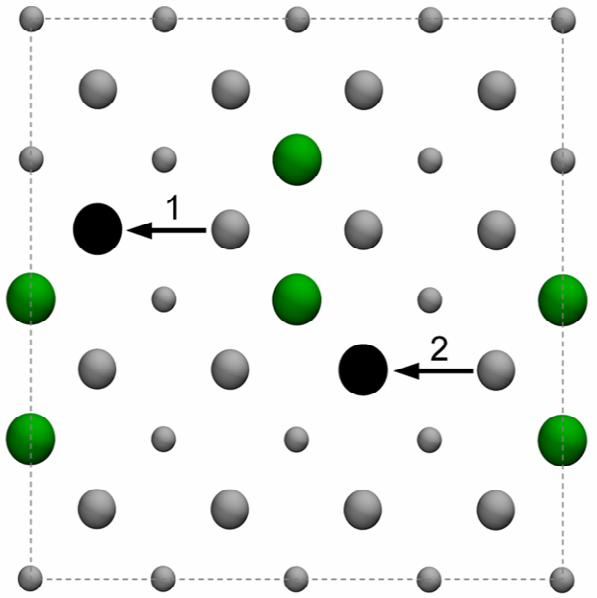

Figure 3–8. Top view of vacancy-containing (010) plane of structure U1. In the stepwise pathway, migrations illustrated by the arrows 1 and 2 occur sequentially. In the concerted mechanism, migrations 1 and 2 occur simultaneously. The colour scheme is the same as in Figure 3–7.

We begin with the step-wise approach, which is more analogous to the previous studies at 3.2%, because it considers the migration of only a single oxygen ion. In this mechanism, one of the vacancies from structure **U1** moves to its position in **U2**, creating an intermediate structure with a 3.8 Å vacancy separation; subsequently, the second vacancy migrates to become the **U2** structure. It was expected that this intermediate would be very high-energy due to the unfavourable positioning of the oxygen vacancies. The relative DFT+U energy of the intermediate was 0.24 eV, which is in line with our understanding of the effect of vacancy separation on the energy. As there are two

vacancies in the lattice, it is possible to create two intermediates depending on which vacancy is moved first; both possibilities were examined, namely wherein either migration 1 or migration 2 (as illustrated in Figure 3–8) occurs first. It was found that both intermediates had the same energy and that their corresponding transition states were also degenerate, which indicates that it does not matter in what order the migrations occur. The activation energy for the stepwise mechanism was found to be 0.43 eV, which is comparable to activation energies found for 3.2% GDC[9] (for example, 0.46 eV) and SDC (for example, 0.40 eV) at the same level of theory. Interestingly, in this case the presence of additional Sm ions and vacancies in the 6.6% SDC lattice does not significantly change the migration barriers for oxygen diffusion as compared to 3.2% SDC.

In the concerted mechanism, both oxygen vacancies migrate together to create a transition state that preserves the 6 Å vacancy separation. This corresponds to both migrations 1 and 2 illustrated by the arrows in Figure 3–8. It was found that the activation energy for the concerted migration was 0.73 eV, almost twice as high as that for the stepwise mechanism. This is most likely due to the fact that in the concerted transition state, two oxygen ions lie in unfavourable positions, which destroys many of the favourable interactions present in configurations **U1** and **U2**. In contrast, in the stepwise mechanism only one oxygen ion lies in a non-equilibrium position, which preserves the favourable interactions for one of the vacancies (that which is not moving) in the structure. Thus, it seems that the additional Sm-vacancy and vacancy-vacancy interactions present at higher concentrations cause the stepwise mechanism to be favoured over its concerted counterpart.

We note that the midpoint approximation was used in estimating the migration barriers wherein the migrating ion is placed halfway between the initial and final states. For the stepwise mechanism, this is a good approximation as calculations where the ion is shifted slightly from the midpoint reveal that the midpoint is the highest energy position. However, for the concerted mechanism, one could imagine that the migration of one ion occurs slightly before the other. To address this concern for the concerted mechanism, we investigated six alternative intermediate configurations where one migration occurred slightly before the other. In other words, one ion was constrained to the midpoint, while the other ion was placed slightly before or after the midpoint structure. All of these were found to be lower in energy than the structure where both ions were placed at the midpoint.

An important corollary to the 0.43 eV activation energy of the stepwise mechanism is that the energy of the intermediate structure, at 0.24 eV above the starting configuration, comprises more than half of the barrier. This illustrates a large influence of relative association energies on the activation energies for diffusion. This was also shown in Section 3.3.1 for 3.2% SDC, as the kinetic preference for lower activation energies was governed by the thermodynamic preference for structures with lower energy; recall that **S2** was favoured by 0.11 eV over **S9**, and hence the barrier for migration was 0.40 eV for **S9→S2** but proportionately higher for the reverse. The fact that at 6.6% the relative energies comprise even more of the barrier suggests that, as the concentration of dopant increases, the dopant-vacancy associations become more important in controlling oxygen migration. Therefore, future investigations of 6.6% SDC should be concerned with

investigating diffusion amongst the low-energy structures which were found by our DFT+U GA.

To summarize, we have shown that the migration barriers in 6.6% SDC are comparable to those in 3.2% GDC, which could explain the high ionic conductivity in these materials. Also, in 6.6% SDC the vacancies prefer to move in a step-wise manner rather than in a concerted mechanism. Further work is needed to fully understand the migration pathways in 6.6% SDC, and we have provided the basis for such work with the configurations found by the GA. Overall, DFT+U calculations reproduce trends found with lower level methods, but the actual values are different. In studying diffusion, it is often important to know the activation energy of a particular migration; in these cases we must trust the DFT+U-calculated barriers, because it is the most accurate method.

Section 3.4 - GA Search of 10.3% SDC

Perhaps the most relevant concentration to study in a 2x2x2 simulation cell of SDC is 10.3%, as it is closest to the optimal value of 11% that is used in real fuel cells. 10.3% SDC consists of three vacancies and six Sm atoms distributed in the 96-atom cell. The number of possible configurations at this concentration is therefore 193 trillion, which is orders of magnitude greater than the number for 6.6%. Clearly, the classical GA trials will need to be of much greater size and greater in number, to ensure the lowest-energy structures are recovered.

As mentioned in Section 2, there were a number of GA trials run on this material without the proper structure screening. Thirty GA trials, each with 500 structures, were run for 300 generations, using the classical potentials of Balducci *et al.*[6] and Senyshyn *et*

al.[7] Every single trial converged to the same top six or seven structures. Subsequently, seven more GA trials were run, with the same population size and for the same amount of time, yet they began from the best seven structures found previously (along with 493 random structures). These trials found no better structures to displace the top seven, after 300 generations. Later, it was noted that some of these structures were in fact identical, and that structure screening was not adequate. Overall, the best configurations had predominantly NNN Sm-vacancy interactions, and a 6 or 6.6 Å separation between all vacancies. Even though there were duplicate structures in the genepool, from these trials we still had a good sense of what to expect in the lowest-energy configurations of 10.3% SDC.

With the correct screening of duplicate structures, eight trials of the GA were run, again with 500 structures and for 300 generations. Here, the original top seven were narrowed down to just two unique structures. Still, they were the same configurations that were found previously as the lowest-energy candidates. All of the trials found the same lowest-energy structure within the first 50 generations. Encouragingly, in all eight trials, the same top seven unique configurations were found. In seven out of eight trials, the same top ten unique configurations were found. These structures all exhibited a preference of NNN Sm-vacancy distances, and a 6 Angstrom separation between vacancies. Based on these findings, it is highly doubtful that a more fit structure was not investigated. To ensure the search was sufficient, two larger GA trials were run on populations of 1000 structures for 500 generations. Encouragingly, the larger GA trials found no new low-energy configurations that were not seen with the smaller GA trials.

Once the search at the classical level was complete, it was time to begin the DFT+U GA. However, we first needed to run tandem GA tests to determine the smallest population size that could be used and the number of generations required to reach convergence in the second GA. To this end, we ran tandem classical-classical GAs, which used the potentials of Wei *et al.*[4] in the first step, and the more accurate SDC potentials of Balducci[6] and Senyshyn[7] in the final step. The goal was to reproduce the low-energy structures of the chosen potential in the second step with the smallest population size possible, in the least number of generations.

First, a large structure search was completed with Wei *et al.*'s SDC potentials. Five GA trials were run each with 500 structures for 300 generations; convergence was achieved quickly as with the other classical potentials. For the second part of the tandem GA, several trials with various options in the GA were tested. Because the regular version of the GA did not find the structures fast enough, certain mating and mutation operations were turned off in an attempt to improve the convergence speed. We noted the number of trials which recovered the best six and best seven structures, as ranked by the Balducci[6] and Senyshyn[7] force field, as well as how many generations they took to reach this point. Five trials of each type of GA were run, to minimize the effect of randomness in the results. All of the tandem GA test parameters and results are summarized in Table 3–9.

Table 3–9. Tandem classical-classical GA parameters and results for 10.3% SDC

Special option[a]	# read in from step 1[b]	Total population size	# of trials which found:[c] best 6	best 7	# of generations required to find best 7
None	17	50	4/5	1/5	> 100
None	17	100	5/5	4/5	≥ 150
None	24	50	2/5	0/5	N/A
None	24	100	3/5	3/5	≥ 70
15 elite structures[d]	24	50	0/5	0/5	N/A
Perturb Off[e]	24	50	1/5	1/5	> 200
Perturb Off[e]	0	50	0/5	0/5	N/A
Perturb Off[e]; Mating Off[f]	24	50	4/5	3/5	≥ 116
Perturb Off[e]; Mating Off[f]; Swap Both Off[g]	24	50	5/5	4/5	≥ 125
Perturb Off[e]; Mating Off[f]; Swap Dopants Off[h]	24	50	0/5	0/5	N/A
Perturb Off[e]; Mating Off[f]; Swap Vacs Off[i]	24	50	5/5	5/5	≥ 43; ≤ 175; avg. 107

[a] All trials are step two tandem GAs and were run for 300 generations using the potentials from Balducci *et al.*[6] and Senyshyn *et al.*[7] [b] Number of structures, from the classical GAs with Wei *et al.*[4]'s potentials, that were read into the initial population. [c] These columns show how many trials found the top six and top seven structures. [d] This GA promoted 15 structures instead of the default 5. [e] This GA did not use the geometry perturbation. [f] This GA did not use the crossover (mating) routine. [g] This GA did not use the mutation which alters the positions of both dopant atoms and vacancies. [h] This GA did not use the mutation which alters the positions of dopant atoms. [i] This GA did not use the mutation which alters the positions of vacancies.

It is crucial that at least the best seven configurations are found within a reasonable time, since DFT+U GAs are very computer demanding. For example, twenty generations of a DFT+U GA on 6.6% SDC took approximately 2 months to complete, running on one to two hundred processors. The results from Table 3–9 suggest that we would have to wait approximately 100 generations to achieve convergence, which is not feasible at the DFT+U level.

However, from these results we can still gain insight on the performance of the GA routines. It was first noted that the geometry perturbation was not finding lower-

energy structures, so this mutation was turned off. It seems like the mating operation performs poorly in later stages of the GA, as better results are obtained when mating is turned off in part two of the tandem algorithm. However, at the start of large structure searches, the mating routine plays a much more important role. Finally, the best performance was achieved by turning off the mutation which swaps vacancies. This is most likely because, in the late stages of a GA, the structures already have the optimal vacancy-vacancy separation, so altering this only increases the energy and lowers the fitness. Oddly, the GA performs worse when 24 structures from step one are read in as opposed to 17. This may be due to the fact that the additional seven structures read in are in fact not favourable in energy with the classical potentials used in step 2 of the GA.

Overall, convergence is too slow for a DFT+U GA to be feasible at this concentration. More importantly though, perhaps a DFT+U GA is not needed at this concentration. The defect distribution amongst the top 40 configurations found at the classical level is nearly identical. The structural qualities which are favoured at the classical level include the NNN preference of the dopant, and the 6 or 6.6 Å separation of the vacancies. The same distribution is most likely favoured at the DFT+U level as well. In fact, it would suffice to show that the distribution amongst the best structures in the DFT+U GA has converged, rather than prove that the lowest-energy configurations have not changed in several generations. Also, it is much quicker for the defect distribution amongst favoured structures to converge compared to the structures themselves.[11] The only drawback of this approach is that perhaps not all of the low-energy configurations are recovered, and the precise number of configurations which lie within kT at fuel cell temperatures remains unknown. However, we hypothesize that at 10.3% SDC there exist

so many configurations which are populated at IT-SOFC temperatures, with similar defect distributions, that accurate energies of every single one are not needed.

In light of this, it seems that a DFT+U GA which begins from a number of different defect distributions should converge to a single distribution amongst the best structures. However, we cannot begin such a GA from the favoured structures found at the classical level, as they all have the same distribution. Furthermore, it is unknown how many configurations are necessary to properly sample all possible distributions. Indeed, such a GA might still be too cumbersome to perform due to limited computational resources. It would be more feasible to show that DFT+U correlates with the Balducci[6] and Senyshyn[7] force field at this concentration, by comparing the relative energies of configurations with different defect distributions, selected manually.

To prove this, we evaluated the top 28 unique configurations recovered from the classical GA trials with DFT+U, all of which had the same structural characteristics described above. Also, 25 configurations which had most Sm NNN to the vacancies, a trait in common with the true low-energy structures, but a variety of vacancy-vacancy distances, in contrast with the optimal separation found amongst the low-energy structures, were evaluated in DFT+U. As well, selected configurations with different dopant and vacancy distributions were run in DFT+U and with the classical potentials. In addition, we used a special version of the GA which reversed the fitness to favour high-energy structures, at the classical level. Two such GA trials with 500 structures were run for 100 generations, and the three optimal structures from these trials were optimized in DFT+U. If the correlation holds, then these structures should be highest-energy in DFT+U, probably with a large energy separation relative to the structures recovered from

the normal, low-energy-fitness classical GAs. Also, if the correlation holds, then the structures with different defect distributions should have higher energies in DFT+U compared to those with the favoured defect distribution; in other words, the distribution favoured classically should also be favoured at the DFT+U level.

The energies of structures with similar dopant-vacancy distances yet different vacancy-vacancy distances help understand how the vacancy separation affects the stability of a configuration. The energies for these 25 configurations as a function of vacancy separation are plotted in Figure 3–9 and Figure 3–10. There is overwhelming agreement between the classical force field and DFT+U with regards to vacancy separation; the favoured structures all have vacancies separated by at least 6 Angstroms, and no more than 6.6 Angstroms.

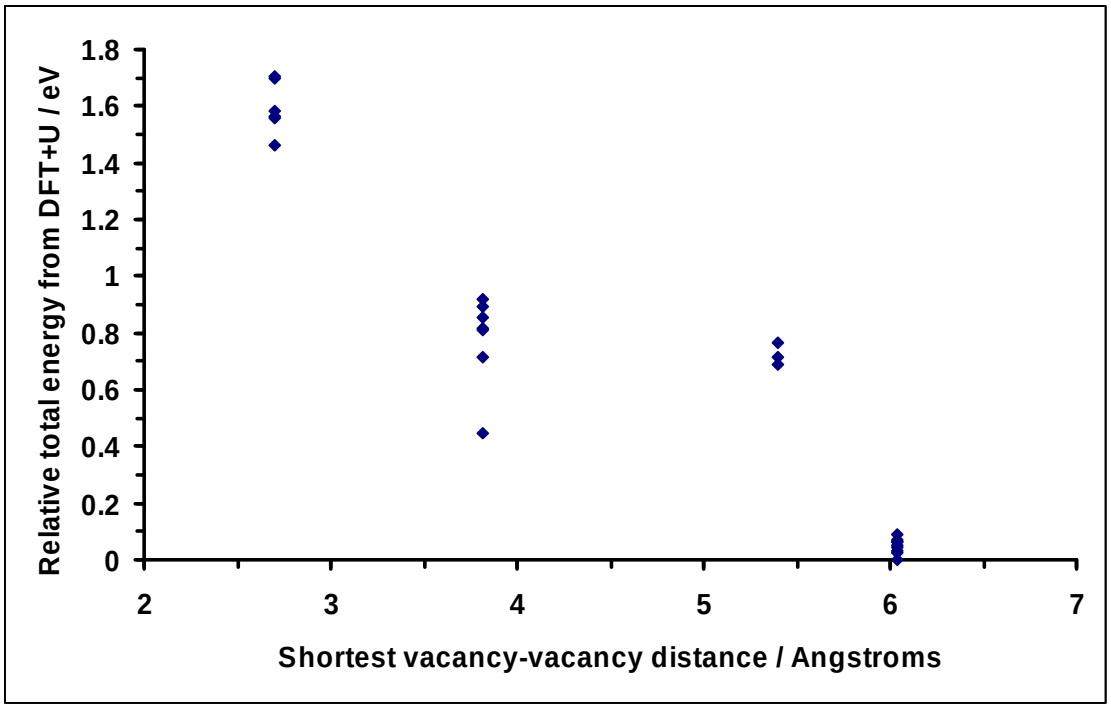

Figure 3–9. DFT+U energy of various 10.3% SDC configurations as a function of shortest vacancy-vacancy distance. These structures have similar Sm-vacancy distances.

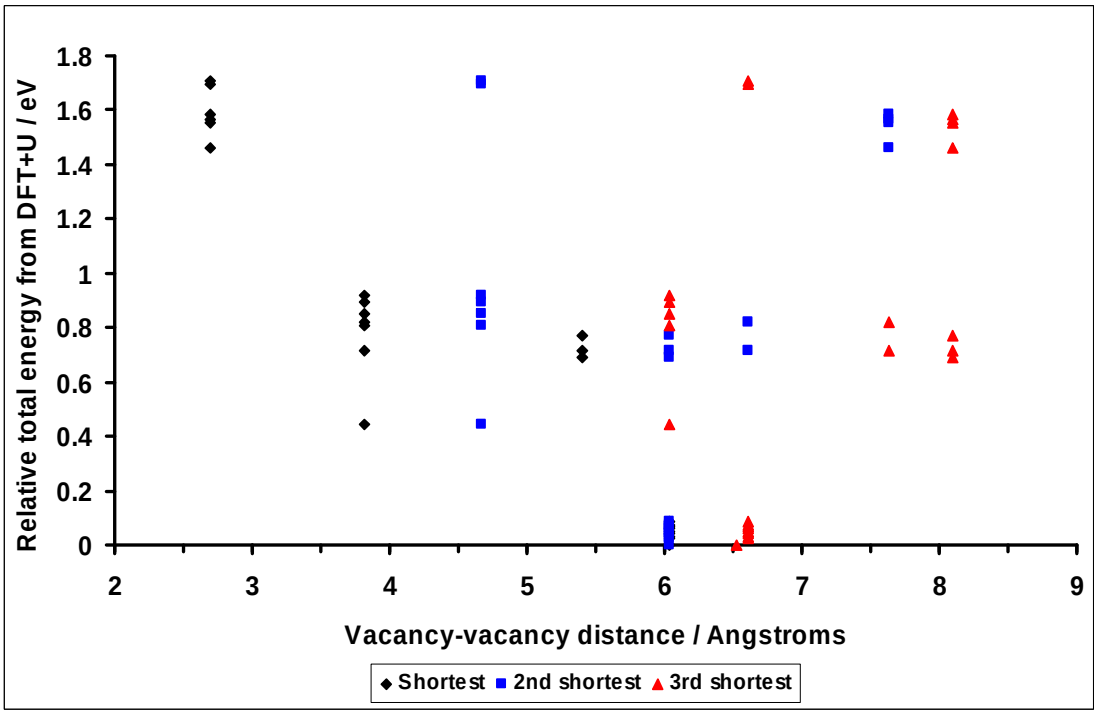

Figure 3–10. DFT+U energy of various 10.3% SDC configurations as a function of vacancy-vacancy distance. All three vacancy separations in the simulation cell are shown. These structures have similar Sm-vacancy distances.

As hypothesized, a number of structures have the optimal vacancy separation, at very low relative energies (within 0.1 eV/cell). Thus it is likely these will all exist in the fuel cell electrolyte.

To compare the effect of Sm-vacancy distance on DFT+U energy, it is imperative to study configurations with a variety of dopant distributions. Several configurations were tested and the results are summarized in Table 3–10, where different sets of structures are separated by dotted lines. The first set of structures are the 28 unique ones favoured with the classical potentials of Balducci *et al.*[6] and Senyshyn *et al.*[7] Secondly, with the optimal vacancy distances, we altered the Sm positions to create different dopant-vacancy distributions. It is important to note that with a given vacancy separation, it is impossible to have all Sm NN to all vacancies, or NNNN to all vacancies. Still, we tried to vary the Sm-vacancy distribution as much as possible with structures in this set. Thirdly, a set of

structures with random positions of dopants and vacancies were investigated. The last set of structures in Table 3–10 are some of the highest-energy configurations found with the reverse-fitness GA at the classical level.

Table 3–10. Relative energies and structural information of selected 10.3% SDC structures

Vac-vac distance range[a] / Å	Sm-vacancy distances # NN (~2.4 Å)	# NNN (~4.5 Å)	# NNNN (~5.9 Å)	# NNNNN (~7.0 Å)	ΔE_{DFT+U} [b] / eV per cell
6.0 - 6.6[c]	1 to 3	11 to 13	0 to 3	0 to 3	0 to 0.10
6.0 - 6.6[d]	2	6	8	2	0.56
	1	7	7	3	0.85
	4	9	5	0	0.19
	3	9	6	0	0.23
	2	7	8	1	0.46
	3	5	9	1	0.56
	1	6	10	1	0.62
	1	5	9	3	0.74
	3	7	7	1	0.56
	0	5	8	5	1.12
2.7 - 5.4	10	8	0	0	1.63
2.7 - 5.4	0	12	6	0	2.28
6.0 - 8.1	6	0	11	1	0.76
7.6 - 7.6	6	0	12	0	1.30
2.7 - 5.4	2	11	5	0	2.18
2.7 - 3.8[e]	0	0	9	9	3.39
2.7 - 3.8[e]	0	1	7	10	3.41
2.7 - 3.8[e]	0	0	10	8	3.30

[a] Range of vacancy-vacancy distances, considering the three distances between vacancies in the cell. [b] Relative total electronic energies from DFT+U calculations. [c] All low-energy configurations recovered from the classical GAs have this distribution. [d] All structures in this set have the same optimal vacancy separation, but different Sm positions. [e] Highest-energy configurations found at the classical level.

Importantly, the low-energy configurations recovered from the classical GA are also the lowest-energy configurations at the DFT+U level. Overall, the results indicate that DFT+U favours precisely the same defect distribution as the classical force field. For instance, the vacancy separation has already been shown to be optimal at 6 Angstroms (see Figure 3–9), with both calculation methods. The structures in the first and second set

of Table 3–10 show that the NNN position of the dopant is favoured. In particular, in the second set, the two structures which were closest to the optimal distribution, with 9 NNN Sm-vacancy interactions, were lowest in energy out of all structures in this set, at 0.19 and 0.23 eV. Also, in general in the second set, the fewer the number of NNN interactions, the higher the energy of the configuration.

The last set of structures in Table 3–10 serve as justification for the correlation between the classical potentials and DFT+U. These configurations are significantly higher in energy than all other structures, at greater than 3 eV over structures with the favoured distribution. Interestingly, these high-energy configurations have identical vacancy separations and similar dopant-vacancy distributions. This further suggests that the same distributions favoured classically are favoured in DFT+U, and that those disfavoured classically are equally disfavoured in DFT+U.

It seems as though no other defect distribution is energetically competitive with the favoured distribution. Indeed, the thermal energy available at 673 and 773 K, which are targeted SOFC temperatures, is 0.058 and 0.066 eV, respectively. Thus, one can expect only configurations with the favoured distribution to be populated significantly at these temperatures. In order to accurately model the SDC electrolyte, future researchers should base their model on the optimal defect distribution found by our GA.

Our findings are in agreement with EXAFS measurements, but offer more information than the measurements provide. The experiment finds isolated vacancies, which is characterized by a lack of NN Sm-vacancy interactions.[17] This suggests a dominance of another Sm-vacancy interaction, such as NNN, although distances further than NN were not seen in the EXAFS experiment. Furthermore, in order for vacancies to

be isolated (and hence mobile), pairs of vacancies cannot be present; in other words, the experiment predicts that no vacancies lie within 4.7 Angstroms of each other, which is replicated by the GA result. Also, because the NN Sm-vacancy interaction is stronger than a NNN interaction,[17] the NNN preference of the dopant, or rather the lack of NN site preference, allows the vacancies to be more mobile in 10.3% SDC.

To summarize, in 10.3% SDC, the Sm ions predominantly occupy NNN positions with respect to the oxygen vacancies, and the vacancies are separated by at least 6 Angstroms. The structure search completed in this section is probably the most relevant of all, because the concentration of 10.3% is closest to that which is used experimentally. In fact, the ionic conductivity of SDC peaks at 11% most likely because there exist more, nearly degenerate configurations available within kT than at lower concentrations. Our GA and subsequent DFT+U evaluation enabled the retrieval and energetic analysis of these structures.

Section 3.5 - GA Search of 14.3% SDC

Above an 11.1% dopant concentration, the ionic conductivity of SDC drops with increasing dopant concentration. Experimentalists first hypothesized that above 11.1%, the concentration of vacancies becomes so high that they aggregate, impeding the conduction of oxygen ions.[18] Later, Ou *et al.*[19] found local oxygen vacancy ordering in 14.3% SDC and other lanthanide doped cerium oxides through selected area electron diffraction measurements. (As a side note, 25 at. % Sm, which is used by Ou *et al.*, is equivalent to 14.3 % Sm_2O_3 dopant. Recall that in this thesis, the dopant concentrations are reported as % Ln_2O_3, where Ln is the lanthanide dopant atom.) In this section, we

investigate the structure of 14.3% SDC, to gain insight on the structural changes above the optimal doping level.

14.3% SDC can be modelled in a 2x2x2 ceria lattice with eight Sm atoms and four oxygen vacancies. Our GA will be used again to find the lowest-energy structures. We begin with classical simulations using potentials from Balducci *et al.*[6] and Senyshyn *et al.*[7], which correlate well with DFT+U calculations.

Five classical GA trials, each with 500 structures in the population, were run for 300 generations. Each trial recovered the same best 13 structures, which is significant considering the enormous search space. These top 13 were read into the initial population of another classical GA, which consisted of 500 structures in total. After 300 generations, the GA did not find any new low-energy structures to displace the original top 13 configurations. Three more trials of this type of GA were run and they completed with the same result. Thus, these top 13 configurations are most likely the global minima of the potential energy surface of 14.3% SDC. Finally, to confirm that structure sampling was sufficient, two larger GA trials were run, each with 1000 structures for 500 generations. The larger trials found the same top 13 configurations as the smaller GA trials, and recovered no new low-energy configurations.

The 40 most fit structures from the classical GAs all had the same defect distribution. Moreover, this distribution is similar to that favoured in 10.3% SDC. The vacancies are separated by at least 6 Angstroms and the dopants prefer the NNN site surrounding the vacancies. In order to confirm that the same defect distribution is favoured with higher level calculations, DFT+U optimizations were run on the top 13 configurations from the GA, as well as other selected configurations. To assess the

influence of dopant ion positions on the energy, configurations with the optimal vacancy distribution but different Sm positions were evaluated. Also, various vacancy distributions were evaluated in DFT+U to assess the influence of vacancy separation on the energy. The results are shown in Table 3–11. No reverse-fitness GA was run on 14.3% SDC, because the correlation between the two methods has already been proven at lower concentrations (see Section 3.1.1, and Section 3.4).

Table 3–11. Relative energies and structural information of selected 14.3% SDC structures

Vac-vac distance range[a] / Å	Sm-vacancy distances # NN (~2.4 Å)	# NNN (~4.5 Å)	# NNNN (~5.9 Å)	# NNNNN (~7.0 Å)	ΔE_{DFT+U} [b] / eV per cell
6.0 - 6.6[c]	3 to 6	16 to 20	4 to 6	3 to 5	0 to 0.13
6.0 - 6.6[d]	1	15	11	5	0.84
	4	14	10	4	0.50
	8	11	10	3	0.25
2.7-5.4	16	16	0	0	3.06
2.7-5.4	0	16	16	0	n/a (didn't converge)
2.7-5.4	0	0	16	16	5.87
6.6-7.6	6	8	14	4	1.65
6.6-7.6	4	12	12	4	1.67
6.6-7.6	6	9	12	5	1.52
3.8-9.4	7	11	9	5	0.66
2.7-8.1	5	14	10	3	2.13
5.4-9.4	6	10	10	6	1.62
4.7-8.1	4	11	11	6	1.68
3.8-8.1	4	13	10	5	1.58

[a] Range of vacancy-vacancy distances, considering the four distances between vacancies in the cell. [b] Relative total electronic energies from DFT+U calculations. [c] All low-energy configurations recovered from the classical GAs have this distribution. [d] All structures in this set have the same optimal vacancy separation, but different Sm positions.

It is clear that the DFT+U-favoured defect distribution matches the classically-favoured one, as all of the top 13 configurations lie within 0.13 eV of the lowest-energy structure. From the energies of configurations with other distributions, it appears that the vacancy separation plays a crucial role in determining the stability of a configuration. For

example, structures with all vacancies separated by too short a distance (2.7 - 5.4 Å) are penalized heavily, whereas structures with all vacancies separated by over 6 Angstroms (6.6 - 7.6 Å) are still penalized, yet not as much. While selecting appropriate structures to evaluate, it was noted that it is difficult to lower the number of NNN interactions in the cell, as there exist so many vacancies that several NNN cation sites are available. Although an extensive configuration search was not done at the DFT+U level, a DFT+U GA is still not needed at this concentration for the same reasons as at 10.3% SDC; mainly, the two methods correlate so well that we can trust the results from the classical GA.

Surprisingly, the optimal vacancy separation remains at 6 Angstroms in 14.3% SDC, even though vacancies are known to order at concentrations above 11% in experiment.[18, 19] This ordering would be represented by vacancies separated by 4.7 Angstroms or less. Consider the fact that there are 26 neighbouring oxygen sites around a vacancy: 6 in <100> sites, 2.7 Å away, 12 in <110> sites, 3.8 Å away, and 8 in <111> sites, 4.7 Å away. As the concentration of dopant increases, the possible number of neighbouring vacancies increases linearly. Ou *et al.* showed that in 14.3% SDC, the possible number of neighbouring oxygen vacancies that could be connected with a given vacancy is large enough to enable the possibility of oxygen vacancy pairs forming, but too small to allow for the formation of chains and other ordered structures.[19] To understand why our calculations of 14.3% SDC show no oxygen vacancy pairs, we must examine the experimental finding more closely.

The segregation of vacancies with dopant cations can play an important role in the ordering. In a real sample of SDC, there exist nanosized domains with doping levels

higher than other parts of the sample.[20-24] Dopant segregation is not uncommon in doped ceria, so it is realistic to expect local dopant concentrations of 40 at. % Sm in a sample that is stoichiometrically 25 at. % Sm (or 14.3% Sm_2O_3). In fact, higher dopant concentrations in nanosized domains was confirmed experimentally by TEM.[19] Because vacancies have an association enthalpy with the dopant ions, it is reasonable to expect pairs of oxygen vacancies to form in these domains. Thus, Ou *et al.* suggests that chains of vacancies form in these domains, generating the order observed experimentally.[19]

Obviously, in our simulations, the entire sample is homogeneously doped at 14.3%, or 25 at. % Sm. Thus, it is impossible to observe the effects observed experimentally due to local ordering, unless our simulation cell is so big that it can house nanosized domains. With just four vacancies and 60 oxygen atoms in the 14.3% SDC simulation cell, it is not possible to create or observe the formation of nanosized domains.

James Hooper performed GA trials on 14.9% SDC in a 3x3x3 simulation cell, which consisted of seven vacancies and 209 oxygen atoms. Even with the larger cell, at this concentration the vacancies remained 6 Å apart in the most fit structure.[25] Although this GA was much more computationally expensive than that on the 2x2x2 cell, the 3x3x3 simulation cell (of 16.2 Å side-length) is still too small to capture the domains, which are on the order of 10 nm.[20] A simulation cell of adequate magnitude to observe these domains would be grossly unfeasible to calculate, even at the classical level of theory.

Overall, we find that 14.3% SDC looks very similar to the 10.3% SDC material. The same structural qualities are favoured at the DFT+U level of theory at both concentrations, which are below and above the 11.1% SDC material used experimentally.

Thus, we expect 11.1% SDC to mimic these properties, which are a dominance of the NNN Sm-vacancy interaction and at least a 6 Angstrom separation between vacancies. These structural findings are in agreement with EXAFS measurements.[17]

To investigate the aggregation of vacancies in highly concentrated SDC, we must raise the dopant concentration above 14.3%, as it exists in the domains of the real material. The next section considers 18.5% SDC, with this goal in mind.

Section 3.6 - GA Search of 18.5% SDC

With the goal of observing vacancy aggregation, we investigated the structure of 18.5% SDC with our GA. Recall that at lower concentrations, vacancy pairing could not be observed due to homogeneous doping across the simulation cell.

18.5% SDC is simulated in a 2x2x2 cell of ceria with 10 Sm atoms and 5 vacancies. In parallel to this work, James Hooper simulated a similar concentration in a 3x3x3 cell.[25] Just as before, we begin with classical energy evaluations with potentials from Balducci *et al.*[6] and Senyshyn *et al.*,[7] because they are known to correlate with more accurate electronic structure calculations.

Five GA trials were run on populations of 500 structures for 600 generations. After the first 300 generations, four out of five of these trials were converged. However, each individual trial did not converge to the same lowest-energy structure. This is most likely because, at this concentration, there are so many defects to place in the cell that it is difficult for a single GA trial to sample all of the low-energy possibilities. Five more trials were run on populations of 1000 structures for 300 generations, which did not find any new structures. From the top 10 structures recovered by the initial structure search,

more GAs were run starting with these structures in the initial population. Nine such trials, each with 500 structures in total, did not find any better configurations after 300 generations. Another trial starting with the same top 10 structures, contained 1000 structures in the population and did not find any better configurations after 300 generations. At this point, sampling of the structure space was sufficient.

The best structures from the classical GA search had one of two defect distributions. In all cases, most Sm are NNN to the vacancies, and most vacancies are separated by 6 or 6.6 Angstroms. However, in some structures, there are two vacancies separated by 4.7 Å, whereas in others, all vacancies are separated by at least 6 Å. For this analysis, we considered all elite structures from the final generation of each GA trial. In some trials, as many as the top 80 structures were elite, and so it is quite significant that they all exhibit one of two vacancy distributions. This result is in contrast to GA results at 10.3 and 14.3%, wherein all favoured structures shared the same defect distribution. In order to determine which of the two vacancy distributions will predominate in the actual material, DFT+U optimizations were done.

34 structures recovered from the classical GAs were evaluated with DFT+U geometry optimizations. In addition, 12 configurations which had either of the two preferred vacancy distributions, but different Sm positions than were found in the GA were tested in DFT+U. Four configurations with a vacancy distribution having two vacancy pairs separated by 4.7 Angstroms (as opposed to just one pair as in the distribution from the GA) were also evaluated in DFT+U. The idea behind this was to test the relative energies of various structures with the two favoured vacancy distributions, and compare their relative energies with structures of other, similar,

vacancy distributions. The results are shown in Table 3–12, where structures are grouped into sets separated by dotted lines.

Based on previous findings for 10.3 and 14.3% SDC, it is reasonable to expect the DFT+U-favoured structures to resemble those favoured classically. However, in order to ensure the correlation holds at 18.5% SDC, we investigated more structures at the classical level, in the following manner. A special version of the GA was designed to find the third-best defect distribution favoured at the classical level of theory. Recall that even with large populations, the previous GAs found only two different distributions of defects that were favourable, so we needed to alter the fitness to remove these two distributions from consideration. The GA was changed so that if a structure had one of the two favoured vacancy distributions, it was assigned a large, positive energy penalty, to remove it from the genepool. Four of these trials were run with 500 structures in the population for 300 generations. The best structures were recovered quickly, and the top structures were common to each trial. The best structures shared the same vacancy distribution, which had most vacancies 6 Angstroms apart, one pair of vacancies 3.8 Angstroms apart, another 9.4 Angstroms apart, although none 4.7 Angstroms apart. Three of these structures were also evaluated in DFT+U. If the correlation holds, then these structures should have relatively higher energies than structures recovered from the normal, unrestricted GAs. Table 3–12 contains the energies of these structures as well. The dopant-vacancy distribution stayed constant in these GA trials, with the NNN interaction dominant.

Table 3–12. Relative energies and structural information of selected 18.5% SDC structures

Vac-vac distance range[a] / Å	Sm-vacancy distances # NN (~2.4 Å)	# NNN (~4.5 Å)	# NNNN (~5.9 Å)	# NNNNN (~7.0 Å)	ΔE_{DFT+U} [b] / eV per cell
6.0 - 9.4[c]	4 to 8	22 to 27	10 to 14	7 to 10	0 to 0.07
4.7 - 6.6[c]	4 to 8	23 to 30	7 to 13	6 to 9	0.17 to 0.58
3.8 - 9.4[d]	6 to 8	22 to 25	10 to 12	6 to 9	0.05 to 0.16
6.0 - 9.4[e]	0	25	16	9	1.69
	10	11	24	5	1.05
	11	12	23	4	1.10
	9*	20	16	5	1.37
	8**	20	17	5	0.86
4.7 - 6.6[f]	0	24	21	5	1.12
	5*	15	22	8	1.49
	6**	15	23	6	0.65
	9	16	17	8	0.17
	8	16	17	9	0.35
	10***	15	17	8	0.20
	10****	14	20	6	0.44
4.7 - 6.6[g]	6	20	18	6	0.89
	8	19	18	5	0.73
	6	22	18	4	0.91
	10***	18	16	6	0.66

[a] Range of vacancy-vacancy distances, considering the five distances between vacancies in the cell. [b] Relative total electronic energies from DFT+U calculations. [c] All low-energy configurations recovered from the classical GAs have one of these distributions. [d] The third-best distribution at the classical level found by a special GA. [e] All structures in this set have the same vacancy distribution which was favoured classically, but different Sm positions. [f] All structures in this set have another vacancy distribution which was also favoured classically, but different Sm positions. [g] All structures in this set have two vacancy pairs at 4.7 Å (not found in the GA). *Sm ions clustered in the cell. **Sm ions scattered about the cell (longer Sm-Sm distances). ***Two Sm NN to each vacancy. **** Four Sm NN to some vacancies, and other vacancies contain no NN Sm ions.

Overall, the results suggest that structures with all vacancies separated by at least 6 Angstroms are more likely to exist at low temperatures compared to structures which have a vacancy pair 4.7 Angstroms apart. Yet there do exist some structures with the 4.7 Angstrom vacancy pair that are as low as 0.17 eV above the lowest-energy structure. Admittedly, it is difficult to predict which vacancy distribution will dominate because the energy ranges of structures with different defect distributions overlap.

Encouragingly, the distribution with two pairs of vacancies separated by 4.7 Angstroms turned out to be high-energy (≥ 0.66 eV/cell) relative to the classically favoured defect distributions. This particular vacancy distribution was not found in any classical GA, and it has a correspondingly high energy in DFT+U. This suggests that the top three classically-favoured distributions may be the most stable in DFT+U.

Yet, the third-best distribution favoured at the classical level (found with the special GA) turns out to be lower in energy in DFT+U than expected. This result suggests that the correlation between the two methods is not as strong at the 18.5% concentration as it is at lower concentrations. It also suggests that configurations with paired vacancies will be populated at 673 and 773 Kelvin, with energies as low as 0.05 eV/cell. The fact that structures with vacancies 3.8 Angstroms apart are favoured over those with vacancy pairs at 4.7 Angstroms support the suggestions of Ou *et al.*, who claimed that the <110> pairs (3.8 Å) are more stable than the <111> pairs (4.7 Å) in doped ceria.[19]

Also, consider the configuration with the favoured 4.7 to 6.6 Å vacancy distribution, and a dopant distribution other than that found by the GA, that was actually low energy (at 0.17 eV/cell) compared to those found by the GA. This finding supports the hypothesis that the correlation between the two methods is not as strong at 18.5%.

Therefore, the structure evaluation at the DFT+U level is not complete, and there may exist more configurations which may alter the energy ranges quoted in Table 3–12. It is not clear which distribution, if any, is favoured at the DFT+U level. Thus, it would be prudent to perform a DFT+U GA on 18.5% SDC to uncover all of the low-energy configurations. However, due to time constraints and limited computational resources, a full scale GA of this kind is not feasible. A smaller DFT+U GA could be run with the

constraint that the vacancies stay fixed, and only Sm positions are altered. In this case, multiple GAs would be run, each on a different given vacancy distribution. Subsequently, the best structures from each GA can be ranked by their DFT+U energy. We plan to perform these structure searches in the near future.

It may be that configurations of both vacancy distributions are energetically competitive, and that no single one dominates, in contrast to the structure at lower concentrations of SDC. Nevertheless, the overall goal was to show that in 18.5% SDC, structures with paired vacancies are present. Although the structure search was not completed to its desired extent, our results suggest that 18.5% SDC contains several configurations with paired vacancies which will exist in nature. However, it is also clear that structures without paired vacancies will also contribute to the overall material.

Recall that Ou *et al.*[19] observed vacancy pairing in nanosized domains of highly concentrated (40 at. % Sm, or 25%) SDC. A GA search and DFT+U evaluation of configurations of 18.5% SDC proved that vacancy pairing starts to occur in the homogeneous material, which is in agreement with the experimental findings. We expect that at higher concentrations, pairing of vacancies will become more prominent.

Section 3.7 - Chapter Summary

In this chapter, we presented the first ever structure search of a metal oxide at a high level of theory. It was found that the DFT+U method correlates well with the classical potentials of Balducci *et al.*[6] and Senyshyn *et al.*,[7] which were used in the genetic algorithm. Using a systematic search, we uncovered the low-energy configurations of 3.2% SDC and found that the NN site is preferred by the dopant, much

like in 3.2% gadolinium-doped ceria. A tandem GA search was done on 6.6% SDC, where we found that no particular site around the vacancy is dominated by Sm ions, and that vacancies prefer to be 6 Angstroms apart. oxygen ion diffusion studies on the low-energy configurations of 3.2 and 6.6% SDC were done at the DFT+U level of theory for the first time. It was found that oxygen ions prefer to migrate sequentially, rather than in a concerted mechanism. Also, the barriers to oxygen diffusion in SDC are similar to those in GDC, which explains the similar ionic conductivity of these materials.

At SDC concentrations closer to the optimal doping level, the same optimal 6 Angstrom vacancy separation was found, although Sm ions preferred to occupy the NNN site around the vacancies, in contrast to 6.6% SDC. These results are in perfect agreement with structural EXAFS data.[17] Finally, above the peak of conductivity at 11.1%, there exist possibilities for paired vacancies in low-energy configurations, which contribute to the decreased conductivity of the material. It was found that the vacancy pairs in the <110> sites are more favorable than the <111> sites, which is in agreement with experiment.[19] This effect was observed at 18.5% SDC in the calculations due to the homogeneous representation of the material, which is not entirely accurate. In summary, the structural information found by the GA is relevant to researchers studying oxygen diffusion mechanisms in SDC, which will enable the design of better solid ion conductors. As well, knowledge of the structure of SDC provides insight on the fundamental interactions which exist in the material, which are important to fuel cell scientists.

Section 3.8 - References

1. D. A. Andersson, S. I. Simak, N. V. Skorodumova, I. A. Abrikosov and B. Johansson, *Proc. Natl. Acad. Sci. U.S.A.*, 2006, **103**, 3518-3521.
2. K. Muthukkumaran, R. Bokalawela, T. Mathews and S. Selladurai, *J. Mater. Sci.*, 2007, **42**, 7461.
3. M. Nakayama and M. Martin, *PCCP*, 2009, **11**, 3241.
4. X. Wei, W. Pan, L. Cheng and B. Li, *Solid State Ionics*, 2009, **180**, 13.
5. K. Eguchi, T. Setoguchi, T. Inoue and H. Arai, *Solid State Ionics*, 1992, **52**, 165-172.
6. G. Balducci, J. Kaspar, P. Fornasiero, M. Graziani and M. S. Islam, *J. Phys. Chem. B*, 1998, **102**, 557.
7. A. Senyshyn, A. R. Oganov, L. Vasylechko, H. Ehrenberg, U. Bismayer, M. Berkowski and A. Matkovskii, *J. Phys.: Condens. Matter*, 2004, **16**, 253.
8. M. F. Mott and M. J. Littleton, *Transactions of the Faraday Society*, 1938, **34**, 0485-0499.
9. P. P. Dholabhai, J. B. Adams, P. Crozier and R. Sharma, *PCCP*, 2010, **12**, 7904.
10. A. Bogicevic and C. Wolverton, *Phys. Rev. B*, 2003, **67**, 024106.
11. J. Hooper, A. Ismail, J. B. Giorgi and T. K. Woo, *Phys. Rev. B*, 2010, **81**, 224104.
12. K. Ando and Y. Oishi, *J. Nucl. Sci. Technol.*, 1983, **20**, 973.
13. H. Hayashi, R. Sagawa, H. Inaba and K. Kawamura, *Solid State Ionics*, 2000, **131**, 281.
14. M. S. Khan, M. S. Islam and D. R. Bates, *J. Mater. Chem.*, 1998, **8**, 2299.
15. S. F. Lee, C. H. Cheng, W. H. Chen and C. W. Hong, *ECS Trans.*, 2007, **7**, 2253-2260.
16. P. P. Dholabhai, J. B. Adams, P. Crozier and R. Sharma, *J. Chem. Phys.*, 2010, **132**, 094104.
17. H. Yoshida, H. Deguchi, K. Miura, M. Horiuchi and T. Inagaki, *Solid State Ionics*, 2001, **140**, 191-199.
18. H. Yahiro, Y. Eguchi, K. Eguichi and H. Arai, *J. Appl. Electrochem.*, 1988, **18**, 527.
19. D. R. Ou, T. Mori, F. Ye, J. Zou, G. Auchterlonie and J. Drennan, *Phys. Rev. B*, 2008, **77**, 024108.
20. T. Mori, J. Drennan, J.-H. Lee, J.-G. Li and T. Ikegami, *Solid State Ionics*, 2002, **154-155**, 461-466.
21. T. Mori, J. Drennan, Y. Wang, G. Auchterlonie, J.-G. Li and A. Yago, *Science and Technology of Advanced Materials*, 2003, **4**, 213.
22. D. R. Ou, T. Mori, F. Ye, M. Takahashi, J. Zou and J. Drennan, *Acta Materialia*, 2006, **54**, 3737-3746.
23. F. Ye, T. Mori, D. R. Ou, M. Takahashi, J. Zou and J. Drennan, *Journal of The Electrochemical Society*, 2007, **154**, B180-B185.
24. F. Ye, T. Mori, D. R. Ou, J. Zou, G. Auchterlonie and J. Drennan, *Solid State Ionics*, 2008, **179**, 827-831.
25. J. Hooper, A. Ismail, J. B. Giorgi and T. K. Woo, *PCCP*, 2010, **12**, 12969-12972.

CHAPTER 4 - ELECTRONIC PROPERTIES OF SAMARIUM-DOPED CERIA

Now that the structure of SDC has been identified, it is possible to perform more detailed investigations on the properties of this material. In this chapter, we provide experimental XPS data on SDC for the first time, and use it as a basis for developing an accurate DFT+U model for SDC. With density of states (DOS) calculations, we parameterize the Hubbard (U) term for samarium, which has not yet been done. These calculations allow for a more detailed interpretation of the XPS spectrum and the prediction of magnetic properties.

Section 4.1 - Experimental

Experiments were run at the Advanced Light Source in the Lawrence Berkeley National Laboratory by John Selwyn, Matthew Brown, Richard Green, and Dr. Javier Giorgi. Unreduced and reduced 8% SDC were measured at the high pressure XPS line with a surrounding atmosphere of approximately 1 torr of oxygen or hydrogen at various temperatures. The average of twenty XPS spectra of unreduced SDC is plotted in Figure 4–1. The graph rises up near the low-energy end due to the presence of background electrons at these energies, which are always present. The XPS of partially reduced SDC is shown in Figure 4–2. Due to experimental problems, the spectrum cuts off at 30 eV below the Fermi level.

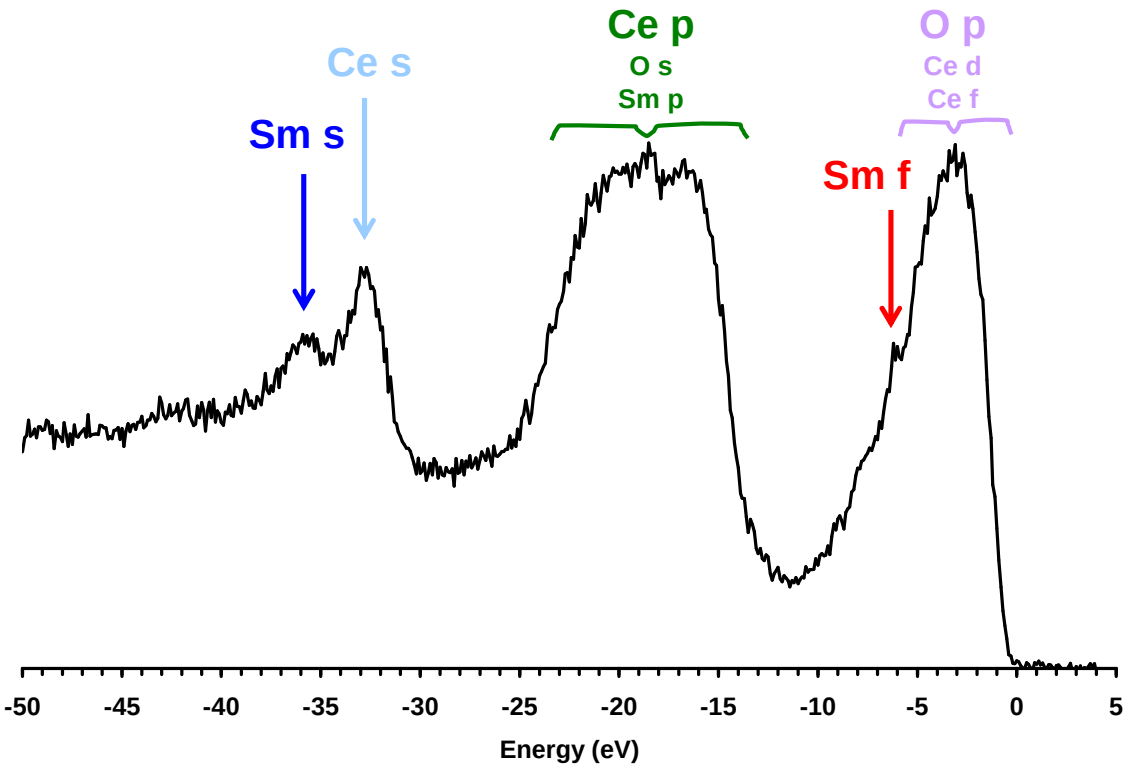

Figure 4–1. XPS of 8% SDC (average of 20 spectra). The zero energy corresponds to zero binding energy. X-axis values are plotted as orbital energies for ease of comparison with calculated DOS spectra. Coloured arrows and lines refer to specific orbital contributions, which are identified by DFT+U calculations in the next section.

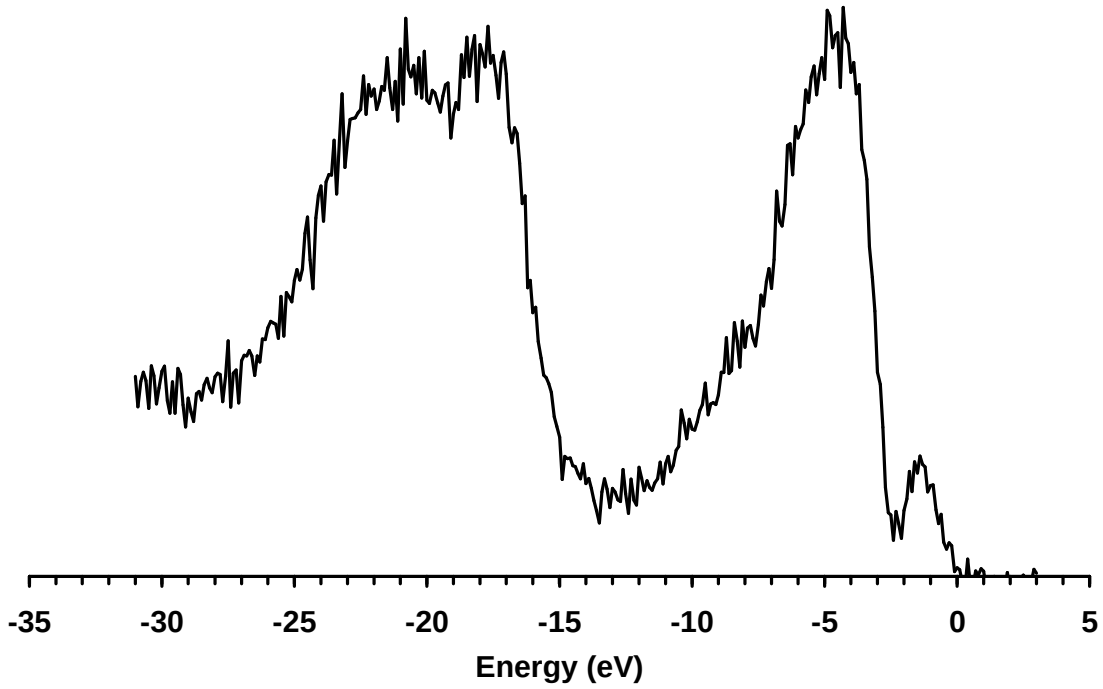

Figure 4–2. XPS of partially reduced 8% SDC. The zero energy corresponds to zero binding energy. X-axis values are plotted as orbital energies for ease of comparison with calculated DOS spectra.

Upon reduction, the peaks shift downward in energy and a new peak appears near the Fermi level, which corresponds to the orbital in which the additional electrons entered. Yet, with only the experimental data, it is difficult to assign individual orbital contributions to the spectrum. For instance, the identity of the orbital which is being filled upon reduction is unknown. While there do exist databases to aid in the interpretation of the XPS,[1] there are several factors that can alter the reported energy of individual orbitals, such as charge transfer and electron screening, which lead to difficulties in assigning all of the contributing orbitals to the peaks in the XPS. By calculating the density of states (DOS) with electronic structure methods like DFT, it is possible to make the peak assignments and therefore better understand the experimental spectrum. In the next

section, we provide these calculations and fit our model to match the XPS of the unreduced sample.

Section 4.2 - Density of States Calculations

In order to understand the results presented in this section, a brief introduction to band theory is necessary. To begin, consider an isolated atom. Its electrons occupy atomic orbitals which each have discrete energy levels. When several atoms are brought in close proximity to form a solid, there exist such a large number of orbitals with very similar energies, that they can be approximated as a continuous band of energies, which contains several electronic states. Therefore, solids have an electronic band structure which consists of occupied and unoccupied orbitals. In metals, there is overlap of the occupied and unoccupied orbitals, and so there exists simply one continuous band which the electrons can occupy, which provides them with the means to conduct electricity. In semiconductors and insulators, like in ceria, there is a region of energy with no orbital overlap in between the fully occupied band and the unoccupied band. These are known as band gaps, and are characteristic of these materials. Although the band gap of ceria is well known,[2] those of lanthanide-doped ceria materials, and in particular of SDC, have not been measured prior to this work. In fact, the electronic band structure of SDC has not yet been investigated in detail. In this work, we examine the density of states (DOS), which is the number of available electronic states at each energy level.

There exist a number of challenges with modeling this system computationally to achieve an accurate band structure. Firstly, the f electrons of samarium must be in the valence of the pseudopotential, in order to observe their contribution to the overall band structure. Yet, DFT calculations with this pseudopotential always fail, which is most

likely due to an inadequate description of the strongly correlated Sm f electrons. It was found that a Hubbard (U) correction is necessary to localize these electrons and allow the calculation to proceed. Yet, unlike for cerium, no prior parameterization had been done for samarium. Therefore, we tested several values of U for Sm, between 2 and 16 eV, in order to find one that matched best with the experimental spectra.

Another challenge present with these calculations is that SDC contains a non-zero magnetic moment.[3] In order to account for this with DFT(+U), one must allow the electronic spins to relax in the calculation. Both the addition of the U parameter on samarium and the spin relaxation contribute to a much longer DFT+U calculation (over two times slower); however, they are necessary in order to properly model this system.

Starting with the goal of matching our calculated DOS to experiment, we calculated the electronic structure of three different configurations of 6.6% SDC with the DFT+U method. We consider 6.6% SDC because it is closest to the 8% material used experimentally (see Section 4.1). We also performed calculations on 10.3% SDC configurations and found no difference in the DOS spectra relative to 6.6% SDC. Furthermore, regardless of the defect ion arrangement in the lattice, the overall DOS was found to be the same in all configurations. Thus, it suffices to consider just one configuration of 6.6% SDC in our calculations to fit the U for Sm to experiment.

Before presenting the parameterization results, it is useful to show the failures of lower level calculations in evaluating the electronic structure. For this purpose, we calculated 6.6% SDC with conventional DFT (i.e. no U parameter on Ce or Sm), as well as with DFT+U, with the U correction on only Ce ions. In these DOS spectra, it is not possible to observe the Sm f electron contribution as these electrons were placed in the

core of the Sm pseudopotential, which allows the calculations to converge. These spectra will serve as a baseline for marking the improved description with the U on Sm, presented later. Although not the most accurate calculations, there are still important spectral features of these DOS plots that can help interpret the experimental spectrum. Figure 4–3 shows the DOS calculated from conventional DFT and DFT+U (with U_{Ce} only) methods. The major atomic orbital contributions to the DOS are represented by the different colours, which match features of the experimental spectrum (refer to Figure 4–1). The orbitals in smaller font in Figure 4–3 have a much smaller contribution to the overall DOS than those in larger font. In fact, the Sm d orbital contribution is so small that it is not identified in the graph. The Ce f orbital is unoccupied, and therefore lies above the Fermi level, as evidenced by our calculated spectra. As XPS recovers only the occupied orbitals, this was not found in the experiment.

Importantly though, most of the experimental spectrum was reproduced by the DFT+U (U_{Ce} only) calculations, which makes it possible to assign the peaks to specific orbitals.

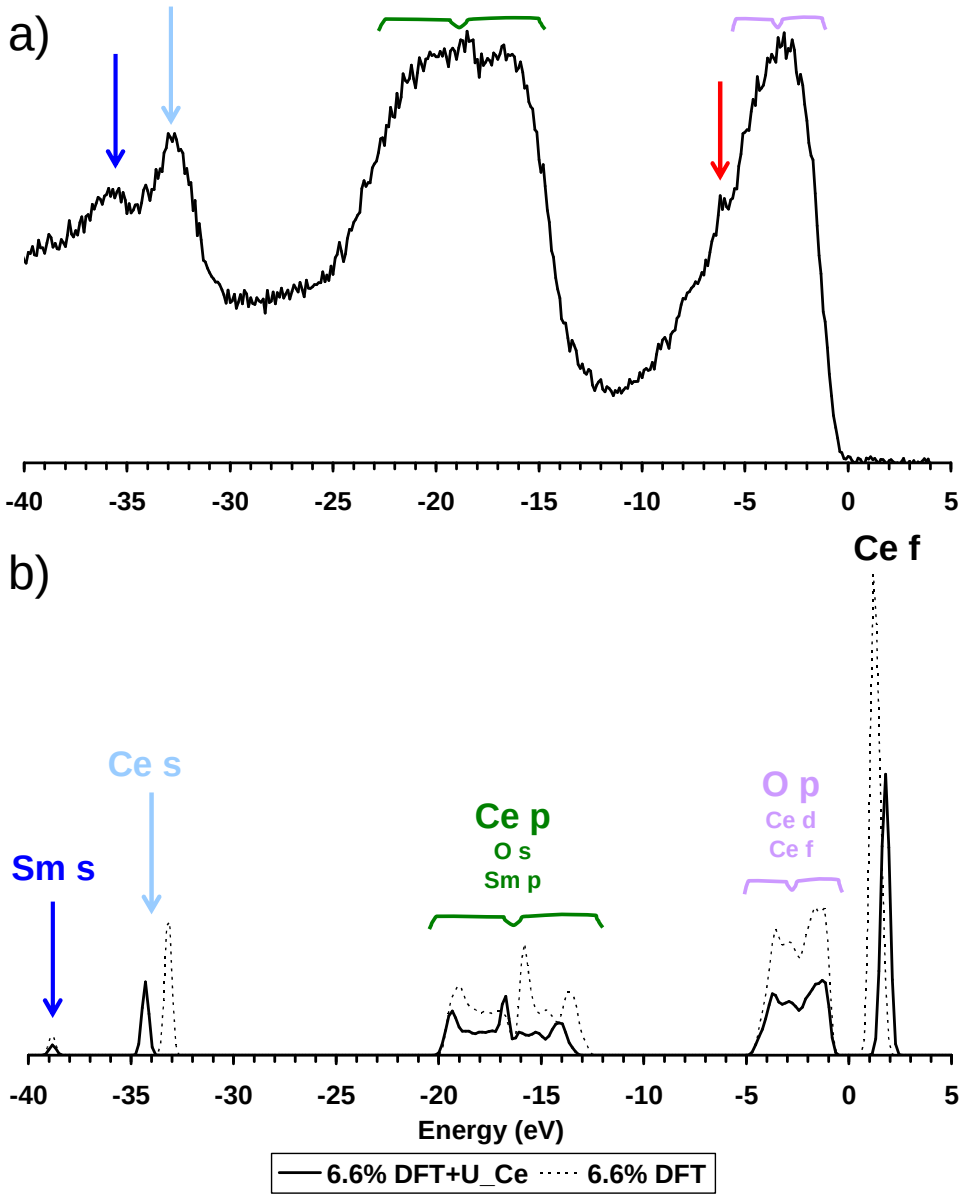

Figure 4–3. a) XPS of 8% SDC; b) Density of states of 6.6% SDC calculated with DFT (broken line) and DFT+U_{Ce} (solid line). All states below 0 eV are occupied. The major atomic orbital contributions are identified above each peak, and their colours match those on Figure 4–3a, for ease of comparison with the XPS spectrum.

The major flaw in these calculations is that the peak at -6 eV, indicated by the red arrow in Figure 4–3a, is not found. The database of XPS binding energies suggests that the samarium f orbital should lie near this value. Indeed, it would make sense that the above calculations did not find this peak because the Sm f electrons were not treated

explicitly, as no Hubbard correction exists for samarium. Thus, we begin our parameterization of the U_{Sm} parameter with the goal of capturing this spectral feature.

Although the DFT+U (U_{Ce} only) calculations allowed the electron spins to relax, the final solution had all spins paired, and so the spin up DOS was identical to the spin down DOS (only the spin up DOS is shown in Figure 4–3). Since SDC is known to exhibit magnetic behaviour,[3] the spin up and down DOS should not be identical. An accurate DFT+U model should be able to reproduce this finding.

4.2.1 - Parameterization of U_{Sm}

It is now evident that to accurately model the electronic structure of SDC, DFT calculations require the Hubbard correction on samarium as well as on cerium ions. Unlike for U_{Ce}, U_{Sm} has not been previously parameterized to experimental observables, such as lattice constant, bulk modulus, and band structure. Here, we use the XPS spectra of SDC to parameterize the U_{Sm} term. The band structure of 6.6% SDC was calculated with the spin-unrestricted DFT+U method, with a U_{Ce} of 5 eV, and U_{Sm} of 2, 4, 5, 6, 8, 10, 12, 14, or 16 eV.

The value of U_{Sm} affects the energy of the Sm f peaks in the DOS spectra, which is to be expected. As U_{Sm} increased, the energy of the occupied Sm f orbital decreased and that of the unoccupied Sm f orbital increased. This trend is illustrated in Figure 4–4, which shows the spin up DOS of SDC. The Sm f orbital contributions with various U_{Sm} values are highlighted by the different colours; only 2, 8, and 16 eV are shown to demonstrate the trend. A small energy window is used to focus on the positions of the Sm f peaks. For the full spectrum, refer to Figure 4–5.

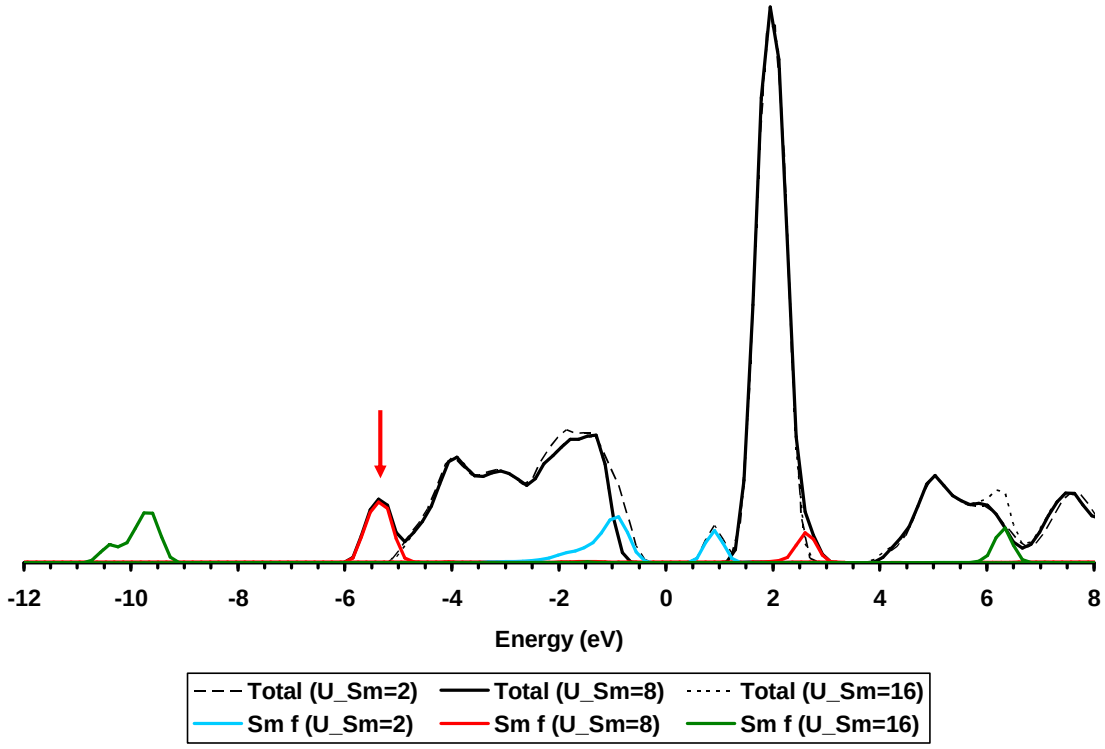

Figure 4–4. Spin up density of states of 6.6% SDC calculated with DFT+U, with U_{Ce}=5 eV and U_{Sm} as shown. All states below 0 eV are occupied. The red arrow corresponds to the experimental peak in Figure 4–1. A small energy window and only a few U_{Sm} values are shown for clarity.

The experimental Sm f peak, highlighted by the red arrow, is best reproduced with a U_{Sm} value of 8 eV. Clearly, U_{Sm} values other than 8 eV incorrectly assign the energies of the Sm f orbital. For instance, with U_{Sm}=2 eV, the Sm f peak lies in the band gap, which was not seen by experiment. On the other side of the spectrum, with U_{Sm}=16 eV, the Sm f orbital is at -10 eV, which is much lower than what was seen in the XPS. The full spectrum, including spin-up and spin-down density of states, for U_{Sm}=8, is shown in Figure 4–5.

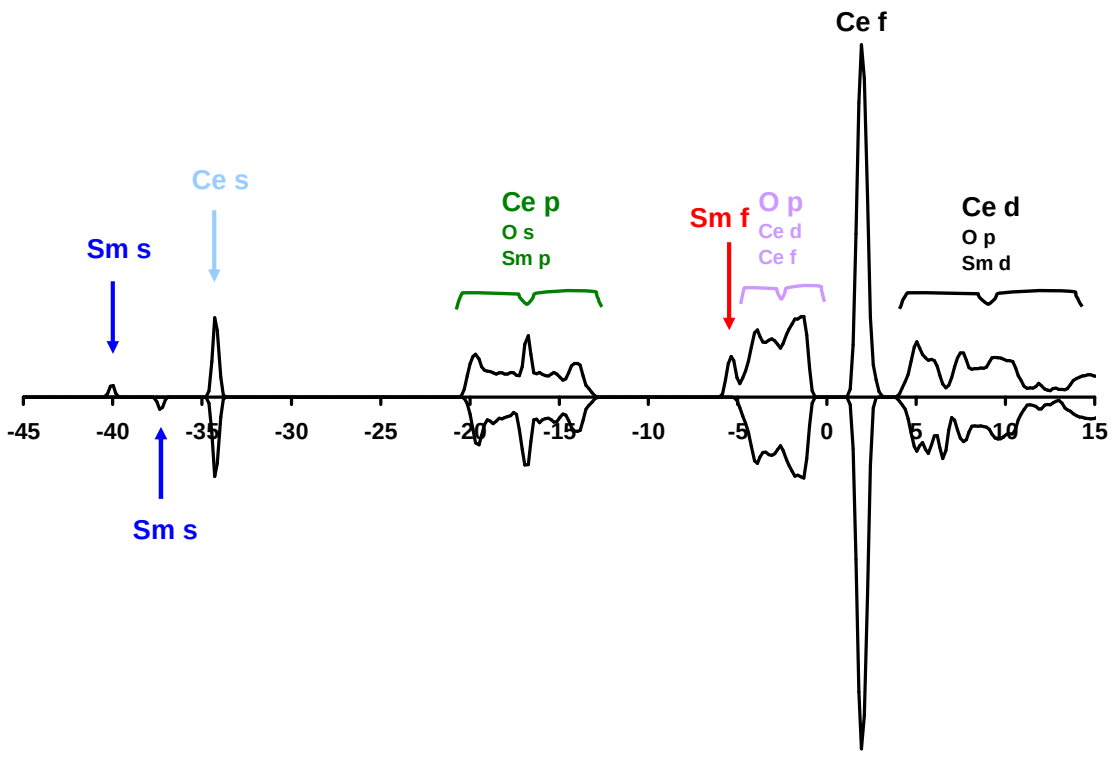

Figure 4–5. Total density of states of 6.6% SDC calculated with DFT+U, where U_{Ce}=5 eV and U_{Sm}=8 eV. The x-axis displays orbital energy in eV. All states below 0 eV are occupied. Spin up and down DOS are represented as positive and negative on the y-axis, respectively. The major atomic orbital contributions are identified above each peak, and their colours match those on Figure 4–1, for ease of comparison with the XPS spectrum.

Interestingly, the spin up DOS does not match the spin down DOS, for any value of U_{Sm}. In fact, all Sm f electrons in the calculation had parallel spins, which indicates paramagnetic behaviour and a non-zero magnetic moment. This finding is in agreement with recent magnetic measurements.[3] Our calculations indicate that the origin of SDC's magnetism is primarily due to the Sm f electrons. All other electrons in the calculation were paired, even though the spins were allowed to relax in the DFT+U optimization. Furthermore, we optimized the same system with a spin-restricted calculation, where the electrons are forced to be paired. This calculation completed with an energy 1 eV higher than the unrestricted spin calculation, which indicates the true low-energy structure has unpaired electrons.

Thus, we have created an accurate DFT+U model for SDC by fitting the U_{Sm} term to experimental XPS data. Our model recovers the experimentally-observed magnetization of SDC, and reproduces XPS measurements on unreduced SDC. More importantly, it provides fundamental insight on these experimental findings.

4.2.2 - Reduced SDC

It is also worthwhile to calculate the density of states of a partially reduced sample of SDC to observe how the electronic states change when electrons are added. We make use of the newly parameterized U_{Sm} value to accurately calculate the DOS of a reduced sample of 6.6% SDC. Such an analysis will also help us understand the differences in electronic states between Ce^{3+} and Ce^{4+} ions, which are both common on ceria surfaces, due to the high reducibility of ceria. Our DFT+U calculations suggested that the Ce 4f orbital is the lowest unoccupied orbital in SDC (see Section 4.2.1) and will become populated upon reduction. Thus, it makes sense to convert two tetravalent cerium ions to trivalent ions and add an oxygen vacancy in the 6.6% SDC lattice to simulate the reduction process. Other researchers have simulated partially reduced ceria in the same way.[4, 5] It is well known that the reduction of pure ceria occurs by this mechanism: namely, where vacancies are formed and the additional electrons are localized on cerium ions, creating the trivalent species.[6] We assume that samarium is not reduced upon reduction, due to the fact that samarium is not stable in the +2 oxidation state. Therefore, our model of 6.6% SDC with an additional vacancy and two trivalent cerium ions should adequately represent the partially reduced SDC sample.

As for pure ceria, the value for U_{Ce3+} has been heavily parameterized based on properties of reduced ceria;[7] the accepted value of 2 eV was used in this description. The

reduced SDC DOS plot calculated with the accurate DFT+U model is shown in Figure 4–6.

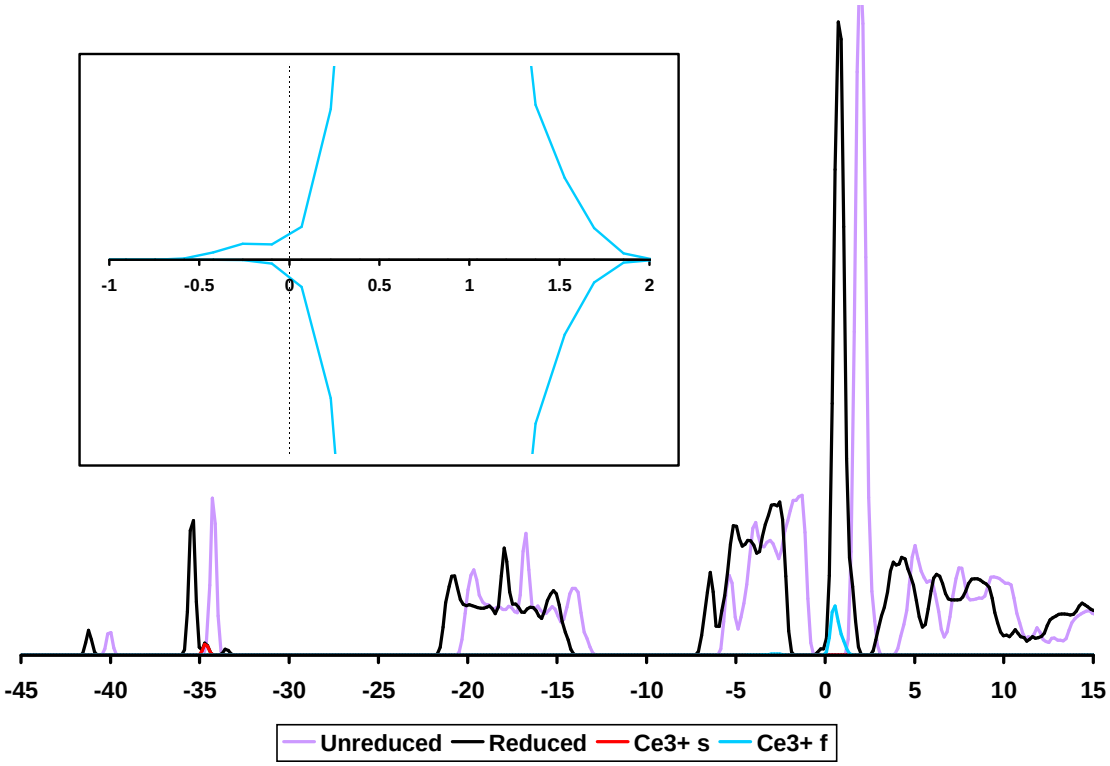

Figure 4–6. Density of states of unreduced and partially reduced 6.6% SDC, calculated with DFT+U, where U_{Ce}=5 eV, U_{Ce3+}=2 eV, and U_{Sm}=8 eV. All states below 0 eV are occupied. Only the spin up DOS is shown for clarity. *Inset:* A magnified view of the cerium f orbital DOS in partially reduced SDC near the Fermi level, showing both spin up and spin down contributions. The faint dotted line at the Fermi level is to guide the eye.

In agreement with experiment (see Section 4.1), all of the peaks in the reduced DOS are shifted to lower energy. This indicates that the energies of the orbitals change as electrons are added to the sample. Most importantly, the Ce 4f orbital peak begins slightly below the Fermi level, at -0.5 eV, which indicates that it is occupied; thus, the DFT+U calculations predict the electrons will reduce the Ce^{4+} ions in SDC. This finding is in good agreement with our experiment, although the experimental spectrum has a larger peak near the Fermi level, indicating that a larger amount of reduction than was modelled took place (see Figure 4–2). It is important to clarify that this discrepancy in the

peak intensity does not represent a problem with the electronic structure description in DFT+U. Rather, it is simply due to the fact that an insufficient amount of reduction was modeled in the SDC simulation cell.

Nevertheless, the model predicts that the new peak near the Fermi level which appears in the XPS upon reduction, corresponds to the Ce 4f orbital. UPS of partially reduced ceria surfaces found the same peak pattern around the Fermi level, which was attributed to the reduction of Ce^{4+} to Ce^{3+} via filling of the 4f orbital.[8, 9] Thus our calculations as well as our experiment indicate that the cerium ions are first to be reduced in SDC, which was expected due to the high reduction stability of samarium, and the high reducibility of ceria.[10]

Our DFT+U calculations also predict that the Ce^{3+} s orbital is of slightly higher energy than its tetravalent counterpart (see red peak in Figure 4–6). Unfortunately, due to experimental limits, the XPS of reduced SDC cuts off at 30 eV below the Fermi level, which does not allow us to observe the low-energy orbitals such as the Ce s and Sm s.

In reduced SDC, the spin up DOS differs from the spin down DOS (see inset of Figure 4–6). We also attempted spin-restricted DFT+U calculations of this material. However, like with unreduced SDC, we found that the spin-unrestricted solution, with unpaired spins, is heavily favoured. This indicates that partially reduced SDC would also exhibit a magnetic moment.

Furthermore, in reduced SDC, the magnetization is higher than in the unreduced sample, due to the additional contribution from the Ce^{3+} which each have an unpaired f electron. Still, the primary source of the magnetization was the samarium f electrons, although this could be because there were only two trivalent cerium ions in our model.

Overall, the calculations suggest that an increase in reduction of the SDC sample would increase the magnetic moment. In theory, this finding is reproducible by experiment, but the magnetic properties of the samples were not measured due to time constraints and lack of available equipment. Nevertheless, this finding is expected because reduced ceria is known to be magnetic.[11-14]

Section 4.3 - Chapter Summary

With the help of the Giorgi lab, we provided the first ever XPS data on SDC. Our electronic structure calculations of the density of states correlate very closely with the XPS measurements. Moreover, the experiment allowed us to fit the value of U_{Sm} to an observable property, for the first time. Fitting our DFT+U-calculated DOS to the XPS spectra, we suggest the optimal value of U_{Sm} to be 8 eV, with the GGA functional. Thus, we have developed an accurate DFT+U model to simulate samarium-doped ceria. With this model, we assigned individual atomic orbital contributions to each peak of the XPS spectra. It was found that Ce^{4+} ions are the first to be reduced in SDC. Also, our model predicted that SDC is magnetic, due to the Sm ions, and that reduced SDC should have an even stronger magnetic moment than the oxidized sample. Prior DFT calculations have not been able to make these predictions, due to the absence of the Hubbard correction on samarium.

Section 4.4 - References

1. J. A. Bearden and A. F. Burr, *Rev. Mod. Phys.*, 1967, **39**, 125.
2. E. Wuilloud, B. Delley, W. D. Schneider and Y. Baer, *Phys. Rev. Lett.*, 1984, **53**, 202.
3. R. Srinivasan and A. C. Bose, *Materials Letters*, 2010, **64**, 1954-1956.

4. M. Nolan, S. Grigoleit, D. C. Sayle, S. C. Parker and G. W. Watson, *Surf. Sci.*, 2005, **576**, 217-229.
5. D. A. Andersson, S. I. Simak, B. Johansson, I. A. Abrikosov and N. V. Skorodumova, *Phys. Rev. B*, 2007, **75**, 035109.
6. A. Trovarelli, *Catal. Rev.-Sci. Eng.*, 1996, **38**, 439-520.
7. C. Loschen, J. Carrasco, K. M. Neyman and F. Illas, *Phys. Rev. B*, 2007, **75**, 035115.
8. M. A. Henderson, C. L. Perkins, M. H. Engelhard, S. Thevuthasan and C. H. F. Peden, *Surf. Sci.*, 2003, **526**, 1-18.
9. D. R. Mullins, P. V. Radulovic and S. H. Overbury, *Surf. Sci.*, 1999, **429**, 186-198.
10. H. Yahiro, K. Eguchi and H. Arai, *Solid State Ionics*, 1989, **36**, 71-75.
11. M. M. Branda, C. Loschen, K. M. Neyman and F. Illas, *J. Phys. Chem. C*, 2008, **112**, 17643-17651.
12. V. Fernandes, R. J. O. Mossanek, P. Schio, J. J. Klein, A. J. A. de Oliveira, W. A. Ortiz, N. Mattoso, J. Varalda, W. H. Schreiner, M. Abbate and D. H. Mosca, *Phys. Rev. B*, 2009, **80**, 035202.
13. V. Fernandes, P. Schio, A. J. A. de Oliveira, W. A. Ortiz, P. Fichtner, L. Amaral, I. L. Graff, J. Varalda, N. Mattoso, W. H. Schreiner and D. H. Mosca, *J. Phys.: Condens. Matter*, 2010, **22**, 216004.
14. V. Fernandes, P. Schio, R. J. O. Mossanek, A. J. A. de Oliveira, W. A. Ortiz, D. Demaille, F. Vidal, Y. Zheng, P. Fichtner, L. Amaral, M. Abbate, J. Varalda, W. H. Schreiner and D. H. Mosca, *Electrochemical and Solid State Letters*, 2011, **14**, P9-P11.

CHAPTER 5 - SURFACE STUDY OF SAMARIUM-DOPED CERIA

In Chapter 3, we found the structure of SDC and identified certain structural properties in the bulk that give it high conductivity. This provides a good starting point for surface studies of SDC. In fuel cells, the surface of a metal oxide catalyst often plays an integral role in the reaction. Of particular interest is the interface between the electrolyte surface, the anode surface, and the gaseous fuel, otherwise known as the triple-phase boundary. Interesting chemistry often takes place at the triple phase boundary, which is important to understand to be able to optimize solid oxide fuel cells. As SDC is a promising electrolyte, it is useful to study its surface properties. An understanding of the structure of the surface of SDC is needed for investigations of the triple phase boundary and fuel oxidation mechanisms.

Section 5.1 - Investigation of (001) and (111) SDC Surfaces

In this section, we make use of the genetic algorithm to find the structure of two low index surfaces of SDC, in order to identify the atomistic interactions which are prevalent at the electrolyte surface. This is the first structure search of a doped metal oxide surface to date. In the past, researchers have simulated surfaces of fuel cell electrolytes like SDC by molecular dynamics, which does not sample all relevant configurations.[1] Yet it is crucial to investigate the low-energy conformers of a material in order to accurately represent it with a computational model.

As the classical potentials of Balducci *et al.*[2] and Senyshyn *et al.*[3] are known to correlate with higher level DFT+U calculations (see Chapter 3), it is reasonable to use

them in a search for low-energy conformers of surface slabs. We performed a structure search similar to the high concentration GA searches in Chapter 3, where the bulk coordinates of pure ceria are input, and the dopants and vacancies are randomly placed in the lattice and evolved over time, until the defect distribution is converged amongst the best configurations. The main difference here is that, in the surface GA, the initial structure is a (001) or (111) slab of pure ceria, with at least 10 Å of vacuum to separate the surfaces in the z-direction. It was quickly realized that the constant pressure optimization in GULP shrinks the cell such that the relaxed cell with the optimized configuration has no vacuum layer. Therefore, all surface GAs had to be run with the constant volume optimization implemented in GULP, to preserve the vacuum layer separating the surfaces. After the optimal distribution is found with classical potentials, we use DFT+U to check that the same defect distribution is favoured at the higher level of theory. Finally, we compare the optimal distribution of defects at the surface versus that in the bulk and highlight any differences.

We chose to investigate these specific surfaces for a number of reasons. Firstly, the (111) surface is known to be the most stable for pure ceria, and therefore should be the easiest to calculate, as the atomic rearrangement is minimal.[4] The (001) surface is interesting for the opposite reason: it is known to be less stable and thus atomic rearrangements are significant.[4] Often in surface catalysis, the less stable surfaces tend to be more catalytically active, so it is useful to study the (001) surface.

While there exist few experimental investigations of the SDC surface, there are several of similar materials, such as gadolinium-doped ceria (GDC) and yttrium-stabilized zirconia (YSZ), which have the same basic structure as SDC and are also fuel

cell electrolytes. In GDC and YDC, experimental[5-8] and theoretical works[9-11] have observed the aggregation of dopants at the (111) and (001) surfaces. As vacancies have an association enthalpy with dopant ions, it is reasonable to expect the vacancy concentration at the surface to be higher than that in the bulk. It will be interesting to observe whether these effects exist in SDC. As long as our slab is made large enough, we should be able to observe aggregation if it is energetically favourable.

5.1.1 - (111) Surface

In order to simulate a surface of SDC most representative of the true electrolyte, we begin with the 10.3% doping level which is close to the value of 11.1% at which conductivity is maximal. The (111) surface of ceria, shown in Figure 5–1, consists of repeating oxygen-metal-oxygen (OMO) layers.

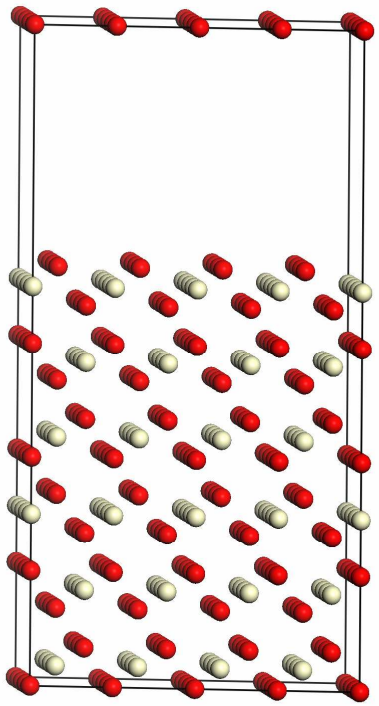

Figure 5–1. Simulation cell of a (111) surface of undoped ceria. The red and white balls represent oxygen and cerium atoms, respectively.

The slabs were all two unit cells wide in the x and y directions, and different lengths in the z direction. Classical GA searches were run on 10.3% SDC slabs of 4, 6, and 8 OMO layers. In each GA, the population consisted of 500 structures and was evolved for a large number of generations. To determine convergence, we waited until the defect distribution amongst the best three configurations remained constant for at least 100 generations.

For all of the (111) slab sizes, we found a Sm-vacancy distribution similar to that of the low-energy bulk structures. For instance, the 6 Angstrom separation between all vacancies is maintained at the surface, and most Sm lie NNN to the vacancies. If the optimal bulk structures are cut to form (111) slabs, their defects are spread evenly throughout the slabs. However, in the (111) slabs recovered from the 6 OMO and 8 OMO GAs, we observed defect segregation to the surface (see Figure 5–2).

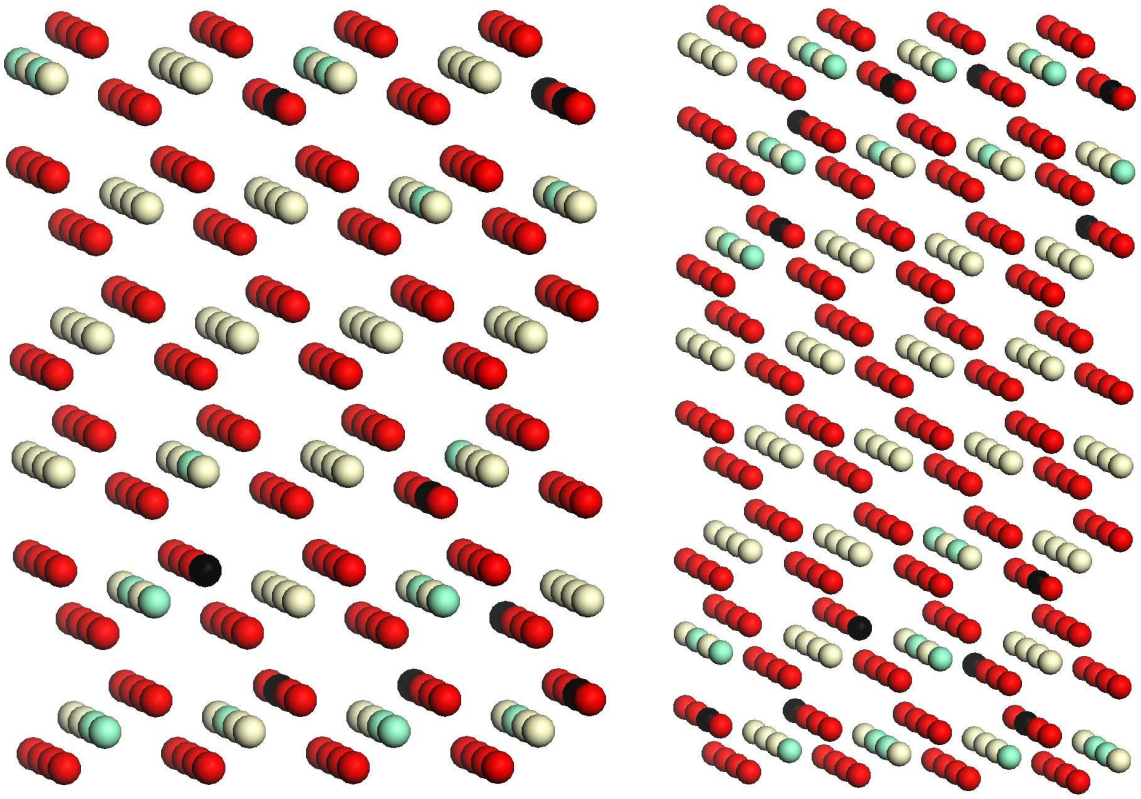

Figure 5–2. Lowest-energy 6 OMO (*left*) and 8 OMO (*right*) 10.3% SDC (111) slabs recovered from classical GAs. Unoptimized coordinates are shown for clarity. The vacuum layer is not shown. The white, red, and green balls represent cerium, oxygen, and samarium ions, respectively, and the vacancies are represented in black.

In the 4 OMO slab, no segregation was observed due to the relatively small depth of the slab. In the 6 OMO slab, one of the central OMO layers contained no Sm atoms and no vacancies. In the 8 OMO slab, more segregation is found, as two central OMO layers were void of Sm atoms and vacancies. The effective dopant concentration ranges from 0 to 1.6% in the middle of the slabs, and is approximately 18.5% at the surface. Yet, at the surface, and throughout the slab, vacancies are still separated from each other by at least 6 Angstroms. Thus it seems like the defects tend to segregate to the surface, but not so much as to create paired vacancies, which are known to be energetically unfavourable (see Chapter 3). Experiments on GDC showed the same segregation,[8] which further illustrates the similarity of these two materials, alluded to earlier in Sections 3.2 and 3.3.

We find that SDC differs from YSZ in that the NN dopant-vacancy interaction is disfavoured in SDC and favoured in YSZ,[11] although dopant segregation is found in both materials.

Interestingly, the vacancies do not appear right at the surface of the material. While there are several close to the surface, they always exist in the bottom part of the top-most OMO layer. Similar sub-surface vacancy aggregation was found by a computational study of the (111) surface of YSZ, which is another common fuel cell electrolyte.[11]

To prove that the GA result from classical simulation is also favoured in DFT+U, we optimized two 4 OMO surface slabs with the DFT+U (U_{Ce} only) method,* one which was found by the GA, and the other which was cut from the optimal bulk positions. The slab from the surface GA had no Sm NN to any vacancy, but 28 NNN interactions, compared to the other which had 4 NN and 22 NNN Sm-vacancy interactions. DFT+U calculations found the slab cut from the optimal bulk structure to be higher in energy by 0.3 eV per cell, which indicates that the slab from the surface GA is heavily favoured.

A few 6 OMO slabs, each consisting of 279 atoms, were also optimized with the DFT+U method. The slab recovered from the GA (which contained a central undoped OMO layer) had the lowest energy in DFT+U once again. A slab cut from the optimal bulk positions was 0.67 eV higher in energy. Both slabs contained predominantly NNN Sm-vacancy interactions, and the main structural difference between the two was that the higher-energy structure did not have any dopant segregation. A third slab was constructed "by hand" from the same vacancy positions found by the GA, that is where the vacancies

* At the time these calculations were done, no U correction existed for samarium; refer to Chapter 2 for the full computational details. All DFT+U calculations in this chapter include only the U_{Ce} correction.

are separated by at least 6 Angstroms. This slab was made to exhibit much more NN and much fewer NNN Sm-vacancy interactions than the previous two. It was not found by the GA, and proved to be 1.77 eV higher in energy than the best slab recovered from the GA, which illustrates the good correlation between the classical and DFT+U optimizations once again. (Refer to Chapter 3 for a detailed discussion of this correlation.)

This high-energy 6 OMO slab contained two undoped OMO layers, which means it has more segregation than the structures found by the GA, which had just one undoped layer. We conclude that structures with more segregation than found by the GA are also energetically unfavourable. In light of the remarkable correlation of classical and DFT+U potentials at this concentration, we are confident that the classical GAs found the true limit to the segregation and the low-energy defect distributions which are present at the (111) surface.

Recall in the bulk 10.3% SDC investigation (see Chapter 3), we tested different vacancy distributions in structures with DFT+U to make sure that the one recovered from the classical GA was indeed the lowest-energy distribution. Since this distribution is the same at the surface, there is no need to perform the test again for the (111) slabs.

It is interesting that although the vacancies segregate to the surface along with the dopants in 10.3% SDC, the vacancies remain 6 Angstroms apart. This suggests that the segregation in SDC (at the optimal doping level) continues until the point where paired vacancies would form. At higher doping levels, the number of defects must become so high that it forces vacancies to pair at the surface, as seen in the bulk at 18.5% (recall Section 3.6). To analyze if this assumption holds, we performed GA searches on 14.3 and 18.5% SDC (111) surfaces. We ran the GA on the 6 OMO slab only, because it was large

enough to observe segregation and still small enough to provide quick calculation times. Classical GAs were run on 14.3 and 18.5% (111) SDC surfaces, to find the low-energy defect distributions. These trials took longer than the 10.3% SDC GA with the same size slab, due to the increased number of defects to arrange in the cell; for instance, at 18.5% SDC, there are 30 Sm and 15 vacancies in the 6 OMO slab, and so the GA took over 1000 generations to converge with 500 structures. The best structures from the high concentration SDC surface GAs are shown in Figure 5–3.

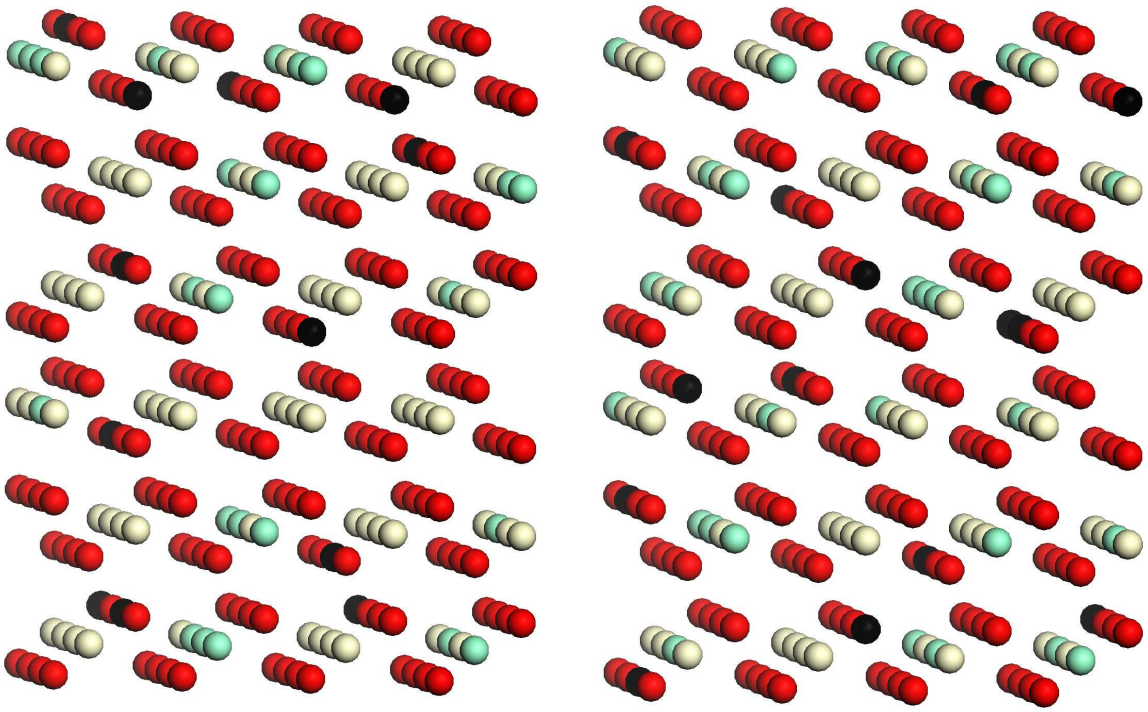

Figure 5–3. Lowest-energy 14.3 (*left*) and 18.5% (*right*) SDC (111) slabs recovered from classical GAs. Unoptimized coordinates are shown for clarity. The vacuum layer is not shown. The colour scheme is the same as in Figure 5–2.

At 14.3%, dopant segregation is visible in the 6 OMO slab, although it is not as striking as at 10.3%. For instance, there are no undoped OMO layers in 14.3% SDC, yet the number of Sm atoms is greatest in the layers closest to the surface. Perhaps with a larger slab, undoped OMO layers could be observed at 14.3% SDC. The effective dopant

concentration is 6.7% in the middle of the slab and 20.8% at the surface, which indicates segregation nevertheless. Importantly, at 14.3%, there exists a vacancy pair 3.8 Angstroms apart, which is consistent with experiment.[12]

At 18.5%, defect segregation is not as obvious as at lower concentrations, although still present. The middle of the slab has an effective dopant concentration of 16.4%, while the surface is 20.8%. The size of the slab could be limiting the observation of defect segregation here as well. However, the purpose of these 14.3 and 18.5% SDC calculations was simply to examine if vacancy pairs formed, not to assess the number. Thus, larger slabs were not evaluated. In 18.5% SDC, vacancy pairs were found in the <110> sites (i.e. the 3.8 Angstrom separation) which is consistent with the findings of Ou *et al.*, who claimed that vacancy pairs prefer <110> sites over <111> sites in doped ceria.[12] We find no vacancy pairs existing in the <111> sites in our slab calculations.

The distribution of defects at the surface is similar to the bulk, in that the NNN Sm-vacancy interaction is dominant. However, the pairing of vacancies at the surface of 14.3% SDC was not seen in the bulk, due to a homogenous distribution of dopants in the bulk cell, which is not perfectly representative of the real material.[12, 13] At 18.5%, more vacancy pairs are observed at the surface than in the bulk, due to the same phenomenon.

While in the process of writing these results, we became aware of a Raman study of the SDC surface, which is the first experimental investigation of the SDC surface to date.[13] This study confirmed the vacancy and dopant segregation that our GA predicted. The fact that our results are in perfect agreement with experiment are indicative of the predictive power of the GA with the chosen classical potentials, even for large search spaces.

In summary, the GA found that all vacancies are separated by at least 6 Angstroms at the (111) surface of 10.3% SDC, whereas at higher concentrations there exist paired vacancies at the surface. In addition, it found the segregation that was observed experimentally.[13] The fact that 10.3% SDC, which is closest to the optimal concentration of 11.1%, has no paired vacancies, demonstrates the nature of its higher conductivity. Furthermore, our GA results suggest that a 6 Angstrom separation between vacancies allows for fast ion conduction in SDC. SDC materials of doping levels above 11.1% have paired vacancies at the surface, which limits vacancy mobility. Thus, the results from our GA reproduce the experimentally-observed trend in SDC conductivity as a function of dopant concentration,[14] and shed light on the fundamental nature of increased conductivity in the optimal material.

5.1.2 - (001) Surface

As with the (111) surface, defect segregation has been observed at the (100) surfaces of YSZ and GDC with classical potentials.[10] Due to the similarity of GDC and SDC, we hypothesize that the same segregation will also be present in SDC. To investigate the (001) surface, we begin with a GA on a 2x2x4 slab of 10.3% SDC using classical potentials from Balducci *et al.*[2] and Senyshyn *et al.*[3] The initial (undoped) slab, shown in Figure 5–4, was made by adding 10 Angstroms of vacuum to a 2x2x4 bulk cell of ceria. The (001) surface consists of alternating layers of metal and oxygen atoms, which means that the slab is Ce-terminated on one side of the vacuum, and O-terminated on the other. Due to this construction, the surface is polar, as cerium atoms are positively charged and oxygen atoms are negatively charged.

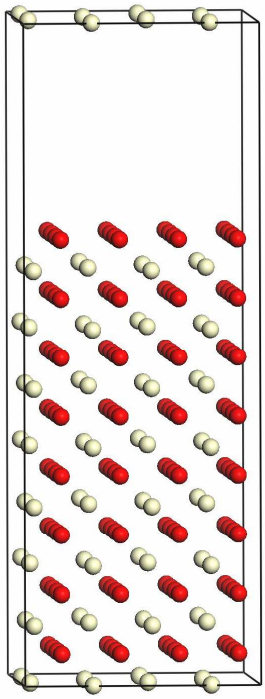

Figure 5–4. Simulation cell of a (001) surface of undoped ceria. The colour scheme is the same as in Figure 5–1.

The 10.3% SDC (001) slabs recovered from the GA all displayed defect segregation. They are shown in Figure 5–5. Two layers of pure Ce atoms are found in the middle of the slab, so there is a clear preference of Sm to be close to the surface. Also, in all configurations, half of the oxygen atoms from one surface migrated to the other side of the slab, such that both sides are half O-terminated. Thus, the non-polar (001) surface is clearly a lower energy conformer. The same behaviour was observed experimentally for pure ceria, as the polar (001) surface is known to be unstable.[15] To find out how this occurred in our simulation, we examined a movie of the classical geometry optimization of one of the structures. The oxygen ions move downward in the z direction by means of the vacancies; as vacancies move towards the surface, oxygen atoms fill in the holes in the center of the slab. Thus, by the end of the geometry optimization, vacancies are

clustered at the surface, near the dopant atoms. Note that this entire process is energetically downhill, as the starting polar slab configuration is relatively unstable.

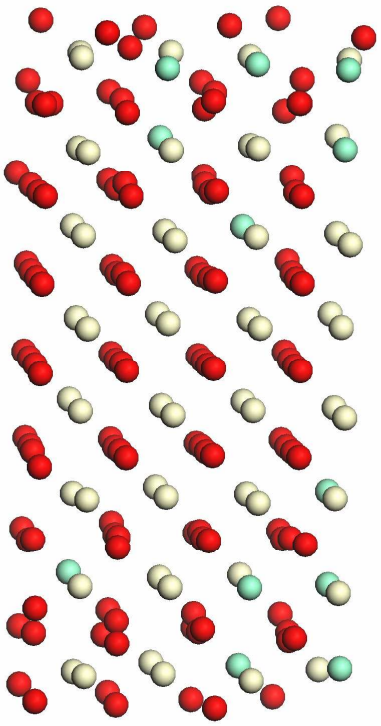

Figure 5–5. Lowest-energy (001) 10.3% SDC slab recovered from classical GA. The vacuum layer is not shown. The colour scheme is the same as in Figure 5–2.

It is difficult to assign positions to the vacancies at the (001) surface after optimization, because the atomic rearrangement is significant. Thus, we cannot conclude whether vacancy separations remain at 6 Angstroms at the (001) surface of 10.3% SDC. Due to the large ionic rearrangement in the optimized structures, the program that automatically assigns vacancy positions did not always place the vacancies in the correct sites. This means that for the (001) surface GAs, the mating and mutation routines which altered the vacancy positions were probably not as effective as they were in the bulk GAs. However, this does not compromise the sampling of (001) surface configurations, as the program correctly assigned vacancy positions during initial structure creation.

Further, the program contains other mutation routines, such as the dopant swap, that can effectively sample the structure space of the (001) surface.

Consider the middle five oxygen layers of the slab, which are void of vacancies, versus the surface and sub-surface oxygen layers. Clearly, with increasing distance from the surface, the atomic displacement decreases. The large number of vacancies present in the half-terminated oxygen surface could be the cause of lack of order of oxygen atoms near the surface. This major atomic relaxation is expected though, because of similar findings for pure ceria.[4, 15†]

The effective surface concentration in the (001) slab is estimated to be 18.5%, based on the number of dopants in the top-most layers. The (111) surface had the same effective surface concentration. In addition, it is interesting to observe that Sm atoms penetrate three layers deep into the surface in the (001) slab, and also in the (111) slabs (see Figure 5–2 and Figure 5–5). To assess the depth of dopant segregation, we investigated 10.3% SDC in larger slabs, such as a 2x2x8 cell for the (001) surface and a 10 OMO cell for the (111) surface. The resulting structures will provide information on how deep the Sm atoms prefer to lie in the surface. Both of these GAs take a substantial amount of computational resources and time, and so are currently in progress.

Also, since it is known that the nonpolar (001) surface is more stable than its polar counterpart, the initial undoped ceria slab for the GA could be constructed to be nonpolar, with half O-terminated sides. This structure search would sample all possible half O-terminations and find the most stable surface configuration, as well as the relative

† The references provided for pure ceria are not a complete list; for the full list, consult the references within ref. 4. M. Nolan, S. Grigoleit, D. C. Sayle, S. C. Parker and G. W. Watson, *Surf. Sci.*, 2005, **576**, 217-229..

positions of Sm atoms and vacancies in the nonpolar slab. We plan to run this GA in the near future.

Section 5.2 - Chapter Summary

In conclusion, we have presented the first ever surface structure search of a doped metal oxide. The GA found defect segregation at the surface of 10.3% SDC, which is in parallel with the results of a recent experiment.[13] These findings show that SDC surfaces are similar to other electrolyte surfaces such as YSZ and GDC.[5-11] At the (001), the GA results revealed the preference of a nonpolar slab. At the (111), most Sm lie NNN to the vacancies and all vacancies remain 6 Angstroms apart, despite their segregation to the surface. The GA result was confirmed with DFT+U calculations. The favoured defect distribution of bulk SDC contains slightly more NN Sm-vacancy interactions and fewer NNN interactions than the surface distribution, although the dominant interaction is still the NNN. At higher concentrations of SDC, we observed vacancy pairing at the (111) surface, which is consistent with experiment,[12] and provides insight on the fundamental nature for increased ionic conductivity at the optimal dopant concentration of 11.1%.

Section 5.3 - References

1. S. F. Lee and C. W. Hong, *CMC-Comput. Mat. Contin.*, 2009, **12**, 223-235.
2. G. Balducci, J. Kaspar, P. Fornasiero, M. Graziani and M. S. Islam, *J. Phys. Chem. B*, 1998, **102**, 557.
3. A. Senyshyn, A. R. Oganov, L. Vasylechko, H. Ehrenberg, U. Bismayer, M. Berkowski and A. Matkovskii, *J. Phys.: Condens. Matter*, 2004, **16**, 253.
4. M. Nolan, S. Grigoleit, D. C. Sayle, S. C. Parker and G. W. Watson, *Surf. Sci.*, 2005, **576**, 217-229.

5. A. Bernasik, K. Kowalski and A. Sadowski, *J. Phys. Chem. Solids*, 2002, **63**, 233-239.
6. A. E. Hughes and S. P. S. Badwal, *Solid State Ionics*, 1990, **40-1**, 312-315.
7. A. E. Hughes and B. A. Sexton, *J. Mater. Sci.*, 1989, **24**, 1057-1061.
8. P. J. Scanlon, R. A. M. Bink, F. P. F. van Berkel, G. M. Christie, L. J. van Ijzendoorn, H. H. Brongersma and R. G. Van Welzenis, *Solid State Ionics*, 1998, **112**, 123-130.
9. P. Dalach, D. E. Ellis and A. van de Walle, *Phys. Rev. B*, 2010, **82**, 144117.
10. H. B. Lee, F. B. Prinz and W. Cai, *Acta Materialia*, 2010, **58**, 2197-2206.
11. A. D. Mayernick, M. Batzill, A. C. T. van Duin and M. J. Janik, *Surf. Sci.*, 2010, **604**, 1438-1444.
12. D. R. Ou, T. Mori, F. Ye, J. Zou, G. Auchterlonie and J. Drennan, *Phys. Rev. B*, 2008, **77**, 024108.
13. M. Guo, J. Q. Lu, Y. N. Wu, Y. J. Wang and M. F. Luo, *Langmuir*, 2011, **27**, 3872-3877.
14. H. Yahiro, Y. Eguchi, K. Eguichi and H. Arai, *J. Appl. Electrochem.*, 1988, **18**, 527.
15. G. S. Herman, *Phys. Rev. B*, 1999, **59**, 14899-14902.

CHAPTER 6 - CONCLUSION

Section 6.1 - Summary

The main goal of this thesis was to identify the fundamental properties of samarium-doped ceria, a widely used solid oxide fuel cell electrolyte, in order to better understand its high ionic conductivity, and aid in the design of better SOFC materials. To this end, we provided new information on the structure of SDC, for the first time at the DFT+U level of theory. A genetic algorithm was developed in order to search for the low-energy configurations of SDC, but can be applied to any doped metal oxide. In addition, the electronic properties of SDC were investigated for the first time, with both experiment and theory. Finally, the surface structure of SDC was determined with the GA, which represents the first ever structure search of its kind. This thesis explains - and more importantly, predicts - the fundamental nature of several important properties of SDC, including high ionic conductivity, magnetism, and surface segregation.

In Chapter 2, we introduced the genetic algorithm method as a means of uncovering the low-energy structures of doped metal oxides that are prevalent at IT-SOFC temperatures. In Chapter 3, we began the GA search on 3.2% Lanthanide-doped ceria, which was also feasible to evaluate systematically as there are only 33 unique configurations. The GA's evolutionary routines recovered the same low-energy configurations as the systematic searches for a variety of materials, including SDC, LuDC, and GDC. In particular, for 3.2% SDC, our first principles DFT+U calculations showed that the NN site is favoured by the dopant, which is in contrast to previous findings at the classical level of theory.[1] The calculations of 3.2% SDC were performed for the first time at the DFT+U level of theory and provide new insight on the defect

interactions present in SDC. For instance, the DFT+U energetics indicate that 3.2% SDC is similar in structure to 3.2% GDC,[2] which indicates that the two materials may share a common origin for their high ionic conductivity.

Similarly, the activation energies for oxygen vacancy migration calculated with DFT+U from the NN to NNN site in 3.2% SDC are close to those for 3.2% GDC, which reinforces the notion that these materials are similar in terms of dopant distribution and diffusion properties. As the NN site is favoured, the NNN→NN migration has lower energy than the reverse migration in both 3.2% SDC and GDC. It was also confirmed that configurations with two dopant ions in close proximity exhibit higher migration barriers than configurations in which the dopant ions lie further apart, which is in qualitative agreement with prior DFT calculations.[3]

The exhaustive structural evaluation for 3.2% SDC configurations was done with a variety of potentials: namely, those from Balducci[4] and Senyshyn,[5] Wei,[1] DFT, and DFT+U. By comparing the structures' classical energies with the energies derived from DFT+U calculations, it was possible to assess the validity of the classical potentials used to simulate SDC. Overall, we found that the potentials of Balducci *et al.*[4] and Senyshyn *et al.*[5] better reproduced the DFT+U-calculated energies compared to the potentials of Wei *et al.*,[1] and that the former were suitable for use in larger scale GAs where DFT(+U) calculations are impractical.

We then used our GA to investigate dopant concentrations above 3.2%. This is the first time DFT+U calculations have been used to explore the structure of SDC at dopant concentrations above 3.2%. It was found that for 6.6% SDC, the dopant ions do not prefer a specific site around the vacancy; this provides insight into the nature of

SDC's high conductivity. The conductivity of SDC is higher at 6.6% than at lower concentrations because several configurations are available within kT at IT-SOFC temperatures, and so vacancies are not trapped in deep potential energy wells. Other materials, which lack a large number of thermally available configurations, such as 3.2% LuDC, have much lower conductivity as a result. Amongst all low-energy 6.6% SDC structures, the vacancies were separated by 6 Angstroms. The importance of this separation became evident at higher dopant concentrations. For instance, in 10.3 and 14.3% bulk SDC, the same separation was found despite the increased number of vacancies in the cell. These findings are in good agreement with EXAFS measurements, which showed that vacancies are not paired in 11.1% SDC.[6] This property allows the vacancies to be mobile, since the presence of vacancy pairs would inhibit diffusion. In fact, it appears that the 6 Angstrom separation is dominant at all concentrations of SDC, which suggests that it is crucial to the oxygen diffusion mechanism in this material.

Furthermore, in 10.3 and 14.3% SDC, most samarium ions occupy the NNN position around the vacancies. This indicates a preference for a site other than the NN site, which is supported by EXAFS measurements on 11.1% SDC.[6] With our GA and with DFT+U calculations, we have accurately assessed defect interactions in SDC at the most optimal doping level, which was previously unfeasible due to the enormous search space. Future studies of the true SDC electrolyte, that is at the 11.1% doping level, are made possible through this work, as the structures found by the GA are most prevalent in solid oxide fuel cells.

The structure search in this thesis has provided an explanation for the observed changes in conductivity as a function of Sm_2O_3 dopant concentration.[7] For 10.3% and

14.3% SDC, the GA found upwards of forty configurations with the optimal defect distribution, which are nearly degenerate. At lower concentrations, fewer low-energy configurations were found, and as a result, the conductivity of these materials is lower. In essence, the conductivity rises with increasing dopant concentration, because of the increase in the number of thermally available configurations, as well as the favourable separation between the vacancies in these configurations, which allows the oxygen ions to be mobile.

Above the optimal doping level, vacancies are known to pair in nanosized domains, which decreases the conductivity.[8] This finding was also recovered by the GA at 18.5% SDC. However, at this concentration, there was more than one low-energy defect distribution found by the GA. As all low-energy configurations exhibited one of just two favoured defect distributions, a special 'restrictive' GA was designed to find the third-most favoured defect distribution at the classical level of theory. Due to this strategic implementation of the GA, we uncovered a new low-energy defect distribution of 18.5% SDC, that contained paired vacancies in <110> sites. This finding is in good agreement with experiment.[8] Yet, it should be understood that in experiment, the dopant concentration of various grains is not the same, as the doping is not entirely homogeneous. Because our simulations could not capture inhomogeneity, it was not possible to observe these effects in a simulation cell of 14.3% SDC.

Overall, the determination of the SDC structure in Chapter 3 identifies the atomistic interactions which affect ionic conductivity in doped ceria. Furthermore, they provide the basis for future computational studies of this material, as the low-energy

defect distributions represent the most prevalent structures in nature, at IT-SOFC temperatures.

In Chapter 4, the electronic properties of SDC were investigated computationally, starting from the low-energy bulk structures recovered in the previous chapter. The electronic structure of SDC was used to help assign the peaks in the XPS spectra of SDC, that were obtained experimentally by the Giorgi group. Conversely, the experimental XPS of SDC allowed us to develop the Hubbard (U) correction for samarium ions, which had never been done before. By fitting DFT+U-calculated DOS spectra to the XPS, we found the optimal U_{Sm} term to be 8 eV with the GGA functional.

Thus, we have established an accurate DFT+U model for investigating SDC's electronic structure. Future electronic structure investigations involving samarium ions will benefit from our parameterization of the U_{Sm} term. With this model, it was found that SDC is paramagnetic, which agrees with experimental measurements.[9] We determined the nature of this magnetization is primarily the samarium f electrons. In reduced SDC, we expect the magnetic moment to be higher, as trivalent cerium ions (which appear upon reduction) add to the overall magnetization.

In Chapter 5, we presented the first ever surface structure search of a doped metal oxide. Investigations such as this are difficult due to the enormous search space, but our GA proved its effectiveness even with large slabs. The calculations predicted that SDC, like other fuel cell electrolytes such as GDC and YSZ, has defects segregating to the (001) and (111) surfaces. Subsequently, a Raman experiment confirmed these predictions,[10] which demonstrates both the effectiveness of the GA and the classical potentials at sampling and evaluating the SDC potential energy surface.

It was found that the distribution of samarium ions relative to the vacancies at the surface is similar to that in the bulk, where the NNN interaction is dominant. Interestingly, although there is vacancy segregation, the vacancies remain separated by 6 Angstroms at the 10.3% SDC surface. Our analysis of the (111) surface slabs suggests that defect segregation is limiting in 10.3% SDC, up to the point where paired vacancies would form. This implies that the 6 Angstrom separation, which is also favoured in the bulk, is a significant structural factor contributing to the enhanced diffusion of SDC. Indeed, at concentrations above the optimal doping level, the low-energy structures contain vacancy pairs separated by less than 6 Angstroms, which decreases conductivity. In fact, our GA discovered that vacancy pairs in concentrated SDC lie predominantly in the <110> sites, which is perfect agreement with selected area electron diffraction (SAED) measurements.[8]

Overall, this thesis offers several significant contributions to the fuel cell and materials science communities. We have identified the atomistic interactions present in the bulk and at the surface of SDC, which contribute to ionic conductivity and defect segregation. Wherever experiment was available, it matched our GA's predictions for bulk and surface structures. For the electronic structure, we provided the first XPS measurements of SDC with the help of the Giorgi lab, and used it to create an accurate DFT+U model for SDC. Researchers interested in the electronic properties of SDC will benefit from the parameterization of the U_{Sm} term provided in this work. Also, mechanistic and oxygen diffusion studies involving SDC are made possible through our structure search of the bulk and surface. Thus, this thesis provides key structural insight that can be used to improve SOFC materials.

Section 6.2 - Future Work

Currently, we are running the GA on larger (001) and (111) surface slabs, to identify the depth of dopant segregation on 10.3% SDC surfaces. In addition, we plan to further investigate the structure of the (001) surface, to understand more about the atomic rearrangements, and identify the low-energy half oxygen-terminated surface configurations which are present at the triple-phase boundary in SOFCs. For this purpose, we will develop a GA code that can sample all possible half oxygen-terminated (001) surface configurations. Currently, the code is setup to sample only the configurations derived from a fully-terminated surface.

As the GAs become more computationally demanding, it will be necessary to have a GA code that can run on multiple platforms (such as Wooki, SHARCnet, and HPCVL) simultaneously. This will involve making significant changes to the code, but will greatly increase the magnitude of the simulations that are possible. For example, we plan to use the updated code to perform the 18.5% bulk SDC GA search at the DFT+U level of theory, to confirm our prediction of vacancy pairs.

As we are interested in identifying the fuel oxidation mechanism, we plan to simulate the triple-phase boundary with the DFT+U method to identify reaction kinetics. Such an analysis would involve adsorbing methane gas (the fuel) and Nickel atoms (the anode) on the low-energy SDC surfaces identified in this thesis.

Alternatively, to gain further insight on SDC's conductivity, we may investigate the oxygen ion diffusion mechanism. This study would make use of the energetic information of different configurations provided in this thesis, to establish a Molecular Dynamics or Monte Carlo simulation that would identify the diffusion pathway.

Section 6.3 - Thesis-related publications

Ismail, A.; Giorgi, J.B.; Woo, T.K. "Atomistic Interactions that Direct Ion Conductivity and Defect Segregation in Samarium-Doped Ceria: A Genetic Algorithm Study", Manuscript in preparation.

Ismail, A.; Giorgi, J.B.; Woo, T.K. "Parameterization of Hubbard Correction to DFT for Samarium Ions in Doped Ceria", Manuscript in preparation.

Ismail, A.; Hooper, J.; Giorgi, J.B.; Woo, T.K. "DFT+U Study of Defect Association and Oxygen Migration in Samarium-Doped Ceria", *Physical Chemistry Chemical Physics*, **2011**, *13*, 6116-6124.

Hooper, J.; **Ismail, A.**; Giorgi, J. B.; Woo, T.K. "Computational Insights into the Nature of Increased Ionic Conductivity in Concentrated Samarium-Doped Ceria: A Genetic Algorithm Study" *Physical Chemistry Chemical Physics*, **2010**, *12*, 12969-12972.

Hooper, J.; **Ismail, A.**; Giorgi, J. B.; Woo, T.K. "A Genetic Algorithm Based Approach to Investigate Doped Metal-Oxide Materials: Application to Lanthanide-Doped Ceria" *Physical Review B*, **2010**, *81*, 224104 (1-11).

Section 6.4 - References

1 X. Wei, W. Pan, L. Cheng and B. Li, *Solid State Ionics*, 2009, **180**, 13.
2 P. P. Dholabhai, J. B. Adams, P. Crozier and R. Sharma, *PCCP*, 2010, **12**, 7904.
3 D. A. Andersson, S. I. Simak, N. V. Skorodumova, I. A. Abrikosov and B. Johansson, *Proc. Natl. Acad. Sci. U.S.A.*, 2006, **103**, 3518-3521.
4 G. Balducci, J. Kaspar, P. Fornasiero, M. Graziani and M. S. Islam, *J. Phys. Chem. B*, 1998, **102**, 557.
5 A. Senyshyn, A. R. Oganov, L. Vasylechko, H. Ehrenberg, U. Bismayer, M. Berkowski and A. Matkovskii, *J. Phys.: Condens. Matter*, 2004, **16**, 253.
6 H. Yoshida, H. Deguchi, K. Miura, M. Horiuchi and T. Inagaki, *Solid State Ionics*, 2001, **140**, 191-199.
7 H. Yahiro, Y. Eguchi, K. Eguichi and H. Arai, *J. Appl. Electrochem.*, 1988, **18**, 527.
8 D. R. Ou, T. Mori, F. Ye, J. Zou, G. Auchterlonie and J. Drennan, *Phys. Rev. B*, 2008, **77**, 024108.
9 R. Srinivasan and A. C. Bose, *Materials Letters*, 2010, **64**, 1954-1956.
10 M. Guo, J. Q. Lu, Y. N. Wu, Y. J. Wang and M. F. Luo, *Langmuir*, 2011, **27**, 3872-3877.